

8. SITE 962¹

Shipboard Scientific Party²

HOLE 962A

Date occupied: 12 February 1995
Date departed: 12 February 1995
Time on hole: 16 hr, 15 min
Position: 3°15.077'N, 3°10.921'W
Bottom felt (drill pipe measurement from rig floor, m): 4648.9
Distance between rig floor and sea level (m): 11.72
Water depth (drill pipe measurement from sea level, m): 4637.2
Total depth (from rig floor, m): 4652.6
Penetration (m): 3.7
Number of cores (including cores having no recovery): 1
Total length of cored section (m): 3.7
Total core recovered (m): 3.71
Core recovery (%): 100
Oldest sediment cored:
Depth (mbsf): 3.71
Age: middle Pleistocene
Comments: Mud-line core; unsplit and frozen for archive only.

HOLE 962B

Date occupied: 12 February 1995
Date departed: 14 February 1995
Time on hole: 1 day, 8 hr
Position: 3°15.063'N, 3°10.919'W
Bottom felt (drill pipe measurement from rig floor, m): 4648.7
Distance between rig floor and sea level (m): 11.72
Water depth (drill pipe measurement from sea level, m): 4637.0
Total depth (from rig floor, m): 4748.7
Penetration (m): 100.0
Number of cores (including cores having no recovery): 13
Total length of cored section (m): 100.0
Total core recovered (m): 85.6
Core recovery (%): 85.6
Oldest sediment cored:
Depth (mbsf): 100.0
Lithology: chert

Age: late Albian
Measured velocity (km/s): 1.598 at 159-962B-8H-4, 79 cm

HOLE 962C

Date occupied: 14 February 1995
Date departed: 15 February 1995
Time on hole: 1 day, 5 hr, 30 min
Position: 3°15.057'N, 3°10.943'W
Bottom felt (drill pipe measurement from rig floor, m): 4639.3
Distance between rig floor and sea level (m): 11.72
Water depth (drill pipe measurement from sea level, m): 4627.6
Total depth (from rig floor, m): 4741.7
Penetration (m): 102.4
Number of cores (including cores having no recovery): 3
Total length of cored section (m): 40.4
Total core recovered (m): 0.58
Core recovery (%): 1.7
Oldest sediment cored:
Depth (mbsf): 102.4
Lithology: chert
Age: late Albian

Comments: Core 159-962C-4M is material recovered while reaming back to bottom.

HOLE 962D

Date occupied: 15 February 1995
Date departed: 22 February 1995
Time on hole: 7 days, 1 hr, 30 min
Position: 3°15.082'N, 3°10.898'W
Bottom felt (drill pipe measurement from rig floor, m): 4657.0
Distance between rig floor and sea level (m): 11.72
Water depth (drill pipe measurement from sea level, m): 4645.3
Total depth (from rig floor, m): 5050.5
Penetration (m): 393.5
Number of cores (including cores having no recovery): 37
Total length of cored section (m): 316.4
Total core recovered (m): 92.76
Core recovery (%): 29.3
Oldest sediment cored:
Depth (mbsf): 393.5

¹Masle, J., Lohmann, G.P., Clift, P.D., et al., 1996. *Proc. ODP, Init. Repts.*, 159: College Station, TX (Ocean Drilling Program).

²Shipboard Scientific Party is given in the list preceding the Table of Contents.

Lithology: siltstone
 Age: late Albian
 Measured velocity (km/s): 2.883 at 159-962D-29R-1, 102 cm

Comments: Drilled: 0–75.1 and 256.4–258.4 mbsf

Principal results: After offsetting to Site 962 in dynamic positioning mode, the previously deployed beacon was switched on and an APC/XCB BHA was made up and deployed to the seafloor. Hole 962A was spudded to recover the mud line alone. Hole 962B was cored by APC until Core 159-962B-11H. Cores 159-962B-10H and 11H showed poor recovery due to cherty interbeds. Continued drilling with XCB resulted in penetration to 100.0 mbsf (Core 159-962B-13X), where drilling was terminated due to bad hole conditions. Hole 962C was spudded as an RCB hole and was washed to 73.0 mbsf before coring was resumed. Only two cores were cut from this hole, which reached 92.3 mbsf. Continued sticking of the pipe and high torque caused by hole collapse forced termination of this hole. Hole 962D was an RCB hole cored below 75.1 mbsf. Despite variable recovery (0%–85%) and penetration rates, coring continued to 256.4 mbsf, where it was halted to replace a broken swivel in the top-drive. Further coring deepened the hole to 393.5 mbsf. It was conditioned with Sepiolite mud and was logged by a reduced Quad logging string and the FMS tool over intervals of 191.0–331.0 and 219.6–291.0 mbsf, respectively.

Drilling in four holes at Site 962 penetrated 393.5 mbsf of sediment. The recovered sediment was divided into three lithologic units (Fig. 1). Lithologic Unit I comprises 47 m of hemipelagic silty clays, and clays (early Pleistocene to early Miocene). Lithologic Subunit IA (middle Pleistocene to late Miocene; 0–26.5 mbsf) consists of silty clays with opal, micrite and plant debris, and clay with nanofossils and pyrite. Lithologic Subunit IB (late Miocene to early Miocene; 26.5–47.0 mbsf) is a pelagic clay that consists of quartz silt, claystone with quartz silt, and claystone. Lithologic Unit II, comprising siliceous pelagic components, radiolarians and diatoms, palygorskite, chert and porcellanite (early Miocene possibly to late Albian), was divided into three subunits. Lithologic Subunit IIA (early Miocene; 47.0–64.5 mbsf) is dominated by grayish green claystone, interbedded with claystone with diatoms, radiolarians, and glauconite. Carbonate is absent. Lithologic Subunit IIB consists of greenish to bluish gray palygorskite claystone, manganese nodules, and glauconitic silty sands. This subunit occurs at 64.5–69.9 mbsf in Hole 962B, and at 73.0–83.1 mbsf in Hole 962C. Lithologic Subunit IIC comprises brown chert and porcellanite that is chaotically intermixed within a clayey sediment. Lithologic Subunit IIC has been recovered at 69.9–100.0 mbsf in Hole 962B, 83.1–102.4 mbsf in Hole 962C, and 75.1–123.5 mbsf in Hole 962D. Lithologic Unit III comprises normally graded siliciclastic sandstones, siltstones, and claystones intermixed with micritic limestones containing planktonic foraminifers and nanofossils of late Albian age. Numerous fining-upward sequences are apparent. This unit was recovered from 123.5 to 393.5 mbsf in Hole 962D.

In Hole 962B, the few bedding measurements recorded in lithologic Units I and II range from 1° to 18°. In Hole 962D (lithologic Unit III), there is a wide range of bedding dip values, mostly due to folding and faulting. Vertical dips related to tectonic deformation were recorded between 180 and 185 mbsf and between 386 and 393 mbsf. Lithologic Unit III shows rare convoluted bedding and slump folding throughout. Normal faulting is common. At 123 mbsf, conjugated normal faults are seen to be formed prior to tilting of the bedding. Reverse microfaults, alone or associated with asymmetrical folds, were observed at various depths. Microfolding is widespread in Hole 962D, showing various morphologies from rounded (e.g., 278 mbsf) to incipient kink folding (e.g., 366 mbsf). Most of the folds are asymmetric except where associated with pop-up structures (e.g., 314 mbsf). Rare evidence of strike-slip motion includes shallowly pitching slickensides along fault planes and flower structures (301 and 372 mbsf) where normal and reverse faults are associated. Veins associated with brecciation occur as infillings of extensional features (e.g., 366 and 386 mbsf).

The Cenozoic is greatly condensed compared to Sites 959–961. Preservation of calcareous microfossils is generally poor. The upper Pleis-

tocene (0–16.8 mbsf) is relatively expanded and lies disconformably on about 5 m of upper Pliocene nanofossil claystone, that, in turn, disconformably overlies 4 m of lower Pliocene claystone. The interval 26.5–36.4 mbsf contains only a few isolated specimens of planktonic foraminifers, suggesting an early Pliocene to latest Miocene age. The interval 36.4–45.9 mbsf is barren, but silicoflagellates and radiolarians at 50.0–64.0 mbsf indicate a late early Miocene age. A disconformity at 65.8 mbsf separates Cenozoic deposits from Albian-Cenomanian(?) cherts and mudstones. The presence of a distinctive palygorskite clay-bearing sequence immediately overlying this disconformity suggests, by lithologic correlation, that lower Eocene sediments may be present in Core 159-962B-8H. Upper Albian to Cenomanian radiolarians and silicified planktonic foraminifers are present at 71.3 mbsf, although the severely disturbed nature of Core 159-962B-8H makes it impossible to assess whether these microfossils are in place or were reworked during a later slumping event. This sequence is underlain by more than 300 m of deformed upper Albian (*R. appenninica* Zone; CC9) turbidites.

In Hole 962B, the magnetic susceptibility is low ($<20 \times 10^{-5}$ SI units) at 0–16 mbsf, and increases to 30×10^{-5} SI units at about 25.5 mbsf, the boundary between lithologic Subunits IA and IB. It remains at this level down to about 45 mbsf. Below this, it falls to $<15 \times 10^{-5}$ SI units, except for an interval between about 65 and 70 mbsf, lithologic Subunit IIB, where values rise to $>30 \times 10^{-5}$ SI units. Susceptibilities throughout Hole 962D are low, generally $<15 \times 10^{-5}$ SI units. NRM intensities show a pattern similar to that of the susceptibility. A zone of high NRM intensity within the Neogene was encountered at Sites 959–961. The upper boundary of this zone was always at Biozone PL3/PL2, or older, and the lower boundary was at Biozone M9, or younger. If the same age relationships apply at this site, it suggests that the depth interval between 25.5 and 45.0 mbsf is younger than Biozone M9, and older than the Biozone PL3/PL2 boundary. Core 159-962B-5H yielded a reversal stratigraphy recovered after a stable component was isolated during cleaning. This magnetostratigraphy can be correlated with Chron 3A (Messinian–late Tortonian).

Five interstitial water samples from 0 to 80 mbsf in Hole 962B reflect the relatively low abundances of calcium carbonate and reactive organic matter, compared to Sites 959–961. Gradients associated with sulfate reduction and ammonium generation are less steep than at shallower sites, indicating that organic matter degradation is less vigorous, although organic carbon contents are relatively high (up to 1.5%). Therefore, the bulk of the organic carbon in the upper portion of the sediment pile at Site 962 must be refractory and not readily degraded, in agreement with its anomalously high hydrogen index (HI) values. Downcore decreases in magnesium concentrations and increases in calcium concentrations are significantly less pronounced than at previous sites due to low calcium carbonate contents. Results from Rock-Eval pyrolysis of Pleistocene sediment show a dominance of reworked, fossil organic matter. Carbonate contents are generally low due to the site being below the carbonate compensation depth, except during the early Pliocene. Late Albian porcellanites (70–100 mbsf) have high organic carbon and low carbonate contents. High C/N ratios and intermediate HI values suggest a mixed terrestrial and marine origin of the organic matter. Between 150 and 195 mbsf, peaks in organic carbon (up to 3.5 wt%) probably indicate periods of high productivity. HI values show a low thermal maturity of marine organic matter. Downcore decreasing HIs show stronger terrestrial influence earlier in the late Albian. The pyrolytic character does not reflect changes in lithology. Hydrocarbon gases were found in significant quantities in Hole 962D. Maximum recorded methane content was 102,214 ppm at 316 mbsf. Heavier hydrocarbons (C₂–C₆) also were present throughout. Ethane (C₂) concentrations up to a maximum of 1401 ppm were recorded at 335 mbsf. Propane through hexane were present in trace amounts.

Physical properties reflect variations in lithology, consolidation, and composition of sediments. Good GRAPE and NGR measurements were obtained from Hole 962B. The most important discontinuities in physical properties data in Hole 962B are at 47 and 70 mbsf, and they correspond to the boundaries between lithologic Units I/II and Subunits IIB/IIC. The first discontinuity, at 47 mbsf, is best reflected in MST, thermal conduc-

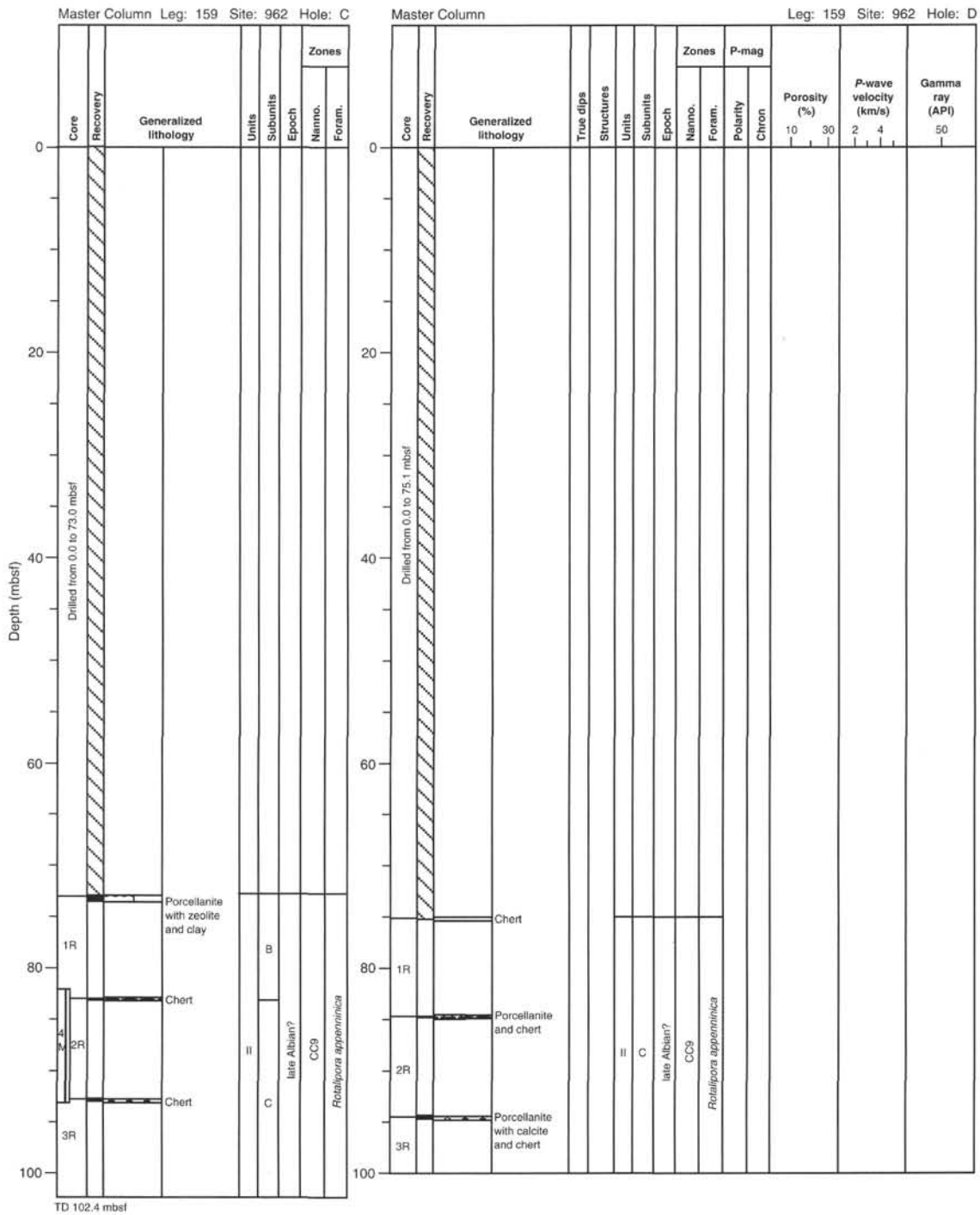


Figure 1 (continued).

in the same direction as the Côte d'Ivoire-Ghana Marginal Ridge (CIGMR) southern slope (Fig. 2). MCS Line MT01 (Fig. 3) and the crossing single-channel line (Fig. 4) reveal that this small bathymetric high is in fact the subdued topographic expression of a narrow acoustic basement structural high, which lies between a thick pile of undeformed sediments to the south, and, to the north, a fault-bounded and rather deformed basin and wedge system, comprising sedimentary reflectors (Fig. 3). A dense set of single-channel seismic lines (see Basile et al., this volume) reveals a similar feature just a few kilometers away to the southwest. These two acoustic basement ridges, bur-

ied by sediments, are elongated (2–3 km wide and 12–15 km long), almond-shaped, and trend southeast–northwest. They lie at the boundary between the southwesternmost extension of the CIGMR (expressed by a wedge of faulted and deformed reflectors to the north, buried by later sedimentation) and the flat-lying sediment cover of the adjacent oceanic crust to the south (Basile et al., 1993). The minor ridges are arranged en échelon according to the structural mapping of Basile (1990) and lie at the transition between the main continental transform CIGMR, and the oceanic fossil Romanche Fracture Zone, which is expressed in a series of aligned, still exposed,

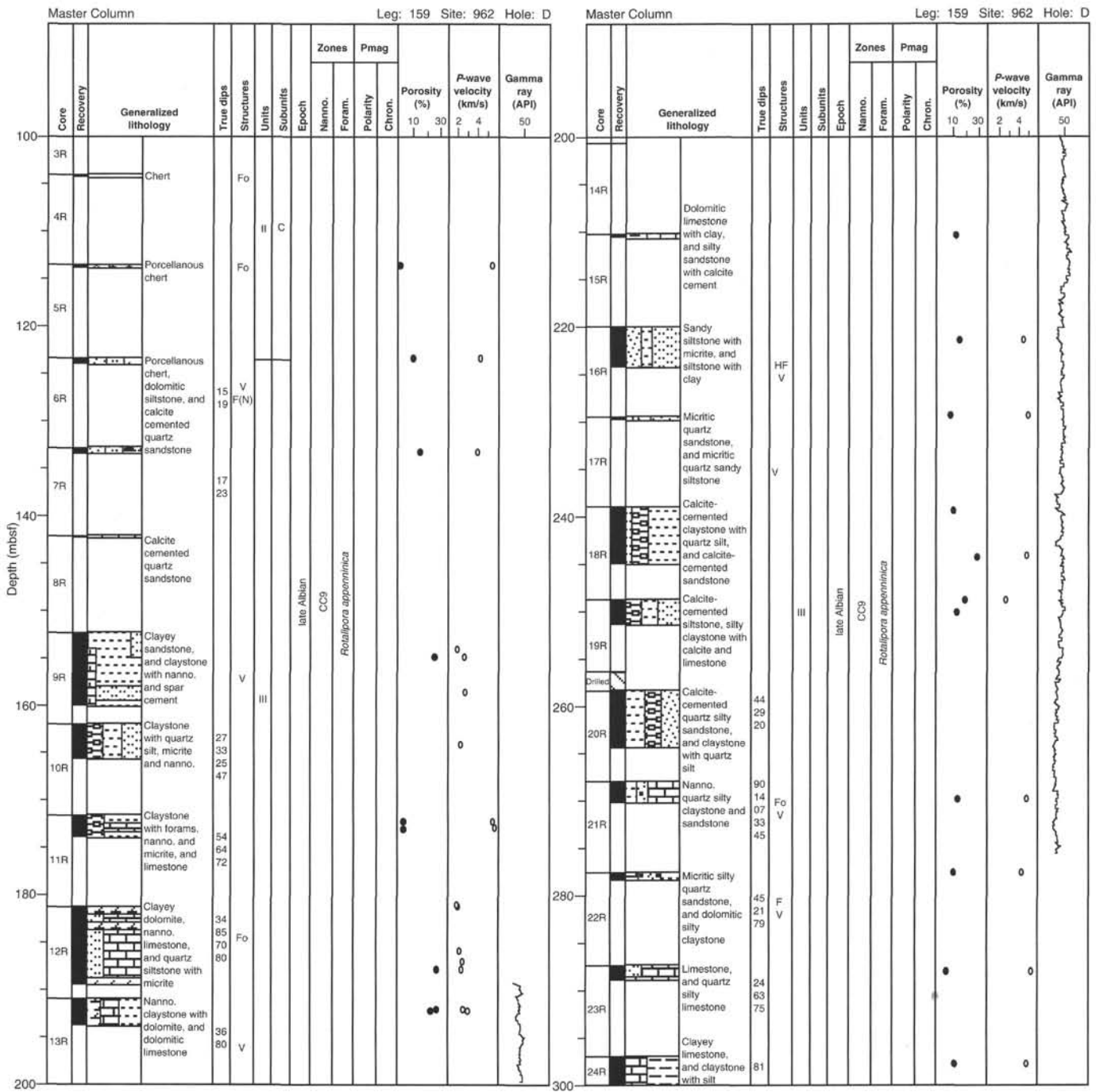


Figure 1 (continued).

acoustic basement highs just a few kilometers away toward the west-southwest (see Fig. 15 of Basile et al., this volume).

Wide-angle seismic data (Sage, 1994) indicate that the crustal section, 10 km north of the easternmost minor ridge, consists of a 7- to 8-km-thick continental crust, while a few kilometers to the south the oceanic crust is only 4 km thick.

Two hypotheses have been considered for the origin of these peculiar elongated basement ridges near the continent/ocean transition:

1. According to Basile et al. (1993) these en échelon ridges may represent narrow continental slivers transported by shear tec-

tonics from either the eastern Ghanian Slope area or the Brazilian Margin (i.e., they have been laterally displaced during active wrench deformation between the two continents). Supporting evidence for this hypothesis includes their almond-like shape, their en échelon arrangement, and their location between the two domains (continental and oceanic) of the transform boundary. Second, the fact that such transport can occur has been demonstrated with recovery from dredging (Honorez et al., 1994) and deep diving (Masclé et al., 1994; Popoff, pers. comm., 1994), of quartzites and mylonitized metasediments from a basement high along the fossil Ro-

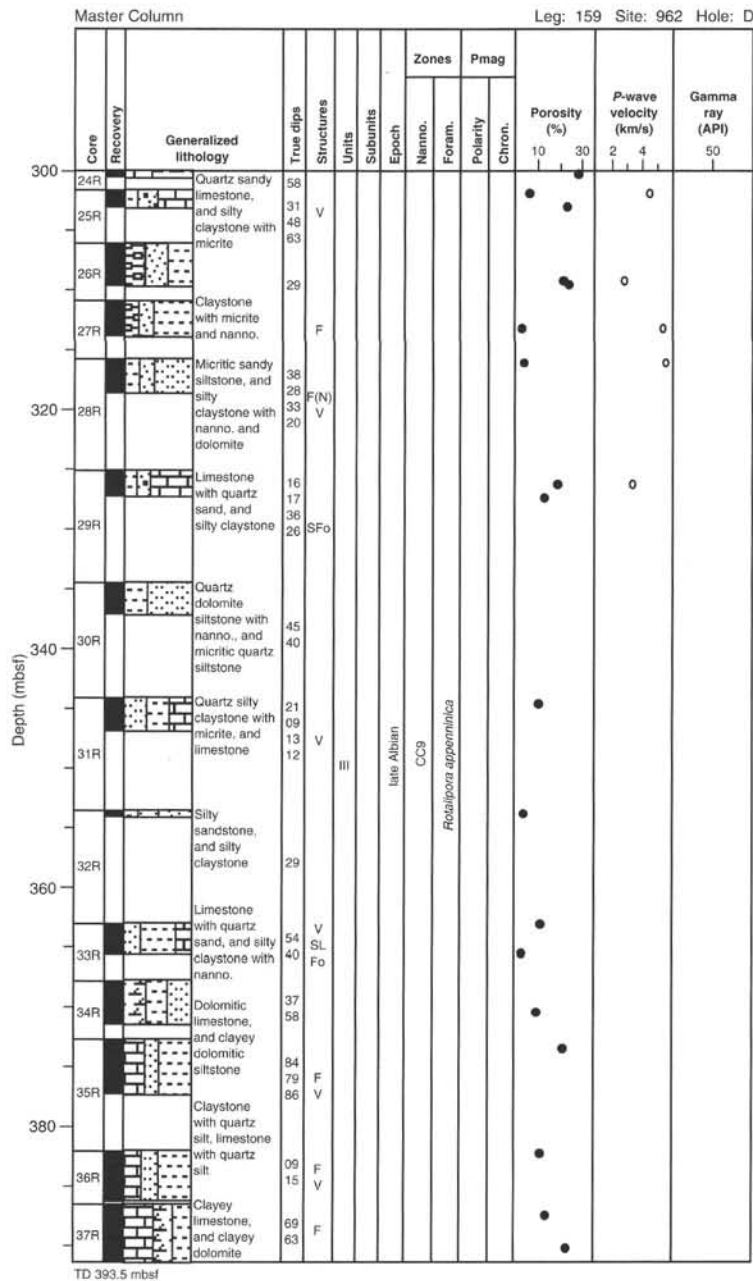


Figure 1 (continued).

manche Fracture Zone, 400 km farther southwest, within the oceanic Gulf of Guinea abyssal plain.

- As an alternate mechanism for the formation of the minor ridges, we suggest that they may have resulted from an upper mantle rising along the ocean/continent boundary as a result of shear tectonism. Such a hypothesis agrees relatively well with the location of the ridges, just a few kilometers away from an atypical oceanic crust, inferred to be made of serpentinized peridotites and discontinuous gabbroic bodies (Sage, 1994).

At Site 962 a migrated, 96-channel MCS Line MT01 (Fig. 5) shows that the acoustic basement feature consists of a thick sequence of short and contorted seismic reflectors whose interval velocities vary between 3.2 km/s, near the top, and 4.6 km/s at a depth of 8.7 s (TWT). These values are compatible either with strongly indurated

material (quartzites) or with serpentinized peridotites. The overlying sediment cover is only on the order of 300 m thick, as a consequence of large scale damming by fault scarps to the north, as well as erosive bottom current activities.

Objectives

Transform Margin Evolution and Continent/Ocean Boundary

The main objective of Site 962 was to determine the nature of the acoustic basement that underlies the continuous reflectors of the more recent sedimentary cover. As discussed above, these minor ridges may be made of strongly deformed sediments that were tectonically displaced during the margin transform stage. Moreover, if the acoustic basement is sedimentary in origin, it should have recorded not only strong deformation (mylonites?), but potentially high-grade

metamorphism, since it is close to, and almost at the same depth as, the adjacent oceanic crust. If the acoustic basement comprises sediments overlying thinned continental crust (hypothesis 1), then a study of these rocks may provide a record of their diagenetic and deformational history. However, if the minor ridges are the result of upper mantle uplift at the ocean/continent boundary (hypothesis 2), then this process should have been recorded by the thermal and geochemical characteristics of the synrift, and possibly the post-rift, sediments. We also hope to determine the age of emplacement of the ridges and their past thermal histories by dating the sediments just above the acoustic basement and by performing fission track dating studies on coarse clastic sediments recovered from this site.

Paleoceanographic Objectives

At a water depth of 4650 m, Site 962 lies nearly 1000 m below the present sill depth for the eastern Atlantic basins. Waters at this depth enter the eastern basins from the west, after spilling over a 3750 m deep sill within the Romanche Fracture Zone. Their character is initially that of the deep waters found at 3750 m water depth in the western Atlantic, and, in spite of some geothermal heating from below and large scale diffusive mixing with overlying waters, waters below 3750 m in the eastern Atlantic are essentially isothermal and isohaline. They are not entirely isochemical, however, because of local modification by organic matter oxidation, the increased solubility of CO₂ with depth, and carbonate dissolution. The cumulative result is that waters overlying Site 962 are predictably different from waters found nearby at the same depth in the western basins. The most obvious sedimentological evidence for this is that today the calcite lysocline and compensation depths are deeper in the eastern basins than they are in the west.

Today Site 962 is located near the depth of the foraminifer lysocline. Consequently, past changes in the character of waters entering the eastern basins, specifically past changes in the carbonate saturation of deep waters flowing in from the western Atlantic, should be recorded as changes in the preservation of planktonic foraminifers at Site 962. During the late Cenozoic, such changes would have been likely to reflect some combination of changes in the carbonate saturation of western Atlantic deep waters and changes in their local modification by organic matter oxidation. On longer, tectonic time scales, such changes should also reflect the evolution of the fracture zones through which the deep waters flow. A primary paleoceanographic objective of Site 962 was to document past changes in the preservation of foraminifer carbonate in the eastern Atlantic basins.

OPERATIONS

During the transit to Site 962, the rotary bit, mechanical bit release, and core barrel (RCB) were laid out, and the drilling line was cut and slipped. The rig crew then started to make up the advanced piston corer/extended core barrel (APC/XCB) bottom-hole assembly (BHA). In addition to spacing out the APC/XCB core barrels, the Motor Driven Core Barrel (MDCB) was function-tested at the rig floor. The tool failed to unlatch during the pumping test. Upon inspection it was determined that the latching mechanism and thruster shaft had seized, probably due to several months storage in the core barrel storage shucks. After freeing these components the tool was tested again. This time the latching mechanism and thruster shaft operated properly. The tool was then set aside and the remaining portion of the BHA was assembled. At 1015 hr on 12 February, the vessel was within 0.9 mile of the site coordinates, at which time the pre-placed positioning beacon was commanded on and the acoustic signal received. By 1130 hr, the vessel was positioning in automatic mode over Site 962. Coring operations for all holes drilled at Site 962 are summarized in Table 1.

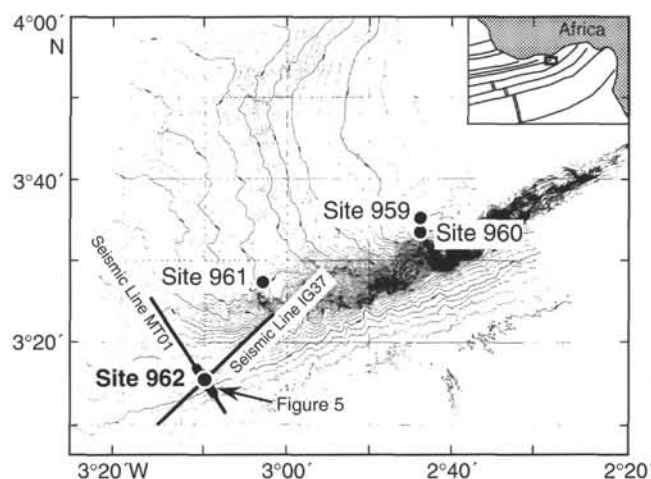


Figure 2. Location of Site 962 on a swath bathymetric map of the Marginal Ridge and surrounding area (*Equamarge II* survey, 1988). Bathymetric contours are in meters (contour interval 50 m); MCS migrated seismic Line MT01 (*Equasis* survey, 1990) and single-channel Line IG37 (*Equamarge II* survey, 1988) on which the site is located are also indicated.

Hole 962A

After the drill string was tripped to the seafloor, the top drive was picked up, and the APC core barrel was deployed. The corrected precision depth recorder (PDR) reading normalized to driller's datum for this hole was 4621.4 m. Coring began with a request for one additional mud-line core. In an attempt to maximize recovery for sampling purposes, the first APC was taken from a depth of 4619 m. Three water cores in succession followed until 3.71 m of core was recovered (Table 1), establishing the seafloor at a depth of 4648.9 m by direct pipe measurement (DPM). Hole 962A was spudded at 2330 hr on 12 February, after which the APC was immediately retrieved, thus ending Hole 962A after a single piston core.

The relatively large depth discrepancy between PDR and drill pipe measurement was never accounted for. A check of the pipe tally revealed no errors or "missing" stands. Likewise, another check of the PDR system yielded results identical to the initial reading.

Hole 962B

After recovering the only core taken from Hole 962A, the APC core barrel was again run to bottom and Hole 962B was spudded at 0045 hr on 13 February, with water depth at 4648.7 m (DPM). APC coring continued to 93.3 mbsf (Core 159-962B-11H). Core orientation using the Tensor tool was attempted in this hole, starting with Core 159-962B-3H. Coring continued without problem until Core 159-962B-10H, which did not fully stroke and required 100,000 lb to pull free. On retrieval of the core barrel a few pieces of chert were found in the liner. The final APC core of Hole 962B (Core 159-962B-11H) also did not exhibit normal end-of-stroke pressure bleed-off; however, it required only 30,000 lb to extract from the formation. Upon recovery the barrel again had just a few pieces of chert in the core catcher. As a result of these coring difficulties, coring proceeded using the XCB for the next two cores (159-962B-12X and 13X) to a depth of 4748.7 m (DPM) or 100.0 mbsf (Table 1). The drilling of this interval was characterized by abnormally high pump pressure (40 spm, 1200 psi) and high torque (500–700 amps). Little progress was made before the ability to circulate was completely lost and the pipe became stuck. Within 30 min circulation was again established and the string was freed with 150,000 lb of overpull. Because of these

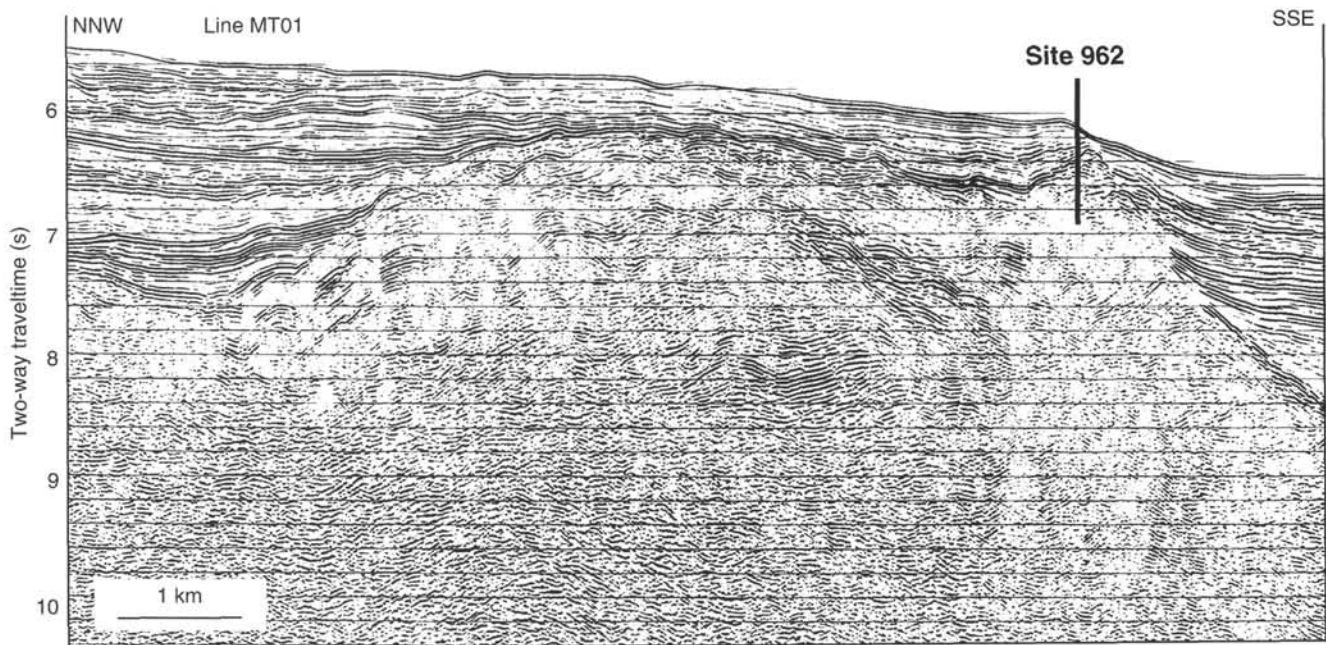


Figure 3. Migrated section of MCS seismic Line MT01 (*Equasius* survey, 1990) perpendicular to the westernmost and buried end of the Côte d'Ivoire-Ghana Marginal Ridge (see Fig. 2). Location of Site 962 is shown. The site is located almost on the summit of a small acoustic basement ridge that extends just south of the buried and deformed CIGMR and just north of the oceanic crust, which is covered by a thick sequence of undeformed sediments.

problems a 20-barrel high-viscosity mud pill of Bentonite gel was circulated and the core barrel was recovered. A center bit was dropped and efforts continued to clean up and stabilize the hole. At 2230 hr, after advancing to a total depth of 4752.4 m (103.7 mbsf), the hole was abandoned due to worsening hole conditions. The drill string was pulled out of the hole, clearing the seafloor at 2300 hr on 13 February. The top drive was set back and the drill string was tripped back to the vessel. The bit reached the rig floor at 0730 hr on 14 February ending Hole 962B.

Hole 962C

While the BHA was changed over from APC/XCB to an RCB configuration, the ship was offset 50 m to the west. The drill pipe was tripped to the seafloor, and Hole 962C was spudded at 1630 hr on 14 February. With a center bit in place, the bit was advanced to a depth of 4712.3 m (73.0 mbsf) where RCB coring commenced. Hole trouble was apparent from the start of coring operations. Core 159-962C-1R advanced to a depth of 82.6 mbsf; however, after picking up a single stand of pipe the hole was found to have a meter of fill on-bottom. While attempting to cut Core 159-962C-2R high torque and pump pressure were evident. After the pipe was worked around in the hole, Core 159-962C-2R was eventually cut to a depth of 92.3 mbsf. Despite circulation of a high-viscosity mud pill in an attempt to clean up the hole, conditions did not improve. Continued working of the pipe was unsuccessful, and it became more and more difficult to reach the bottom of the previously drilled hole. At 0200 hr on 15 February Core 159-962C-2R was recovered and another barrel was pumped to bottom. However, on lowering the pipe, another 3 m of fill was found at the bottom of the hole. Attempts to advance through the fill resulted in high torque and continued sticking of the pipe. A Sepiolite mud pill was circulated to aid in hole cleaning. However, all efforts to reach the original bottom of the hole were frustrated by the hard, broken, chert formation. The decision to abandon the hole was made at 1200 hr on 15 February. After the core barrel was recovered, the drill pipe was pulled clear of the seafloor at 1300 hr on 15 February, ending Hole 962C.

Hole 962D

One final attempt to achieve deep penetration and coring was made at Hole 962D. The ship was offset 100 m east in the hope that the drilling conditions would be improved. At 1330 hr on 15 February Hole 962D was spudded at a seafloor depth of 4657.0 m (DPM). The corrected precision depth recorder reading normalized to driller's datum for this hole was 4623.8 m. With a center bit in place, the bit was advanced to a depth of 4732.1 m (75.1 mbsf) where RCB coring commenced. RCB coring (Cores 159-962D-1R through 19R) continued to a depth of 4913.4 m (256.4 mbsf). Recovery in this interval was highly variable, ranging from 0% to 85%. The rate of penetration also was quite erratic, varying from 5.7 to 12.8 m/hr.

Gas chromatograph (GC3) and Natural Gas Analyzer (NGA) analysis on Core 159-962D-9R, immediately below the chert layer, indicated the first presence of long-chain hydrocarbons, which ranged up as high as C₅. Core 159-962D-13R contained 6 ppm of C₆, although this proved to be the only occurrence of this hydrocarbon in Hole 962D. As coring progressed, the percentage of hydrocarbons decreased downhole, except for occasional spikes related to shale interbeds with high organic content.

During the cutting of Core 159-962D-19R, the top drive swivel began leaking hydraulic oil. After Core 159-962D-19R was recovered at 1130 hr, the top drive was set back, the drill pipe was pulled to a depth of 4751.4 m (94.4 mbsf), and the circulating head was installed. A constant drag (overpull of 35,000–40,000 lb) was experienced in the lower 60 m of Hole 962D. Above that point the hole seemed to be in good condition until 133 mbsf, where the same tight spot seen on the previous wiper trip was encountered.

By 1800 hr on 17 February the spare swivel had been installed, the wireline blow-out preventer (BOP) and WKM valves re-installed, and all hoses re-connected. The drill string was run back into the hole to 4847.0 m (190.0 mbsf) and the top drive was picked up. The last 66 m of hole required washing and reaming until the original depth of 4913.4 m (256.4 mbsf) was reached. A 15-barrel Sepiolite mud pill was circulated and at 2230 hr the drilling center bit was recovered.

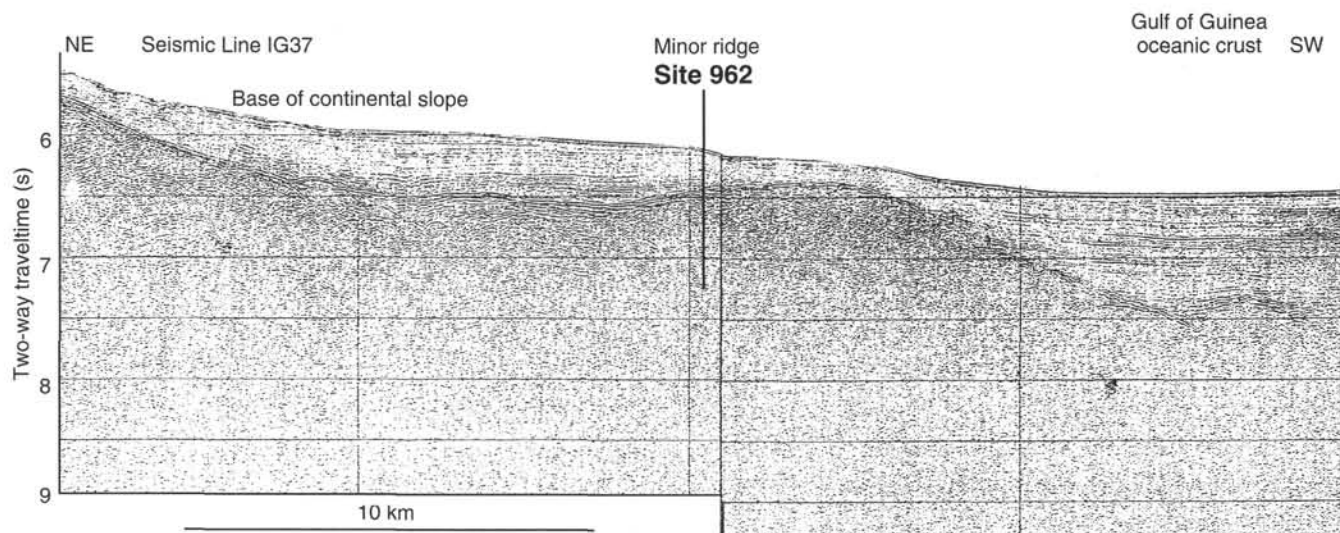


Figure 4. Single-channel seismic Line IG37 (*Equamarge* survey, 1988) almost along strike of the eastern minor ridge; this last shows as a subdued acoustic basement feature emplaced between the oceanic crust and the foot of the continental slope.

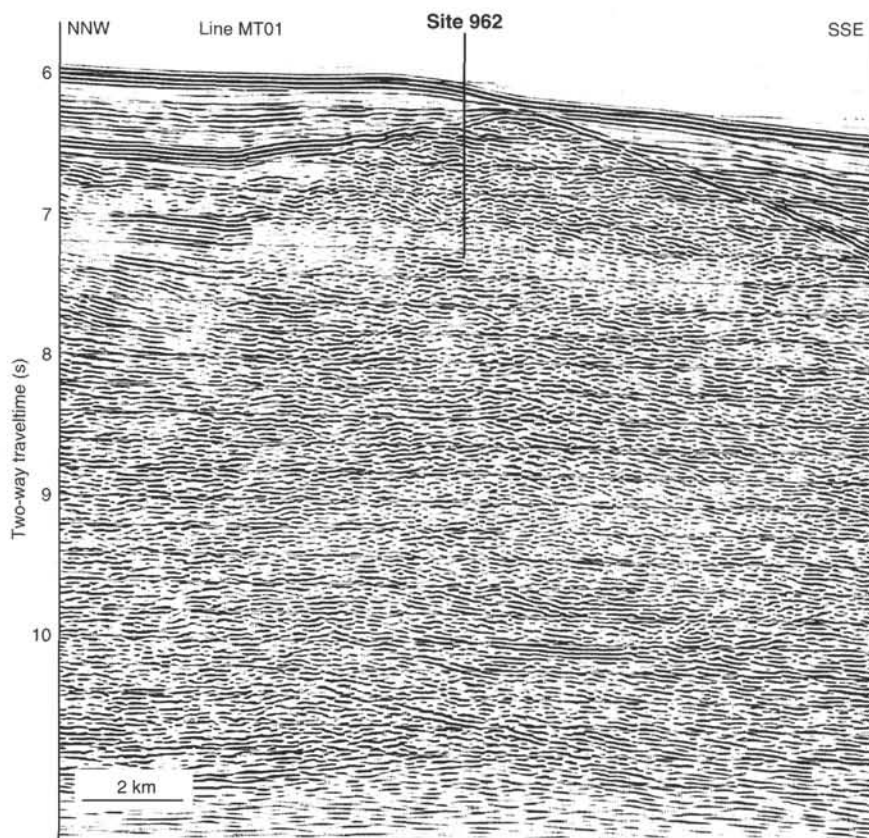


Figure 5. Detail of migrated MCS (96 channels) Line MT01 at Site 962 location. The seismic section shows an approximately 300-m-thick sediment cover pinching out against an acoustic basement made of discontinuous and contorted reflectors. Strongly reflective events can be detected at depth, with one at around 10.5 s TWT, possibly indicating the Moho.

Coring resumed with Core 159-962D-20R and continued until Core 159-962D-30R was recovered from a depth of 5002.3 m (345.3 mbsf). However, as this core was about to be completed the hole suddenly collapsed and the drill pipe became stuck. All attempts to circulate and/or rotate were unsuccessful. The pipe was worked until it could be moved downhole. Top drive rotation was then established, but the hole was still packed off around the drill string. After 1.25 hr, and overpulls of up to 100,000 lb, the pipe was freed. After

recovering Core 159-962D-30R it was decided to make a wiper trip to check conditions over the remaining portion of the hole. The top drive was set back and the drill string was pulled to a depth of 4760.0 m (103.0 mbsf). A continuous drag of 20,000–30,000 lb, with a maximum of 60,000 lb, was noted during the wiper trip. The pipe was run back into the hole to a depth of 4944.0 m (287.0 mbsf) where the top drive was picked up. The remaining portion of the hole was washed and reamed until the original total depth (TD) of 5002.3

Table 1. Site 962 coring summary.

Core	Date (1995)	Time (UTC)	Depth (mbsf)	Length cored (m)	Length recovered (m)	Recovery (%)
159-962A-1H	Feb 12	2355	0.0-3.7	3.7	3.71	100.0
Coring totals:				3.7	3.71	100.0
159-962B-						
1H	Feb 13	0105	0.0-7.5	7.5	7.47	99.6
2H	Feb 13	0205	7.5-17.0	9.5	9.57	101.0
3H	Feb 13	0320	17.0-26.5	9.5	9.55	100.0
4H	Feb 13	0530	26.5-36.0	9.5	9.86	104.0
5H	Feb 13	0630	36.0-45.5	9.5	9.86	104.0
6H	Feb 13	0810	45.5-55.0	9.5	10.08	106.1
7H	Feb 13	0915	55.0-64.5	9.5	9.41	99.0
8H	Feb 13	1030	64.5-74.0	9.5	9.99	105.0
9H	Feb 13	1145	74.0-83.5	9.5	9.14	96.2
10H	Feb 13	1315	83.5-93.0	9.5	0.42	4.4
11H	Feb 13	1500	93.0-93.3	0.3	0.06	20.0
12X	Feb 13	1710	93.3-94.3	1.0	0.01	1.0
13X	Feb 13	2030	94.3-100.0	5.7	0.18	3.2
Coring totals:				100.0	85.60	85.6
159-962C-						
		*** Drilled from 0.0 to 73.0 mbsf ***				
1R	Feb 14	2035	73.0-83.1	10.1	0.33	3.3
2R	Feb 15	0100	83.1-92.8	9.7	0.06	0.6
3R	Feb 15	1000	92.8-102.4	9.6	0.12	1.3
4M	Feb 15	1230		0.0	(0.07)	N/A
Coring totals:				29.4	0.51	1.7
Drilled:				73.0		
Total:				102.4		
159-962D-						
		*** Drilled from 0.0 to 75.1 mbsf ***				
1R	Feb 15	1745	75.1-84.7	9.6	0.10	1.0
2R	Feb 15	1915	84.7-94.4	9.7	0.08	0.8
3R	Feb 15	2050	94.4-104.1	9.7	0.20	2.1
4R	Feb 15	2230	104.1-113.7	9.6	0.12	1.3
5R	Feb 16	0025	113.7-123.4	9.7	0.15	1.5
6R	Feb 16	0240	123.4-133.0	9.6	0.53	5.5
7R	Feb 16	0445	133.0-142.7	9.7	0.61	6.3
8R	Feb 16	0700	142.7-152.4	9.7	0.13	1.3
9R	Feb 16	0900	152.4-162.0	9.6	7.68	80.0
10R	Feb 16	1135	162.0-171.7	9.7	3.54	36.5
11R	Feb 16	1430	171.7-181.3	9.6	2.16	22.5
12R	Feb 16	1700	181.3-191.0	9.7	8.24	84.9
13R	Feb 16	1935	191.0-200.7	9.7	2.63	27.1
14R	Feb 16	2230	200.7-210.3	9.6	0.00	0.0
15R	Feb 17	0105	210.3-220.0	9.7	0.21	2.2
16R	Feb 17	0345	220.0-229.6	9.6	4.20	43.7
17R	Feb 17	0605	229.6-239.1	9.5	0.28	3.0
18R	Feb 17	0900	239.1-248.8	9.7	5.94	61.2
19R	Feb 17	1130	248.8-256.4	7.6	2.44	32.1
		*** Drilled from 256.4 to 258.4 mbsf ***				
20R	Feb 18	0045	258.4-268.0	9.6	5.98	62.3
21R	Feb 18	0310	268.0-277.7	9.7	2.21	22.8
22R	Feb 18	0600	277.7-287.3	9.6	0.71	7.4
23R	Feb 18	0900	287.3-297.0	9.7	1.54	15.9
24R	Feb 18	1100	297.0-302.0	5.0	3.86	77.2
25R	Feb 18	1530	302.0-306.6	4.6	1.44	31.3
26R	Feb 18	1530	306.6-311.3	4.7	3.52	74.9
27R	Feb 18	1750	311.3-316.3	5.0	2.94	58.8
28R	Feb 18	2120	316.3-326.0	9.7	2.81	28.9
29R	Feb 19	0110	326.0-335.6	9.6	2.22	23.1
30R	Feb 19	0445	335.6-345.3	9.7	2.61	26.9
31R	Feb 19	1745	345.3-354.9	9.6	2.77	28.8
32R	Feb 19	2300	354.9-364.6	9.7	0.38	3.9
33R	Feb 20	0300	364.6-369.3	4.7	2.42	51.5
34R	Feb 20	0605	369.3-374.3	5.0	3.66	73.2
35R	Feb 20	1035	374.3-383.9	9.6	4.60	52.9
36R	Feb 20	1330	383.9-388.5	4.6	4.40	95.6
37R	Feb 20	1630	388.5-393.5	5.0	5.45	109.0
Coring totals:				316.4	92.76	29.4
Drilled:				77.1		
Total:				393.5		

m (345.3 mbsf) was reached. Two meters of fill was found at the bottom of the hole. At 1400 hr on 19 February RCB coring was again initiated and continued until 1645 hr on 20 February when the final depth of the hole was achieved at 5050.5 mbrf (393.5 mbsf). Coring was terminated to allow adequate time for logging the hole prior to abandonment.

Logging Operations

The top drive was set back and another "pre-logging" wiper trip with the drill pipe was made to 4760.0 mbrf (103.0 mbsf). As experienced earlier, there was moderate drag throughout the wiper trip, which reached a maximum of 80,000 lb overpull at one point. The drill pipe was run back in the hole and the top drive picked up at 4992.0 mbrf (335.0 mbsf). After reaming the lower portion of the hole to total depth, a 30-barrel Sepiolite mud pill was circulated from the bottom up and two successive wireline runs were made to release the bit and reverse-shift the sleeve. The drill pipe was then pulled to a logging depth of 4789.7 mbrf (132.7 mbsf). This depth was selected to put the drill pipe across the zone where excessive overpull had been experienced on the two previous wiper trips.

The first logging run was made with a reduced geophysical logging string comprising the phasor dual induction resistivity tool (DIT), lithodensity logging tool (HLDT), sonic digital logging tool (SDT), and the Natural Gamma spectrometry logging tool (NGT). The nuclear source was left out to eliminate any chance of loss in the hole and potential associated problems. This run was aborted when the tools would not pass 4809.0 mbrf (152.0 mbsf). The pipe was lowered to a depth of 4848.0 m (191.0 mbsf) using the circulating head, and the logging run was repeated. The tools reached 4988.0 mbrf (331.0 mbsf), within 62.5 m of bottom. Logging proceeded from that depth back to the drill pipe and was repeated before recovering the logging tools. Prior to running into the hole with the Formation MicroScanner (FMS) tool, the drill pipe was lowered an additional stand to 4876.6 m (219.6 mbsf), placing it across an area of bad hole conditions at 4868.0 mbrf or 211.0 mbsf. This was done to increase the chances that the FMS tool would reach the deeper, more scientifically interesting part of the hole. The FMS tool reached a depth of 4948.0 mbrf (291.0 mbsf). Two runs were made from that depth back to the end of the drill pipe. On all logging runs the drill pipe was raised an additional 20 m as the logging tools approached the end of their run.

While the FMS logging tools and sheaves were being rigged down, the circulating head was installed and Hole 962D was displaced with heavy mud. The drill string was pulled out of the hole, clearing the seafloor at 2400 hr on 21 February. At this point the aft (short) sandline was run into the pipe and coated with preservative. The positioning beacon was released and recovered. The drill string was tripped back to the rig floor and the drill collars/subs were magnafluxed, during which time the damaged coaxial TV cable was disposed of in preparation for installation of the new line during the Marseilles port call. While the pre-transit work was being completed, the thrusters were raised, and the ship was secured for the 2117-nmi voyage to Las Palmas, Canary Islands. At 1430 hr on 22 February the transit to port began.

SITE GEOPHYSICS

Site Survey

Site 962, which corresponds to proposed Site IG3, was included in the single-channel seismic survey shot at the beginning of Leg 159 (full details of the acquisition of these data are given in the "Underway Geophysics" chapter, this volume). Two passes were made over the site in a figure-eight pattern (Lines IG3-1 and IG3-2) before the third pass (IG3-3) along the same line as the first, during which the acoustic beacon was dropped (Fig. 6). Once the beacon had been deployed, a course was set for proposed Site IG2 (Site 961). Unfortunately the data from the first pass over the site (Line IG3-1) were lost during transfer to magnetic tape, so these data are unavailable for further processing and redisplay. However, Line IG3-3 is coincident with Line IG3-1, so two crossing passes over the site are still available. Line IG3-2 has a trend similar to multichannel Line MT01 from

the *Equasis* survey of 1990, whereas Line IG3-3 is subparallel to, and southeast of, single-channel Line IG37 (*Equamarge II* survey of 1988).

Unfortunately the data recorded at the beginning of Leg 159 are particularly noisy, and in the vicinity of Site 962 it is difficult to clearly distinguish any reflectors below the seabed on these profiles.

Integration of Seismic Profiles with Observations from the Site

The conversion from two-way traveltimes to depth for this site is based on discrete velocity measurements taken with the Digital Sound Velocimeter and the Hamilton Frame Velocimeter (see "Physical Properties" section, this chapter). Due to poor recovery from Hole 962D the velocity measurements for this site are sparse and rather variable and may not provide an accurate representation of the velocity structure. Although downhole measurements, including the sonic log, were recorded for part of Hole 962D, poor hole conditions mean that the sonic data are low quality and require considerable processing before they can be useful.

From the seismic data close to Site 962 two main reflectors can be identified: R1 and R2. These are shown in Figure 7 at the projected intersection of Site 962 and the closest points on multichannel Line MT01 and single-channel Line IG37. The single-channel data recorded at the beginning of Leg 159 are not shown in this figure because of their poor quality in the vicinity of Site 962. From Figure 7 the northwesterly offset of Line IG37 from Site 962 (Fig. 6) becomes apparent in the increased sediment thickness in the upper part of the section (above Reflector R1) compared to Line MT01 and drilling results at Site 962. Line MT01 also shows slightly thicker sediments in the upper part of the section than those calculated from the depths of interfaces and velocities at Site 962, indicating that this line is also offset from the site.

Reflector R1

Reflector R1 marks the base of an acoustically transparent unit below the seafloor (Fig. 7). This reflector probably corresponds to the interface between claystone and porcellanite in lithologic Subunit IIA at 55 mbsf (see "Lithostratigraphy" section, this chapter). The overlying section, of acoustically transparent claystones of late Pleistocene to early Miocene age, can be correlated to seismic Unit F (see "Site Geophysics" section, "Site 959" and "Site 961" chapters, this volume). The underlying unit contains laterally continuous reflectors that pinch out against the northern slope of the acoustic basement high. This unit corresponds to the porcellanite, radiolarian claystones, and palygorskite claystones of lithologic Subunits IIA and IIB.

Reflector R2

Reflector R2 corresponds to the cherts and porcellanites of lithologic Subunit IIC. This is a strong, laterally continuous reflector that can be traced over a wide area. However, on single-channel Line IG37 (Fig. 4) this reflector becomes more discontinuous in the region of Site 962. This observation agrees well with the single-channel data recorded at the beginning of Leg 159, where this strong reflector becomes considerably weaker in the vicinity of Site 962 (Fig. 8), which may result from a change in the mode of deposition of the cherts that are interbedded with thin claystone units in this area (see "Lithostratigraphy" section, this chapter). Unlike the Eocene cherts from Sites 960 and 961, the chert at Site 962 is late Albian to Cenomanian in age.

The top of the acoustic basement that corresponds to lithologic Unit III is defined by Reflector R2. The resolution of the seismic wavelet is not sufficient to delineate the top of lithologic Unit III as a

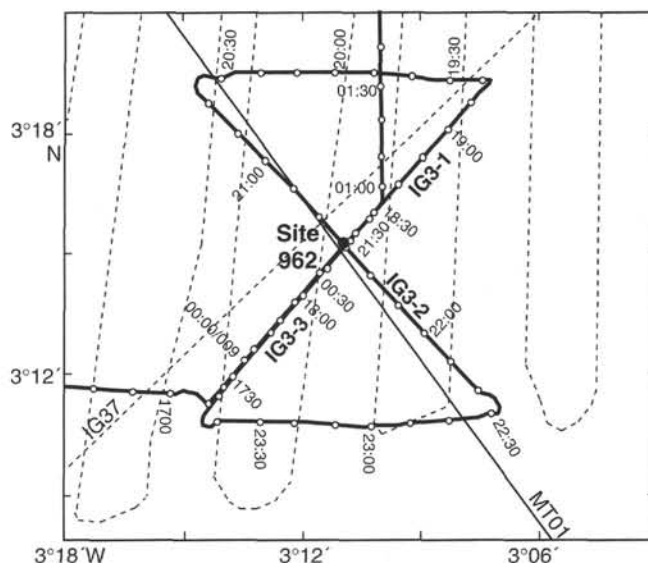


Figure 6. Track chart showing the location of Site 962 and the available seismic data close to the site. Thick lines show the single-channel seismic lines collected at the beginning of Leg 159. Thin lines show the multichannel data available from the *Equasis* survey of 1990. Dashed lines denote the single-channel lines from the *Equamarge II* survey of 1988.

separate reflector from the top of lithologic Subunit IIC, which has a maximum thickness of 48 m at Hole 962D. This acoustic basement is equivalent to seismic Unit A (see Basile et al., this volume) and comprises deformed claystones, siltstones, and sandstones of late Albian age. Seismic Unit A consists of short, discontinuous reflectors, and no internal structures can be defined within the unit.

The base of Hole 962D corresponds to a two-way traveltimes of 0.28 s below seafloor.

LITHOSTRATIGRAPHY

Four holes were drilled at Site 962. At Hole 962A, a mud-line core was taken and archived; thus this hole will not be discussed here. In Hole 962B, 100.0 m of stratigraphic section was cored; in Hole 962C, the top 73.0 m was drilled without coring, from which point coring continued to a total depth of 102.4 mbsf with very low recovery; in Hole 962D, the top 75.1 m was drilled without coring. RCB coring at Holes 962C and 962D yielded low recovery of most drilled intervals, and many of the cores were highly disturbed by drilling.

Three lithologic units were identified at Site 962 (Fig. 9; Table 2). These are, from top to bottom, lithologic Unit I comprising hemipelagic to pelagic silty clays, clays, and claystones (Pleistocene to late Miocene in age); lithologic Unit II, comprising biosiliceous sediment with radiolarians and diatoms, chert and porcellanite, and palygorskite claystone (early Miocene to late Albian in age), and lithologic Unit III, comprising siliciclastic sandstones, siltstones and claystones intermixed with limestones containing pelagic microfauna and -flora (late Albian in age).

Description of Lithologic Units

Unit I

Description: Silty clays with opal, micrite and plant debris, pyritic clay with quartz silt and plant debris, nanofossil clay, clay, and claystone with quartz silt

Interval: Sections 159-962B-1H-1, 0 cm, through 6H-1, 82 cm

Depth: 0-47.0 mbsf

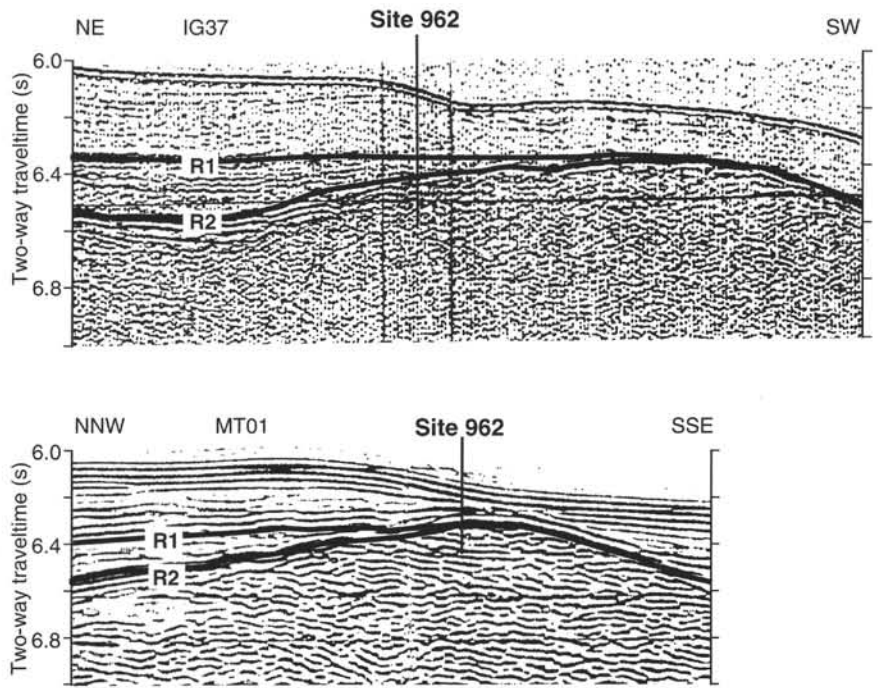


Figure 7. Projected intersection of Site 962 with the closest points on single-channel seismic Line IG37 and multichannel Line MT01. The sediments in the upper part of the section (above Reflector R1) are thicker along Line IG37, which passes to the northwest of the site. See Figure 6 for the location of the seismic lines.

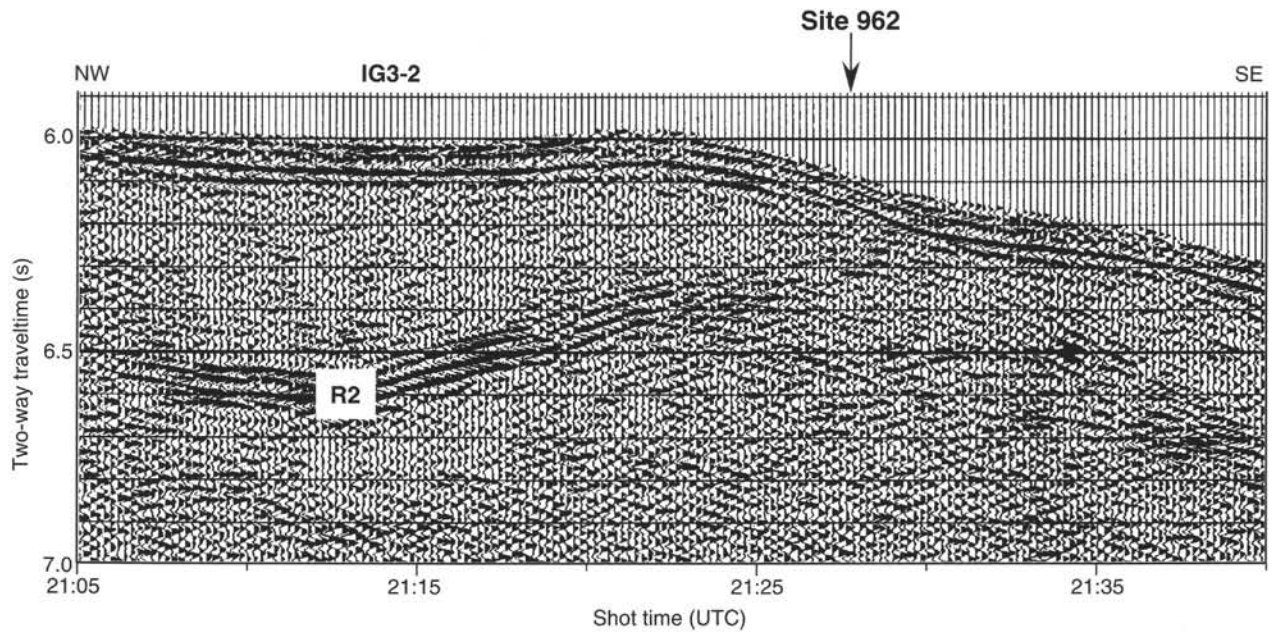


Figure 8. Part of single-channel seismic Line IG3-2 showing the decrease in amplitude of Reflector R2 close to Site 962. See Figure 6 for the location of the seismic profile.

Age: late Pleistocene to late Miocene

APC coring of lithologic Unit I yielded excellent recovery of a variety of silty clays, clays, and claystones, which were divided into two subunits on the basis of pelagic components, glauconite content, and the presence of goethite. Lithologic Subunit IA, late Pleistocene to early Pliocene in age, consists of silty clays with opal, micrite and plant debris, pyritic clay with quartz silt and plant debris, clay, and nannofossil clay. Lithologic Subunit IB has fewer pelagic components, is less glauconitic, and is early Pliocene to late Miocene in age. It comprises clay with quartz silt that grades downhole into claystone

with quartz silt and claystone. This subunit is characterized by the presence of goethite in many intervals. Although lithologic Unit I at this site comprises clays, rather than pelagic oozes as at Sites 959 through 961, it is temporally correlative with lithologic Unit I at those sites.

Subunit IA

Description: Silty clays with opal, micrite and plant debris; pyritic clay with quartz silt and plant debris; clay with nannofossils, and clay
 Interval: Sections 159-962B-1H-1, 0 cm, through 3H-CC, 26 cm

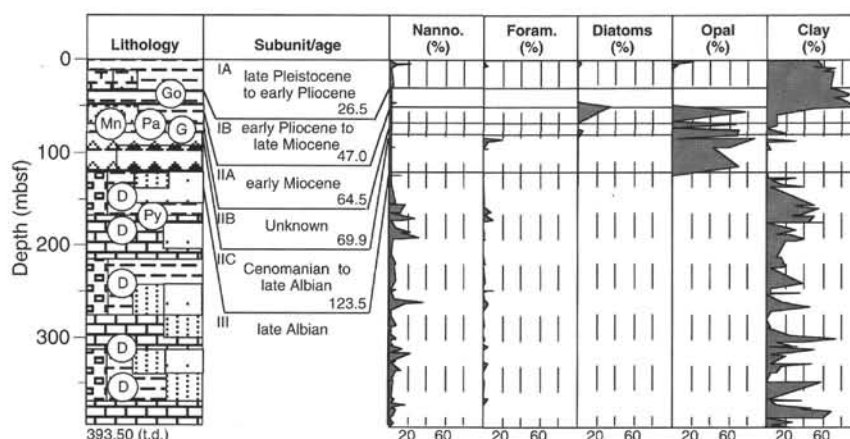


Figure 9. Stratigraphic column for Site 962.

Table 2. Lithologic units for Site 962.

Unit	Subunit	Cored interval	Depth interval (mbsf)	Thickness (m)	Lithology	Age (Epoch)
I	A	159-962B-1H, 0 cm, to 3H-CC, 26 cm	0–26.5	26.5	Silty clays with opal, micrite, and plant debris; pyritic clay; and clay with nannofossils (more pelagic components and glauconite)	late Pleistocene to early Pliocene
	B	159-962B-4H-1, 0 cm, to 6H-1, 82 cm	26.5–47.0	20.5	Clay and claystone with quartz silt and claystone (goethite-bearing)	early Pliocene to late Miocene
II	A	159-962B-6H-1, 82 cm, to 7H-7, 41 cm	47.0–64.5	17.5	Radiolarian claystone with diatoms, claystone with radiolarians and diatoms, porcellanite with clay	early Miocene
	B	159-962B-8H-1, 0 cm, to 8H-4, 90 cm	64.5–69.9	5.4	Palygorskite claystone, manganese hardground, glauconitic silty sandstone	Unknown
III	C	159-962C-1R-1, 0 cm, to 1R-CC, 11 cm	73.0–83.1	10.1	Chert and porcellanite	Cenomanian–late Albian late Albian late Albian late Albian
		159-962B-8H-4, 90 cm, to 13X-CC, 18 cm (TD)	69.9–100.0	30.1		
		159-962C-2R-1, 0 cm, to 3R-CC, 12 cm (TD)	83.1–102.4	19.3		
		159-962D-1R-1, 0 cm, to 6R-1, 7 cm	75.1–123.5	48.4		
III		159-962D-6R-1, 7 cm to 37R-CC, 10 cm (TD)	123.5–393.5	270.0	Claystones with quartz silt, micrite, and nannofossils; clayey siltstone with micrite and nannofossils; calcite-cemented sandstone; calcite-cemented quartz sandy siltstone; limestone; and limestone with quartz sand and silt	late Albian

Note: TD = total depth

Depth: 0–26.5 mbsf
Age: late Pleistocene to early Pliocene

The top 7.5 m of Subunit IA is dominated by alternating beds of dark gray, silty clay with opal and silty clay with micrite. This slightly bioturbated interval also contains thin beds of somewhat lighter gray clay with nannofossils and micrite, and dark brown silty clay with nannofossils and diatoms. It is succeeded downhole by black to dark gray pyritic clay with silt and plant debris, interbedded with medium greenish gray silty clay with plant debris, from 7.5 to 17.0 mbsf. This interval is slightly to moderately bioturbated. Generally, pyrite occurs as disseminated framboids, nodules, or burrow fills. In many intervals, however, pyrite locally comprises up to 25% of the sediment. Smear slide samples from Cores 159-962B-1H and 2H (0–17.0 mbsf) indicate the presence of semiconsolidated fragments of claystones and siltstones in the sediments, which were probably redeposited from older rocks during the Pleistocene. The major lithology from 17.0 to 26.5 mbsf is an interbedded dark greenish gray clay and lighter greenish gray nannofossil clay. Minor lithotypes are nannofossil glauconite clay with foraminifers and micrite, and clayey nan-

nofossil ooze with foraminifers. Glauconite occurs in Subunit IA as thin color bands and burrow fills.

Subunit IB

Description: Clay with quartz silt, claystone with quartz silt, and claystone
Interval: Sections 159-962B-4H-1, 0 cm, through 6H-1, 82 cm
Depth: 26.5–47.0 mbsf
Age: early Pliocene to late Miocene

The boundary between Subunits IA and IB is marked by the first occurrence of goethite (Fig. 10), a reduction in the pelagic components and glauconite content of the clayey sediments, and a change in magnetic properties (see "Paleomagnetism" section, this chapter). Organic geochemistry and XRD data show that this subunit is devoid of carbonate material (see "Organic Geochemistry" section, this chapter). Lithologic Subunit IB consists of greenish gray clay with quartz silt and light olive brown clay with quartz silt, which grade downcore into light olive brown to olive brown claystone with quartz silt and grayish green claystone. The olive brown layers are common-

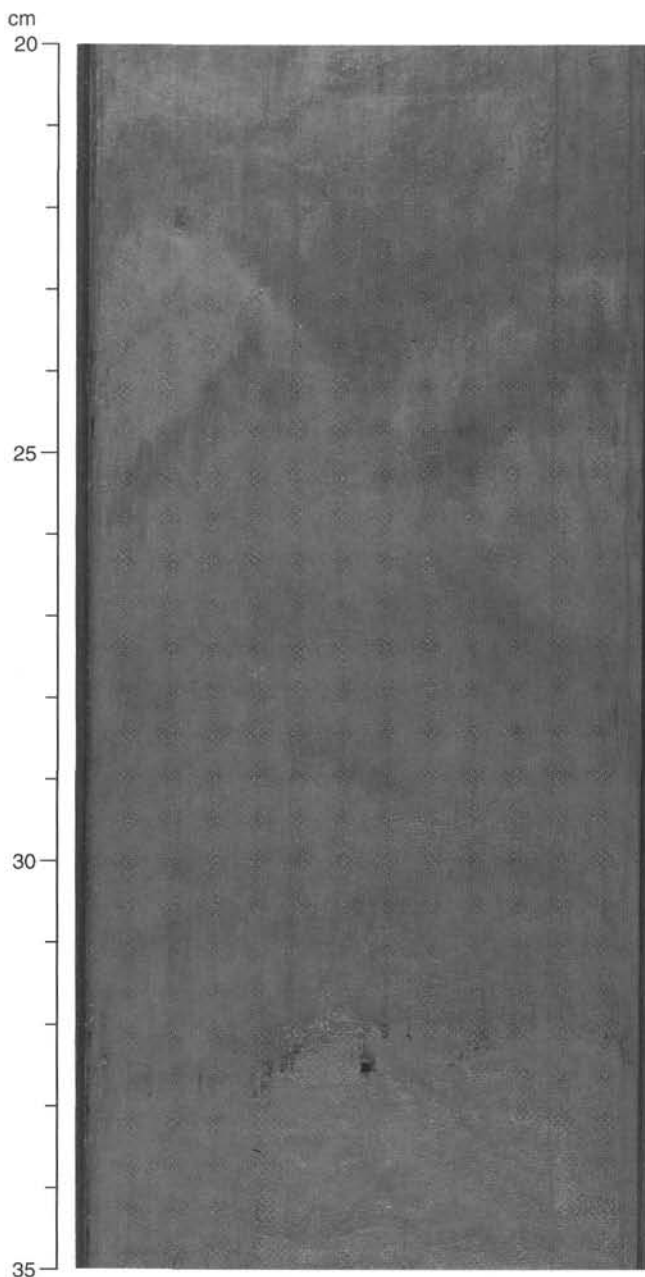


Figure 10. Section 159-962B-4H-2, 20–35 cm, stringers and subhorizontally aligned goethite (and hematite?) enrichments in the goethitic clay of lithologic Subunit IB.

ly goethite bearing. XRD data from these olive-colored clays and claystones with quartz silt show the dominance of kaolinite and the presence of gibbsite in these sediments (Fig. 11). Lithologic Subunit IB is slightly to heavily bioturbated, and the burrows are filled with goethite and pyrite.

Unit II

Description: Radiolarian claystone with diatoms, claystone with radiolarians and diatoms, porcellanite with clay, palygorskite claystone, glauconitic silty sandstone, chert, and porcellanite

Interval: Sections 159-962B-6H-1, 82 cm, through 13X-CC, 18 cm (TD), 159-962C-1R-1, 0 cm, through 3R-CC, 12 cm (TD), and 159-962D-1R-1, 0 cm, through 6R-1, 7 cm

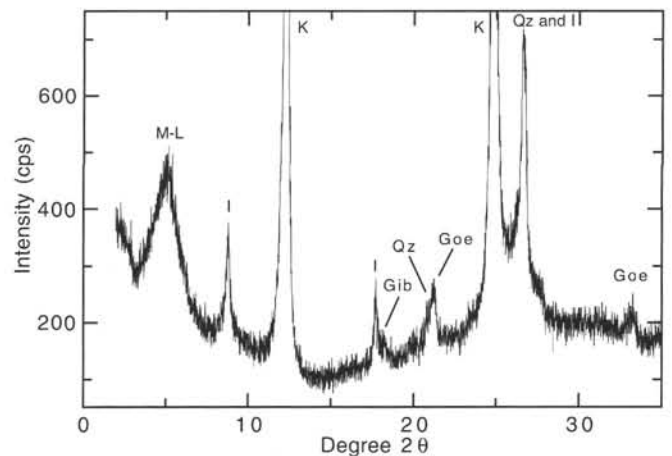


Figure 11. X-ray diffractogram of glycolated clay separate from Sample 159-962B-4H-2, 45–46 cm, from the brownish clay in lithologic Subunit IB. The kaolinite (K) strongly dominates the mineral assemblage, which contains additional illite-smectite mixed-layer mineral (M-L) which expands to 17-Å, discrete illite (I), goethite (Goe), quartz (Qz), and traces of gibbsite (Gib).

Depth: 47.0–100.0 mbsf (TD), Hole 962B; 73.0–102.4 mbsf (TD), Hole 962C; 75.1–123.5 mbsf, Hole 962D
Age: early Miocene to late Albian

Lithologic Unit II, which was cored in all three holes from this site, comprises a varied silica-rich and/or diagenetic lithology that was divided into three subunits on the basis of their bulk mineralogy. The boundary between lithologic Units I and II is marked by a change in magnetic properties (see “Paleomagnetism” section, this chapter). Lithologic Subunit IIA, of early Miocene age, consists of grayish claystone which alternates with claystones characterized by variable admixtures of siliceous microfossils (diatoms and radiolarians) and glauconite, and with porcellanite with claystone. Lithologic Subunit IIB, of unknown age, consists of bluish-green palygorskite clay, a dark brown manganese crust, and glauconitic silty sand. Lithologic Subunit IIC, which was poorly recovered, has a chert and porcellanite and minor interbedded clayey lithology. It ranges in age from Cenomanian to late Albian.

Subunit IIA

Description: Radiolarian claystone with diatoms, claystone with radiolarians and diatoms, and porcellanite with clay

Interval: Sections 159-962B-6H-1, 82 cm, through 7H-7, 41 cm

Depth: 47.0–64.5 mbsf

Age: early Miocene

The upper 8.6 m of lithologic Subunit IIA is dominated by light grayish green to grayish green claystone, which is interbedded or dissected by subhorizontal burrows infilled with radiolarian claystone with diatoms and claystone with radiolarians and glauconite. Below 55 mbsf, the sediment turns into green to grayish green porcellanite with clay that contains some zeolite. The entire subunit is marked by the lack of carbonate and by the intercalation of numerous glauconitic color bands or hardgrounds. Furthermore, pyrite and, toward the base, marcasite, are commonly disseminated throughout the sediment.

Subunit IIB

Description: Palygorskite claystone, nodular manganese crust, and glauconitic silty sandstone

Interval: Sections 159-962B-8H-1, 0 cm, through 8H-4, 90 cm, and 159-962C-1R-1, 0 cm, through 1R-CC, 11 cm

Depth: 64.5–69.9 mbsf, Hole 962B; 73.0–83.1 mbsf, Hole 962C

Age: Unknown

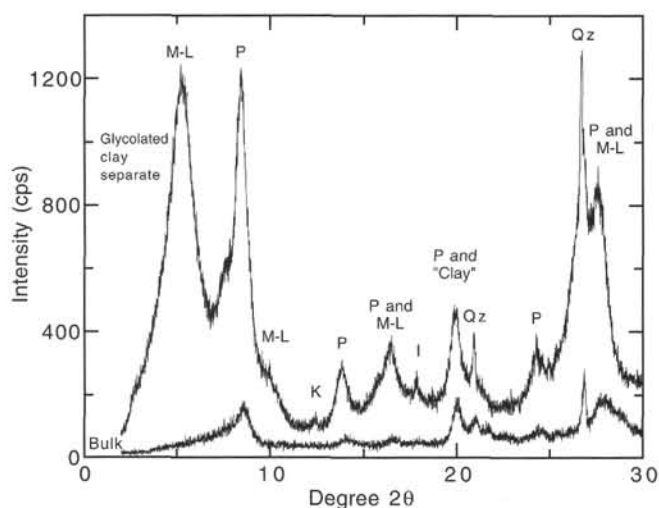


Figure 12. X-ray diffractogram of Sample 159-962B-8H-2, 85–86 cm, from the bluish green claystone at the top of lithologic Subunit IIB. Palygorskite (P) has a prominent peak at 10.5 Å and some minor reflections at 6.4, 5.4, 4.45, and 3.65 Å. The palygorskite peaks at 5.4 and 3.18 Å are superimposed by the reflections of a highly expandable 17-Å illite-smectite mixed-layer mineral (M-L). Kaolinite (K) and probably some illite (I) occur in minor amounts. Note the presence of sharp quartz (Qz) peaks at 3.34 and 4.25 Å.

The top of lithologic Subunit IIB consists of greenish gray, slightly bluish palygorskite claystone with several moderately bioturbated intervals and faint color banding. XRD analysis revealed dominant palygorskite and highly expandable illite-smectite mixed-layer minerals together with significant amounts of quartz and minor kaolinite (Fig. 12). Quartz silt has also been observed in smear slides (e.g., Sample 159-962B-8H-3, 58–59 cm). Pyrite crystals are widely scattered. The palygorskite clay is barren of microfossils, but similar deposits at Sites 960 and 961 all belong to the early Eocene nannofossil Zone CP10. In Hole 962C, a 7-cm-thick interval (Section 159-962C-IR-1, 14–21 cm) of dark brown, nodular manganese oxide crust occurs at the base of the palygorskite claystone. This crust is underlain by glauconite pellet-rich claystone, which contains a 3 × 4 cm, yellowish brown chert nodule stained by iron oxyhydroxides. The nodule is rimmed by a dark (phosphatic?) mineral. A Mn crust is not present or was not recovered in Hole 962B, where the palygorskite claystone is underlain directly by porcellanite with glauconite, similar to the sediment that occurs with the chert nodule in Hole 962C.

Layered glauconitic hardgrounds in Sections 159-962B-8H-3, 140 cm, through 8H-4, 90 cm, include intervals with dark glauconitic pebbles and pyrite nodules (Fig. 13). The lower boundary of lithologic Subunit IIB corresponds to the first occurrence of dark, bedded chert.

Subunit IIC

Description: Chert and porcellanite

Interval: Sections 159-962B-8H-4, 90 cm, through 13X-CC, 18 cm (TD), 159-962C-2R-1, 0 cm, through 3R-CC, 12 cm (TD), and 159-962D-1R-1, 0 cm, through 6R-1, 7 cm

Depth: 69.9–100.0 mbsf, Hole 962B; 75.1–102.4 mbsf, Hole 962C; 148.1–123.4 mbsf, Hole 962D

Age: Cenomanian to late Albian (Hole 962B) and late Albian (Holes 962C and 962D)

Lithologic Subunit IIC was drilled in all Site 962 holes but generally yielded very poor recovery (see "Operations" section, this chapter). The boundary between lithologic Subunits IIB and IIC was defined as the last occurrence of glauconite in lithologic Subunit IIB

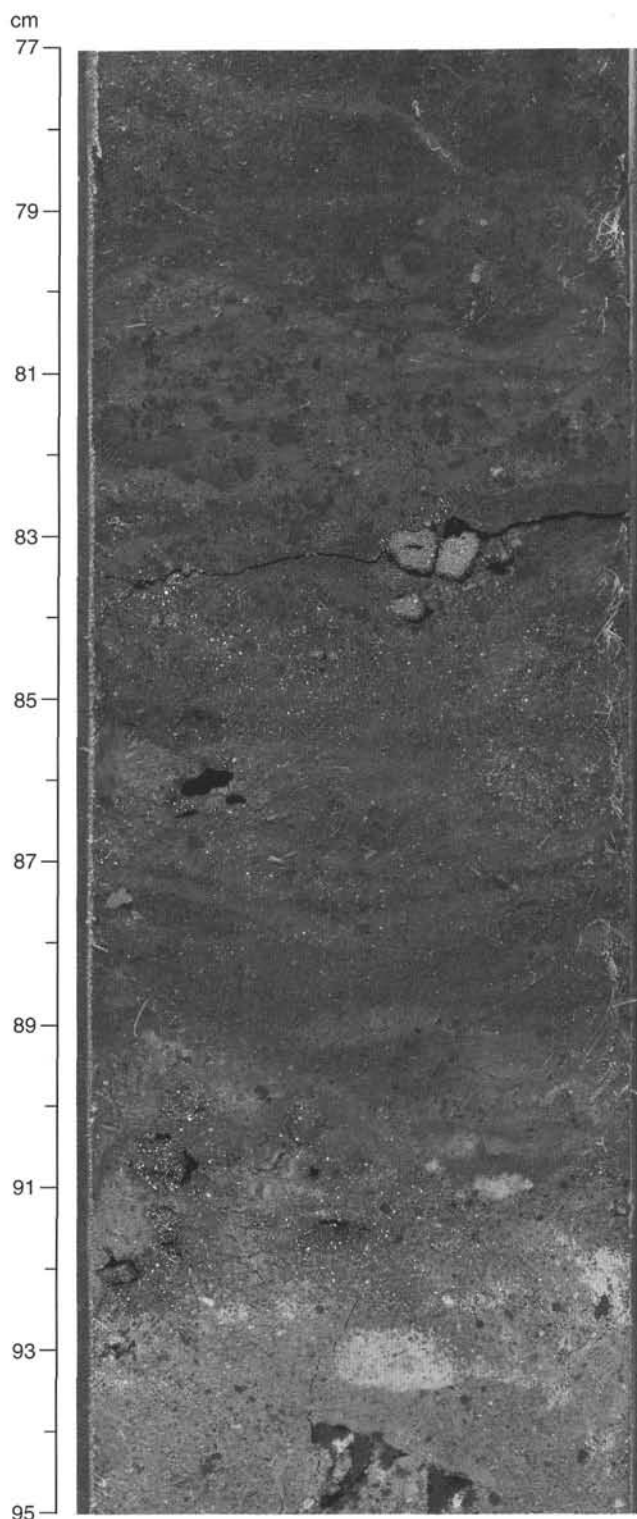


Figure 13. Section 159-962B-8H-4, 77–95 cm. The base of the glauconitic hardground at 90 cm marks the boundary between lithologic Subunits IIB and IIC. The hardground is irregularly layered with some layers consisting of glauconitic pellets. Pyrite nodules are common. Below 90 cm, the sediment consists of a breccia of dark chert in a porcellanitic and clayey matrix.

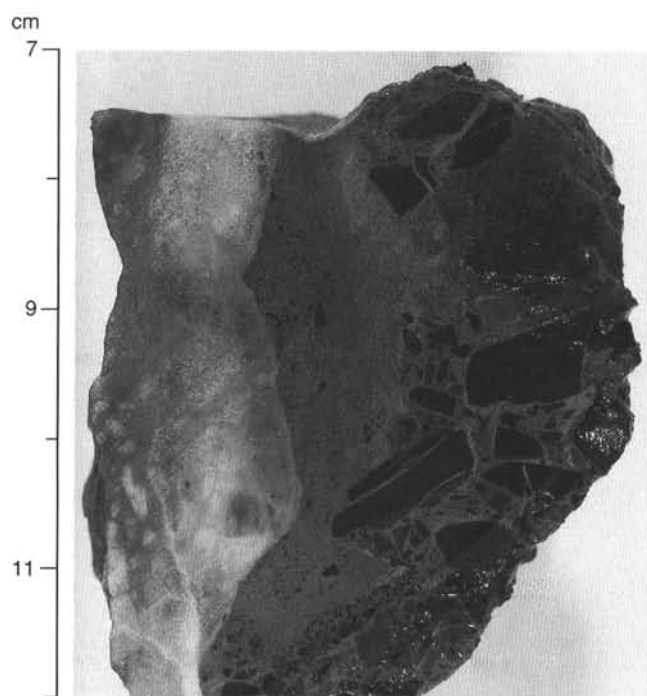


Figure 14. Section 159-962D-3R-CC, 7–12 cm. Veined chert breccia of fragments of dark chert floating in a lighter porcellanite matrix. The matrix is cut by a calcite vein.

and the first occurrence of dark chert in lithologic Subunit IIC (Fig. 13). In Hole 962B, from 74.0 to 96.9 mbsf, the chert is chaotically intermixed with porcellanitic and clayey sediment. Pieces of chert in this interval are mostly dark gray or green and some of them show rims of whitish haloes.

In Core 159-962B-9H, where recovery is comparatively high, dark olive gray chert is interbedded with porcellanite containing pyrite and clay. Several generations of fractures in the porcellanites and the cherts have been filled by light brown to clear chert. Organic carbon values are remarkably high in this interval, and, in agreement with optical estimates, the C/N ratio and HI parameter point to a mainly terrestrial source of organic matter (see “Organic Geochemistry” section, this chapter). Core 159-962B-10H is similar to that above, but nannofossil foraminifer claystone with pyrite occurs as the matrix of a drilling breccia. This claystone may have formed the interbeds between the chert prior to drilling disturbance.

Cores 159-962B-11H through 13X consist of a few centimeter-sized pieces of chert and porcellanite, which are commonly fractured and were subsequently annealed by clear chert. Locally, fracturing results in brecciation (Fig. 14), where fragments of chert are supported by a porcellanitic matrix with calcite, and a later-stage generation of calcitic veins cut through the breccia. Significant amounts of silt-size, rhombic dolomite crystals occur in the dolomitic porcellanite in Core 159-962B-13X.

The lower boundary of lithologic Unit II is defined as the first downhole occurrence of siliciclastic lithologies. Chert fragments found below the boundary are probably related to caving of the borehole.

Unit III

Description: Claystone with quartz silt, micrite and nannofossils; clayey siltstone with micrite and nannofossils; calcite-cemented sandstone; calcite-cemented quartz sandy siltstone; limestone; limestone with quartz sand; and limestone with quartz silt

Interval: Sections 159-962D-6R-1, 7 cm, through 37R-CC, 10 cm (TD)
Depth: 123.5–393.5 mbsf
Age: late Albian

Lithologic Unit III is 270 m thick and entirely restricted to Hole 962D. It comprises dark olive gray to dark brownish gray claystone with quartz silt and micrite, clayey siltstone with micrite, calcite-cemented sandstones and quartz sandy siltstones, and limestones. The upper boundary of this unit is defined by the first occurrence of light gray, calcite-cemented, clayey sandstones beneath the cherts and porcellanites of lithologic Unit II. Pure limestones are rare. Most contain some quartz sand and silt. Throughout lithologic Unit III, the intercalated siliciclastics are rich in carbonate. The type and frequency of sedimentary structures and bed forms in lithologic Unit III show no significant change with depth.

The claystones of Unit III are massive to laminated and contain some silt to very fine-grained sand. This coarser material either is dispersed within the massive claystones or forms laminae or small-scale ripple-laminated horizons. In the upper part of the unit, claystones contain up to 25% calcareous microfossils, which are dominantly nannofossils (Fig. 9). Downhole, the claystones contain fewer nannofossils even though the carbonate content remains relatively constant throughout lithologic Unit III. This carbonate, however, consists of micrite and authigenic dolomite. Clay mineral assemblages predominantly consist of illite-smectite mixed-layer minerals and kaolinite (Fig. 15) with chlorite in the upper part of the unit (Sample 159-962D-9R-1, 24–25 cm) and hence are interpreted as detrital. Clay composition shows no significant systematic changes downhole. Organic matter is a significant component of the clay-rich sediments and imparts a dark olive gray to dark brown color (see “Organic Geochemistry” section, this chapter). Dolomite is generally present in claystones and siltstones, up to 30%; however, clayey dolomite interbeds also occur associated with limestone-rich intervals (Cores 159-962D-12R, 13R, and 37R). Some disseminated pyrite is present throughout lithologic Unit III. Pyritic nodules occur only in the upper part of the unit (Cores 159-962D-9R through 11R).

Limestones in lithologic Unit III occur in distinctive intervals. Going downhole, the first pure limestones are present in Core 159-962D-11R at 172.5 mbsf. Limestones with quartz sand and silt are abundant in the intervals 180–220, 287–310 mbsf, and downhole from 345 mbsf. They are typically horizontally laminated and locally show small basal scours (e.g., Sections 159-962D-33R-1, 52–53 cm, and 34R-1, 43–44 cm). Lamination is commonly overlain by isolated ripples or cross-lamination which, in turn, is overlain by laminated to massive, fine-grained limestones or micritic claystones (Fig. 16). In fine-grained portions, lenticular bedding is present and some coarser quartz sandy limestone laminae form individual 5- to 10-cm-thick beds (Fig. 17). Thin, fining-upward sequences are present in Cores 159-962D-25R, 26R, and 31R. Limestones consist of sparry and micritic carbonate, uniserial benthic and planktonic foraminifers, quartz sand, and silt. Limestones in Core 159-962D-11R consist dominantly of micrite with foraminifers replaced by sparry calcite. Carbonate content generally varies between 50% and 75%, with a maximum of 95% (see “Organic Geochemistry” section, this chapter). Variation in the abundance of siliciclastic components results in color changes, from dark to light gray, in these fine- to medium-grained limestones. Organic matter content in the limestones of lithologic Unit III is distinctly high but is slightly lower in micritic claystones.

Predominantly siliciclastic intervals occur at 124–170, 220–248, and 317–326 mbsf. Calcite-cemented sandstones show parallel lamination or small-scale cross-lamination (Fig. 18). In the upper part of lithologic Unit III, sandstones are cross-bedded with some slightly upward-curved, small-scale foreset laminae (Fig. 19). Thin layers or laminated portions of grayish, siliciclastic, very fine- to fine-grained sandstones are also associated with otherwise limestone-rich intervals (Cores 159-962D-11R, 25R, 31R, 35R, and 36R). In Section

159-962D-12R-4, normally graded to laminated, clayey quartz siltstone alternates with thickly laminated micritic limestone with nanofossils (Fig. 20). Typical framework grains include subangular to subrounded quartz, plagioclase, and some microcline. The matrix consists of calcite spar cement, micrite, and dolomite.

Veining occurs sporadically throughout lithologic Unit III. The filling mineral is dominantly calcite, although occasionally, filling is by fine-grained sediment (Fig. 18) or by pyrite (Core 159-962D-12R). In some intervals, bedding is steep or nearly vertical (see "Structural Geology" section, this chapter), making the succession slightly thicker than the original depositional thickness.

Discussion

At Site 962, we recognized the following depositional sequences:

1. a thick series resulting from low-concentration turbidity currents transporting mixed carbonate and siliciclastic sediments into a hemipelagic environment above the CCD, where anaerobic or dysaerobic conditions at the seabed were probably related to high accumulation rates (lithologic Unit III);
2. biosiliceous sediments and their alteration products that formed during periods of high productivity are interrupted by a major hiatus that may have spanned most of the Upper Cretaceous and part of the lower Paleogene. During this period, the depositional environment passed from above to below the CCD (lithologic Unit II);
3. hemipelagic to pelagic sediments, generally free of both calcareous and siliceous components, which were deposited in a sub-CCD setting that recorded periods of increased terrigenous sediment input.

Sediments of lithologic Unit III are interpreted as distal turbidite sequences comprising sands, sandy limestones, and clays. Dark, fine-grained, massive micritic claystones with nanofossils and some quartz silt represent hemipelagic sedimentation, whereas the laminated equivalents reflect periodic transport of material by low-concentration turbidity currents. Anaerobic or dysaerobic conditions associated with a high sedimentation rate are inferred from the excellent preservation of centimeter- to millimeter-scale lamination and organic matter (Byers, 1977; Scholle et al., 1983). The presence of benthic foraminifers and calcareous nanofossils indicates deposition above the CCD. The presence of quartz sand and silt in the limestones indicates mixed sediment sources. Some carbonate was probably derived from shallow shelf areas, and the siliciclastic components may be derived from continental sources redeposited downslope through submarine canyons. This sediment was intermixed with pelagic calcareous material prior to and/or during transport by periodic density flows. Identified Bouma sequences (T_{bde} , T_{cde} , T_{de}) in the limestones and sandstones lack the basal part (T_b) and generally also the middle parts of a Bouma sequence (T_b). The beds resemble the facies D2.1 and D2.2 of Pickering et al. (1986, 1989), which were interpreted as having been transported by low-concentration turbidity currents. Scattered individual laminations, gradational lower bases, and lack of clear grading or fining-upward successions may indicate additional bottom-current reworking of the material.

The stacked succession of more than 270 m of similar basinal sediment of Unit III suggests a high sedimentation rate for the late Albian, probably related to active tectonism characterized by constant sediment input, coupled with a continuously subsiding basin. The subangular to subrounded quartz grains indicate that the sediments were probably recycled from preexisting sedimentary sources. The presence of kaolinite indicates relatively intense weathering conditions for the source area.

The onset of chert and porcellanite deposition in lithologic Unit II records a significant break in the supply of detrital material. Biosili-

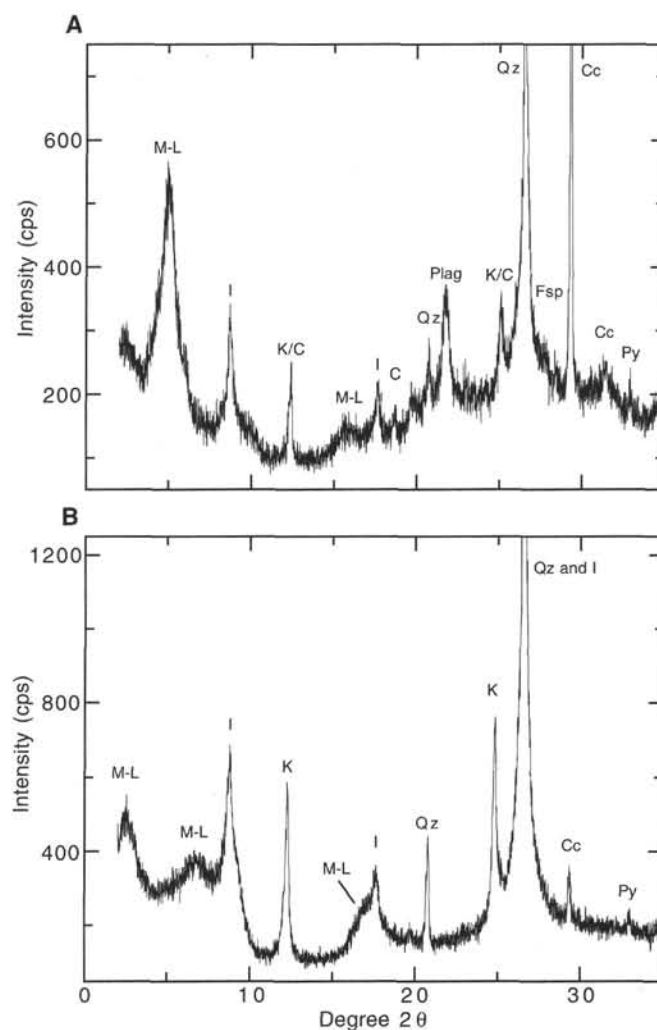


Figure 15. X-ray diffractogram of glycolated clay separates of samples from lithologic Unit III. **A.** Sample 159-962D-9R-1, 24–25 cm. The sample contains large amounts of quartz (Qz), calcite (Cc), and feldspar (Fsp). A reflection at 4.08 Å is characteristic of plagioclase (Plag), but K-feldspars may be present as well. The clay mineral assemblage consists of an illite-smectite mixed-layer mineral (M-L) that expands to 17 Å, discrete illite (I), chlorite (C), and probably some kaolinite (K). Although the strong peaks at 7.14 and 3.55 Å can be interpreted as kaolinite, the presence of chlorite is indicated by a small, but significant, reflection at 4.74 Å. The co-occurrence of highly expandable mixed layers with chlorite points to a detrital rather than a diagenetic origin of the latter. Minor diagenetic pyrite (Py) is also noted. **B.** Sample 159-962D-26R-2, 35–37 cm. The clay mineral assemblage consists of kaolinite, illite, and an illite-smectite mixed-layer mineral that expands to about 13 Å and has a superstructure peak at about 35 Å, indicative of R-1 ordering (Moore and Reynolds, 1989). Quartz, calcite, and pyrite occur additionally. Conventions as in Figure 15A.

ceous deposits and their alteration products (porcellanite, chert, and zeolite), have been interpreted as representing periods of increased organic productivity (see "Principal results" sections in "Site 959," "Site 960," and "Site 961" chapters, this volume), which have Eocene (Sites 960 and 961) or Oligocene (Site 959) ages. At Site 962, however, the chert and porcellanite are late Albian to Cenomanian in age. Biosiliceous sedimentation was temporarily interrupted in the middle Cretaceous, as indicated by the overlying interval of alternating glau-

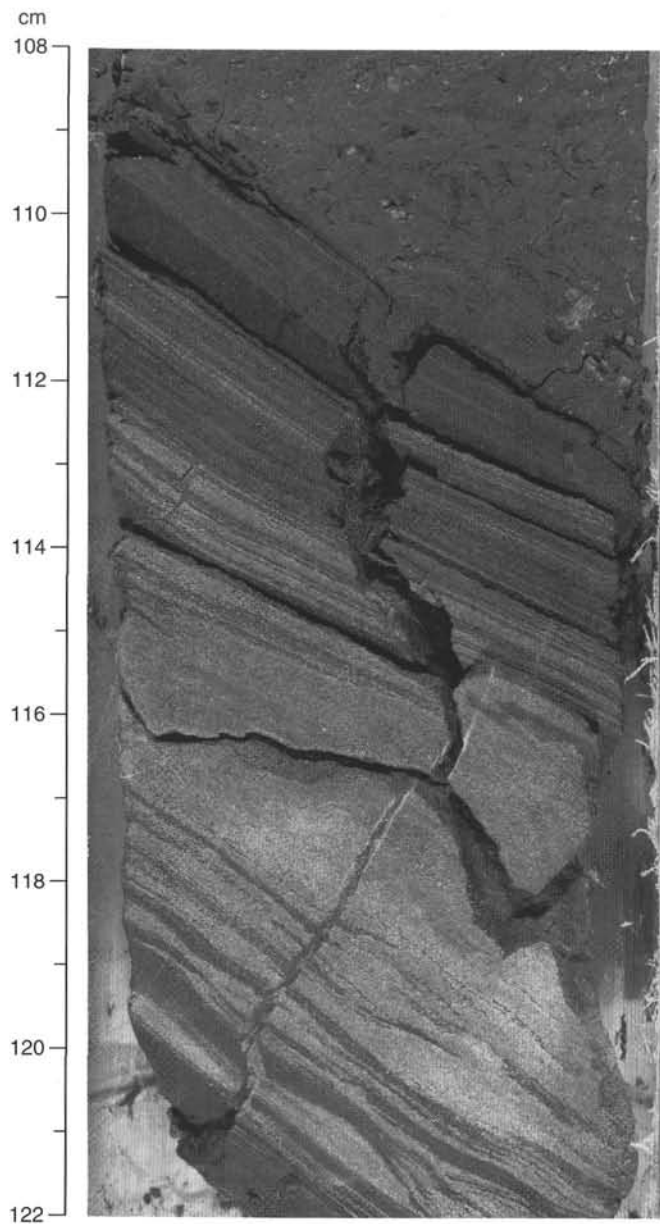


Figure 16. Section 159-962D-25R-1, 108–122 cm, lamination in quartz sandy limestone associated with rippled, slightly coarser intervals in the middle and overlain by laminated to massive fine-grained limestone and micritic claystone.

conite hardgrounds and porcellanite with glauconite, which yielded a Turonian or older age (see “Biostratigraphy” section, this chapter). The sediment-starved or nondepositional period necessary for the formation of the glauconitic hardgrounds is poorly constrained in time because the overlying palygorskite claystone is also barren of nanofossils; however, this represents a very long period of time. Manganese crusts and nodules, such as the one that separates palygorskite claystone and glauconite claystone in Core 159-962B-1R, grow only a few millimeters per million years and require extremely low sedimentation rates (Heath, 1981). Taken together, the glauconite hardgrounds and the nodular Mn-crust represent a long hiatus in a sub-CCD environment that was constantly swept by bottom currents that winnowed the hardground surface.

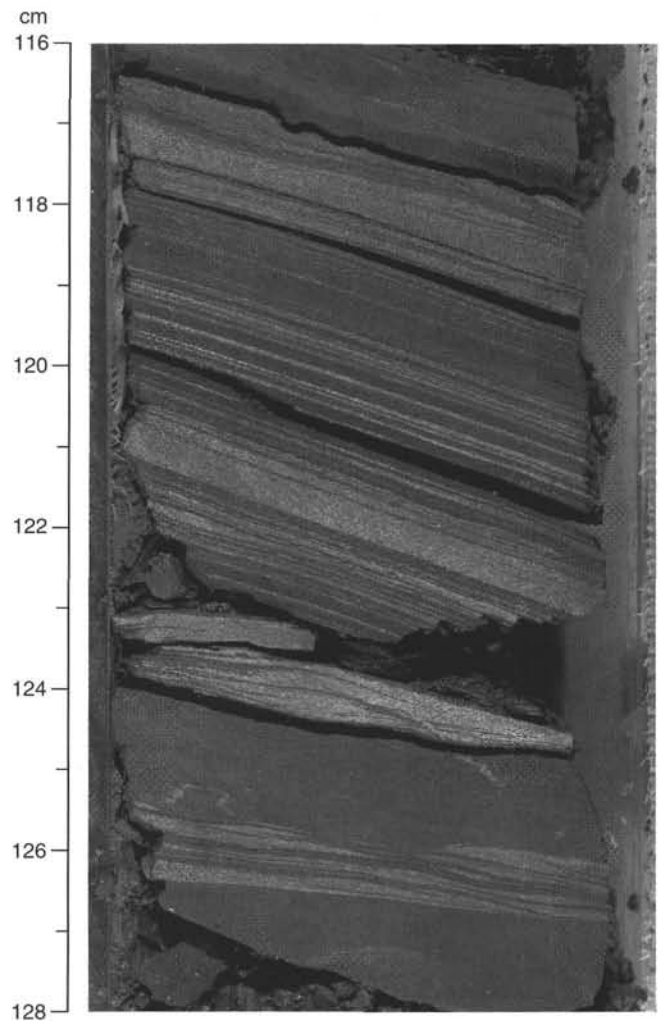


Figure 17. Section 159-962D-29R-1, 116–128 cm, limestone-bearing intervals showing lenticular bedding. Coarser quartz sandy limestone laminae are seen as individual 5- to 10-mm-thick beds.

Palygorskite claystone, which forms the upper part of lithologic Subunit IIB, is similar to the lithologies recovered at Sites 960 and 961 (see “Principal results” section, “Site 960” and “Site 961” chapters, this volume), where it was restricted to the lower Eocene nanofossil Zone CP 10, although no barite was found at Site 962. Also, faulting was prominent in the claystone in Hole 962B, whereas no tectonic deformation of this lithology was recorded at the other sites. Although it is tempting to place the palygorskite claystones at Site 962 at the same stratigraphic level as the other palygorskite clay intervals, an older or a younger age cannot be excluded because the sediment itself is barren of microfossils. Several hypotheses have been put forward for the formation of palygorskite claystone at Sites 960 and 961, which include authigenic formation in a very shallow-water or terrestrial environment, authigenic formation in a deep-water environment, or the erosion of shallow-water palygorskite and its transport into deep water. At Site 962, the occurrence of detrital quartz silt and the presence, though in minor amounts, of kaolinite, points to a detrital input during deposition of the palygorskite clay. The lack of microfossils, however, hampers the interpretation of this undated deposit in terms of depositional environment.

Increased sedimentary input resumed with the deposition of clays with siliceous microfossils and porcellanites of lithologic Subunit

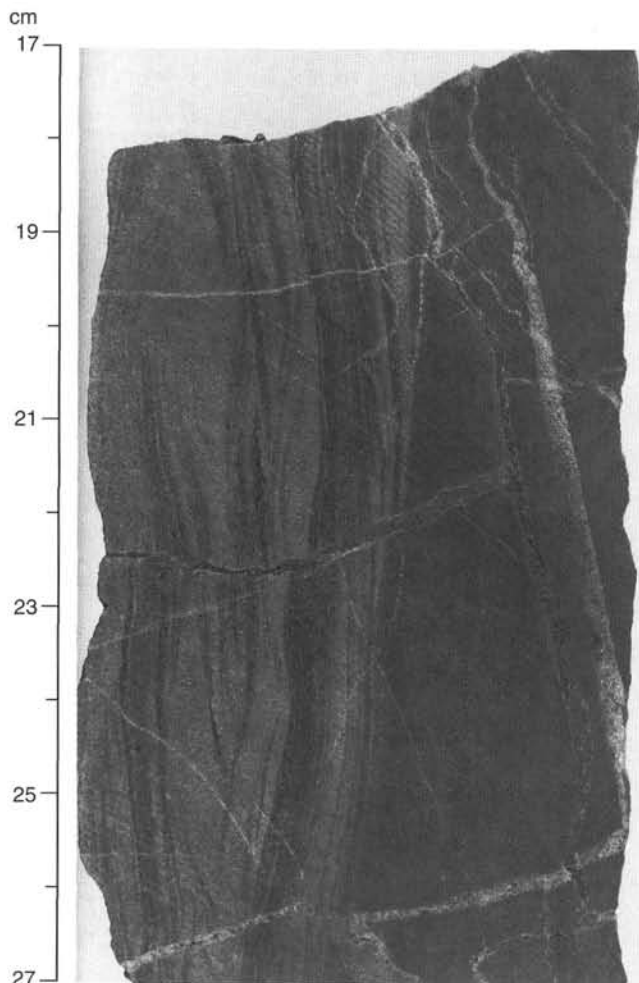


Figure 18. Section 159-962D-17R-CC, 17–27 cm, calcite-cemented sandstone showing small-scale cross-lamination grading to horizontal lamination. Tectonic veins are filled by calcite and fine-grained sediment.

IIA. The very low carbonate contents point to continued deposition below the CCD, but sedimentation rates were much higher (see “Sedimentation Rates” section, this chapter). Periods of high sediment flux were interrupted by periods of sediment starvation when glauconite formed.

At the boundary between lithologic Unit I and II, there is a change from biosiliceous sedimentation in Unit II to a dominantly clayey, pelagic setting in Unit I. The absence of carbonate material in the lower part of Unit I, and few biogenic components in the entire unit (with the exception of several intervals from 0 to 7.5 mbsf), may be a reflection of continued sub-CCD conditions, in which most calcareous components were dissolved. Lithologic Subunit IB consists of interbedded varicolored sediments (greenish green, olive brown to olive, grayish green), which lack sedimentary structures except for bioturbation (facies E1.2 of Pickering et al., 1989). The presence of kaolinite and gibbsite in the olive-colored, goethite-bearing clays and claystones, which are typically produced in tropical-humid laterite soils of the equatorial zones, points to a terrigenous source for the sediments (Chamley, 1989). The present-day suspended load of the Niger River contains large amounts of kaolinite and minor gibbsite (Konta, 1985), which is compatible with similar source area for the sediments drilled at Site 962. Riverine input of kaolinite and gibbsite, however, was probably very low, as indicated by the reduced sedimentation rates for the goethite clay (see “Sedimentation Rates” section, this

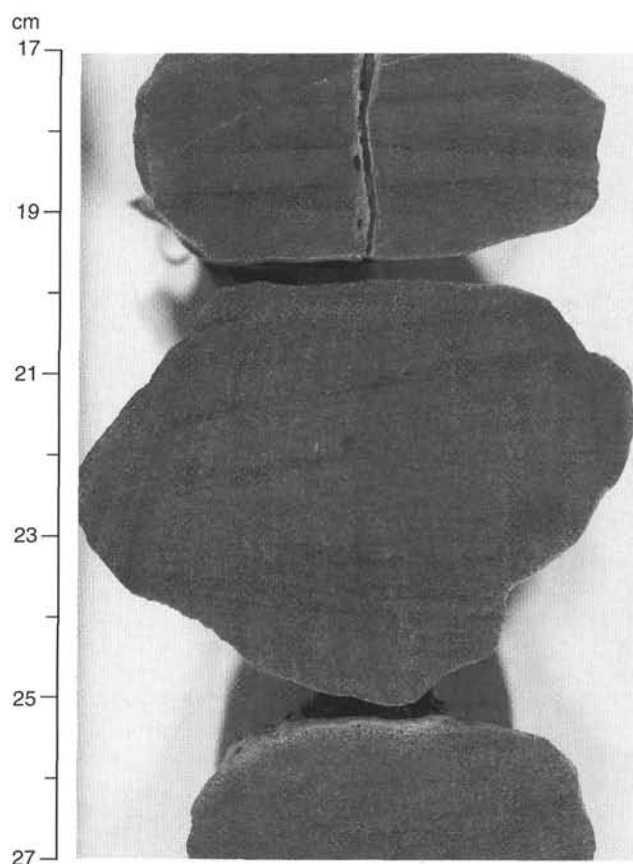


Figure 19. Section 159-962D-6R-1, 17–27 cm, cross-bedded sandstones showing small-scale, upward-curved foresets.

chapter). Eolian erosion and transport of outcropping, deeply weathered clays seem to be an adequate explanation for this mineral assemblage.

The deposition of lithologic Subunit IA commenced with clay, clay with nanofossils with minor interbeds of nanofossil glauconite clay with foraminifers and micrite, and clayey nanofossil ooze with foraminifers. The presence of calcareous microfossils suggests an increase in sedimentation rates and/or a deepening of the CCD during the middle Pliocene to late Pleistocene. These sediments are succeeded by middle to late Pleistocene age pyritic clay and silty clay with plant debris, silty clay with opal and micrite, minor beds of nanofossil glauconite clay with foraminifers and micrite, and clayey nanofossil ooze with foraminifers in the upper part of the subunit. The formation of calcareous micrite can be related to the dissolution of calcitic shells in the sediments.

The Pleistocene sediments of lithologic Subunit IA are distinctive in that they have very high values of total organic carbon, hydrogen index, and T_{max} maturity parameter (see “Organic Geochemistry” section, this chapter). The total organic carbon content and high hydrogen index values suggest that the organic matter was dominantly marine derived, but this source does not correlate well with the abundance of plant debris in some of the sediments. There is a possibility that the organic components in the sediments were derived from both marine and terrestrial sources. Moreover, the high T_{max} value indicates that these sediments are overmature. This highly unusual maturity pattern for such young sediments has been documented only at this site. We suggest that reworking has played a role in increasing the amount of total organic carbon in the sediments, which has consequently affected the maturity parameter. The presence of semiconsolidated siltstone and claystone particles is indicative of redeposi-

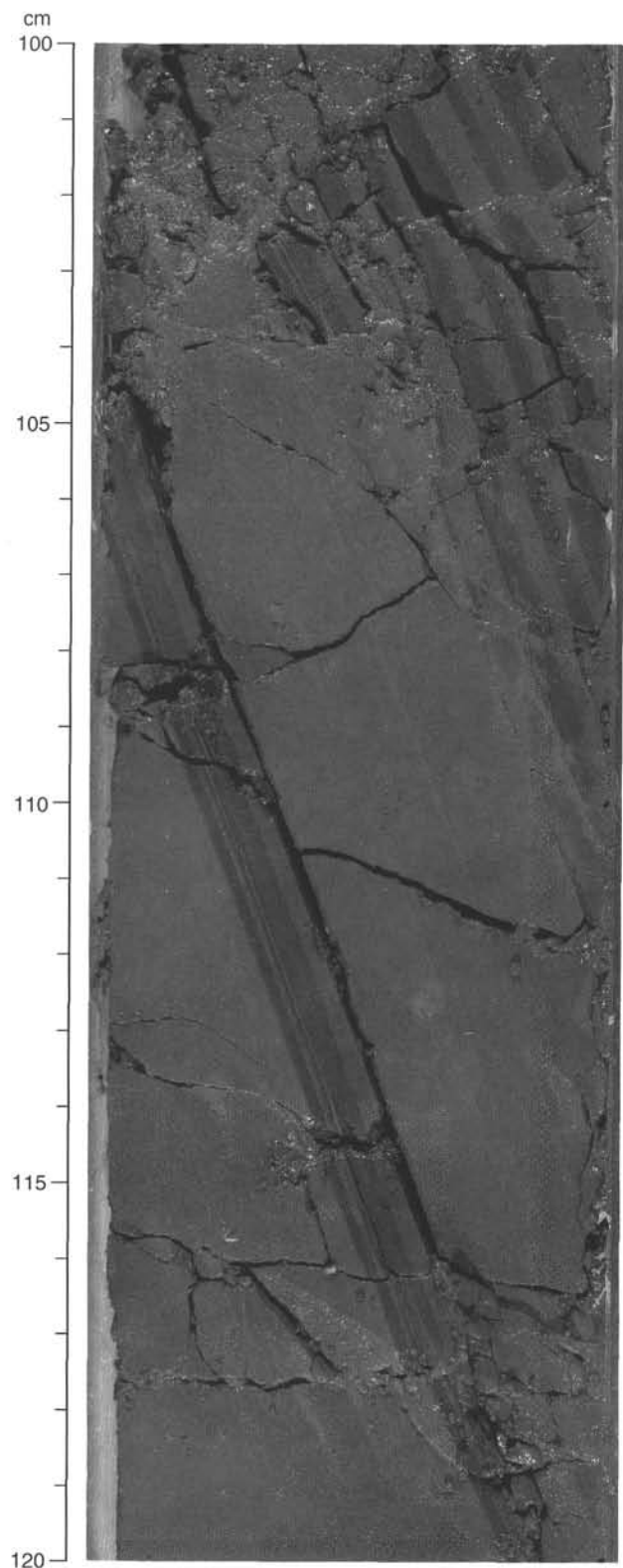


Figure 20. Section 159-962D-12R-4, 100–120 cm. Normally graded to laminated clayey quartz siltstone alternates with thickly laminated micritic limestone with nannofossils.

tion, possibly from the Cretaceous carbonaceous rocks similar to lithologic Unit III. It is noteworthy to mention the existence of the submarine Trouis-sans-Fond Canyon in the Deep Ivorian Basin (Klingebiel et al., 1975), several tens of kilometers to the west of Site 962. Giresse and Barusseau (1989) discussed the accumulation of hemipelagic sediments in the canyon, and also indicated that no deep-sea detrital fan has been associated with the canyon in the last 16,000 yr. It is, however, possible that the Trouis-sans-Fond Canyon acted as a conduit for terrestrial input during the accumulation of lithologic Subunit IA in the Pleistocene.

BIOSTRATIGRAPHY

Introduction

Biostratigraphic control at Site 962 was provided by shipboard analyses of calcareous nannoplankton, planktonic foraminifers, and radiolarians (Fig. 21). Excellent recovery provided by piston coring (APC) and extended core barrel (XCB) drilling of Hole 962B permitted us to study the pelagic cover at a resolution of about one sample per section. Rotary (RCB) coring of Holes 962C and 962D produced incomplete recovery of nearly all cores, but, where it was practical, samples were taken within cores to select the most promising lithologies for preservation of calcareous microfossils.

The Cenozoic sequence at Site 962 is greatly reduced compared to other sites drilled during Leg 159, and preservation of calcareous microfossils is generally poor. Hole 962B contains a disconformity in the middle Miocene that extends into the upper Miocene. Upper Pliocene to Pleistocene deposits are present down to at least Sample 159-962B-2H-CC (17.0 mbsf). Upper Pliocene sediments are present at the top of Core 159-962B-3H (to at least 17.5 mbsf) and a lower Pliocene to upper Miocene section is present from Sample 159-962B-3H-2, 50–52 cm, to at least Sample 159-962B-3H-CC (19.0–26.5 mbsf). Core 159-962B-5H (36.0–45.5 mbsf) is barren of calcareous and siliceous microfossils. Latest early Miocene-aged siliceous microfossils are present in Cores 159-962B-6H and 7H (55.0–64.5 mbsf). Core 195-962B-8H contains a disconformity separating Cenozoic deposits from Albian-Cenomanian(?) cherts and mudstones at about 65.8 mbsf. The presence of a distinctive palygorskite clay-bearing sequence immediately overlying this disconformity suggests that lower Eocene sediments may be present in the top of Core 159-962B-8H (64.5–65.8 mbsf). Similar lithologies have been found only at Sites 961 and 960 within sections assigned to the lower Eocene calcareous nannofossil Zone CP10. Unfortunately, no fossils have been found in the palygorskite-bearing sequence or in the underlying glauconite-bearing sediments in Core 159-962B-8H. Upper Albian to Cenomanian(?) deposits are present within and below Cores 159-962B-8H (71.3 mbsf) and 159-962C-3R (102.4 mbsf). Upper Albian rocks have also been found below Core 159-962D-2R (133.0 mbsf).

Calcareous Nannofossils

The calcareous nannofossil record at Site 962 is restricted to a thin upper Pleistocene and Pliocene section and a thick, Lower Cretaceous sequence.

The Pleistocene–Pliocene section was cored only in Hole 962B. There it is represented by Cores 159-962B-1H through 3H, and the first barren interval extends from Section 159-962B-5H-1 through 9H-CC (45.5–83.5 mbsf). The Cretaceous nannofossils in Hole 962B are limited to Section 159-962B-10H-CC (93.0 mbsf); below this, in Cores 159-962B-11H through 13H (93.0–100.0 mbsf) sediments are barren of calcareous nannofossils. The Cretaceous in Hole 962C is represented by Section 159-962C-3R-CC (102.4 mbsf); Cores 159-962C-1R and 2R (73.0–92.8 mbsf) lack calcareous nannofossils and probably equate with the barren interval above the Cretaceous in Hole 962B. All cores recovered from Hole 962D contain Cretaceous

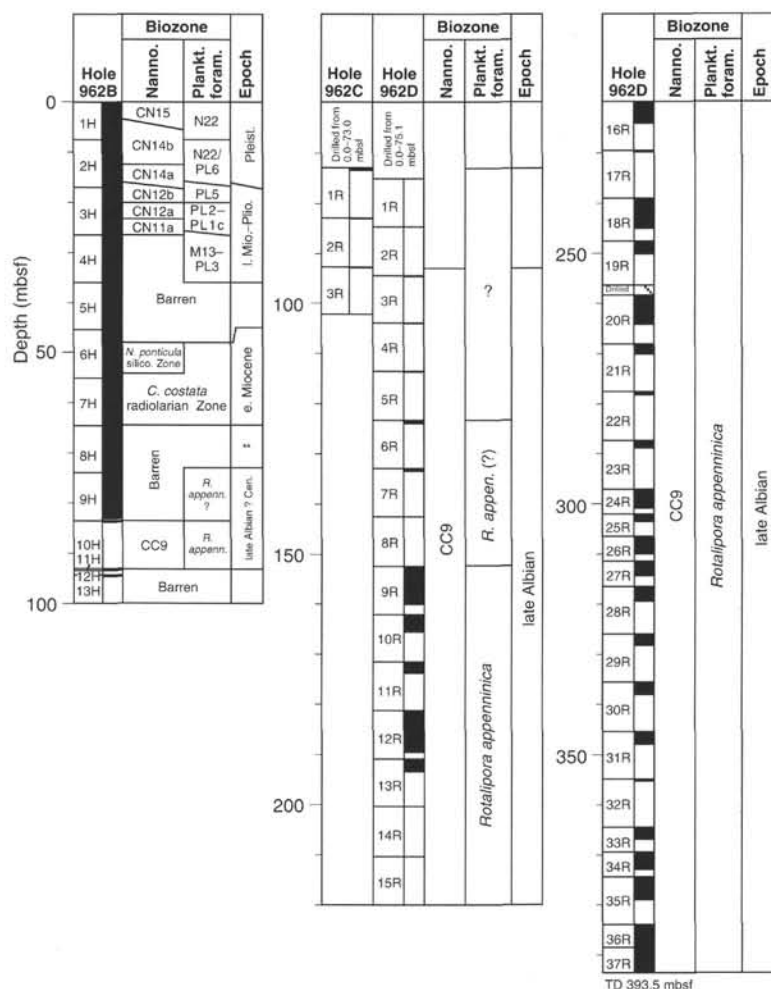


Figure 21. Biostratigraphic age assignments for Holes 962B through Hole 962D. Hole 962A is a single mud-line core of Pleistocene age. No fossils have been found in the first sections in Core 159-962B-8H, but this interval (indicated by the double asterisk) is interpreted to be possible early Eocene age. These sections contain an unusual clay mineral, palygorskite, which has been found in the lower Eocene (calcareous nannofossil Zone CP10) at Sites 960 and 961.

nannofossils, except those that recovered chert fragments without soft sediments.

The assemblage in Sample 159-962B-1H-1, 1–2 cm, contains *Emiliania huxleyi*, indicating late Quaternary Zone CN15. The presence of *Gephyrocapsa parallela* and the absence of both *Pontosphaera indoceanica* and *Helicosphaera inversa* in this sample suggest the latter part of Zone CN15. However, this sample is dominated by *gephyrocapsids*, rather than *E. huxleyi*. This indicates that the record for the last 85,000 years was not recovered in this hole. A similar assemblage is present in Sample 159-962B-1H-1, 50–52 cm. In both samples, the high abundance of *Florisphaera profunda* indicates that the nutricline was relatively deep in the water column during this period.

Sample 159-962B-1H-2, 50–52 cm (2.0 mbsf), contains only rare, strongly etched calcareous nannofossils that indicate significant dissolution during the deposition of this interval. Preservation in this sample is insufficient to determine the age precisely. The next, stratigraphically lower Sample 159-962B-1H-3, 50–52 cm, 3.5 mbsf, contains abundant, moderately preserved nannofossils that include *Emiliania huxleyi*, *Gephyrocapsa parallela*, and *Helicosphaera inversa* without *Pseudoemiliania lacunosa*. This association indicates an age of 0.15–0.24 Ma (Sato and Takayama, 1992). Samples 159-962B-

1H-4, 50–52 cm, and 1H-5, 78–80 cm (5.0 and 6.8 mbsf), are barren of calcareous nannofossils. Sample 159-962B-1H-CC (7.4 mbsf) contains late middle Pleistocene *Gephyrocapsa parallela*, *G. aperta*, and *Helicosphaera inversa* without *E. huxleyi* or *P. lacunosa*. This assemblage indicates Subzone CN14b. This assemblage is dominated by small *gephyrocapsids* with relatively few *Florisphaera profunda*, suggesting that the thermocline was relatively high in the water column during deposition of this sample. Although Samples 159-962B-2H-1, 50–52 cm, and 2H-2, 50–52 cm (8.0 and 9.5 mbsf), are barren, and Sample 159-962B-2H-3, 50–52 cm (11.0 mbsf), contains too few nannofossils to indicate precise age, Sample 159-962B-2H-4, 50–52 cm (12.5 mbsf), also belongs to Subzone CN14b.

The last appearance of *P. lacunosa* occurs in Sample 159-962B-2H-5, 50–52 cm (14.0 mbsf), marking the top of middle Pleistocene Subzone CN14a. *H. inversa* occurs with *P. lacunosa* in Samples 159-962B-2H-5, 50–52 cm, and 2H-6, 50–52 cm. The co-occurrence of these two taxa indicates an age of 0.39–0.48 Ma, according to Sato and Takayama (1992). Sample 159-962B-2H-5, 50–52 cm, is dominated by small (>4 μm) *gephyrocapsids*, whereas Sample 159-962B-2H-6, 50–52 cm, is dominated by *F. profunda*. This suggests a rise in the nutricline or an increase in surface water turbidity during the interval spanned by these samples. Sample 159-962B-2H-5, 50–52 cm,

contains trace amounts of reworked taxa (e.g., *Chiasmolithus solitus*) derived from Eocene sediments. No calcareous sediments of Eocene age were cored at this site, although they are known from shallower sites (e.g., Sites 959 and 960) to the east.

Samples 159-962B-2H-7, 50–52 cm, through 2H-CC (16.6–16.9 mbsf) contain *P. lacunosa*, *G. parallela*, *G. oceanica*, and *Reticulofenestra asanoi* without *Helicosphaera inversa*. This association indicates middle Pleistocene Subzone CN14a. More specifically, the co-occurrence of *G. parallela* and *R. asanoi* indicates that the age of these samples is 0.83–0.89 Ma, based on estimates in Sato and Takayama (1992). Sample 159-962B-2H-7, 50–52 cm, contains abundant *Florisphaera profunda*. This suggests a deep nutricline, following the work of Molfino and McIntyre (1990). Sample 159-962B-2H-CC contains few moderately preserved nannofossils whose sparsity prevents paleoecological interpretation.

Sample 159-962B-3H-1, 50–52 cm, contains *Discoaster surculus*, *D. pentaradiatus*, *D. tritellifer*, *D. brouweri*, *D. asymmetricus*, and *Helicosphaera sellii* without *Discoaster tamalis*. This association indicates early late Pliocene Subzone CN12b. A minimum of 1.7 m.y. is represented by the 0.5-m interval between this and the base of Core 159-962B-2H. Unfortunately, core disturbance at the top of Core 159-962B-3H makes it impossible to precisely place the disconformity that almost certainly is located in this interval. Nannofossils are abundant and well preserved in this sample. Assemblages contain abundant *F. profunda*, indicating limited turbidity and a relatively deep nutricline during this time.

Sections 159-962B-3H-1 through 3H-3 contain numerous concentrations of glauconite, identified as hardgrounds based on lithologic criteria (see “Lithostratigraphy” section, this chapter). Preliminary biostratigraphic determinations indicate rapid changes in age through this interval, indicating significant hiatuses associated with some of these hardgrounds (see “Sedimentation Rates” section, this chapter). Sample 159-962B-3H-2, 50–52 cm (19.0 mbsf), contains *Discoaster tamalis*, *P. lacunosa*, *Sphenolithus abies*, and *S. neoabies* without *Reticulofenestra pseudumbilica*. This indicates the early Pliocene basal part of Subzone CN12a. More precisely, the presence of *Sphenolithus* spp. without *R. pseudumbilica* specifies an age of 3.62–3.77 Ma. Sample 159-962B-3H-3, 50–52 cm, contains *R. pseudumbilica*, *Ceratolithus rugosus*, *Discoaster challengerii*, *D. variabilis*, *D. asymmetricus* (rare), and *Angulolithina arca*, without *Discoaster tamalis* or *Amaurolithus* spp. This association of taxa is diagnostic of early Pliocene Subzone CN11a.

There is a significant lithologic change between Cores 159-962B-3H and 4H, at approximately 26.5 mbsf, separating nannofossil clay (above) from zeolitic clay (below). A few specimens of calcareous nannofossils were observed in Sample 159-962B-4H-1, 50–52 cm (27.0 mbsf). These include taxa that are not age diagnostic (e.g., *Discoaster pentaradiatus*, *Sphenolithus abies*, and *Reticulofenestra minutula*). With this exception, samples from Cores 159-962B-4H through 9H (26.5–64.4 mbsf) are barren of nannofossils. Biostratigraphic control for some of this interval is provided by siliceous microfossils (see below), whereas much of it is barren of all calcareous and siliceous microfossils.

Assemblages from the Cretaceous sequence at this site are not older than the late Albian. The assemblage in Sample 159-962B-10H-CC includes *Axopodorhabdus albianus*, *Biscutum constans*, small *Broinsonia* spp. (probably including *B. beveiri* and/or *B. dentata*), *Broinsonia signata*, *Corollithion signum*, *Eiffellithus collis*, *E. turriseiffelii*, *Eprolithus floralis*, *Gartnerago nanum*, *Gartnerago* sp. cf. *G. obliquum* (very rare), *Gephyrorhabdus coronadventis*, *Lithraphidites alatus*, *Manivitella pemmatoidea*, *Parhabdololithus achylostaurion*, *Prediscosphaera avitus*, *P. columnata*, *Watznaueria barnesae*, and *Zeughrabdodus pseudanthophorus*. A maximum age of late Albian is indicated by the presence of both *A. albianus* and *E. turriseiffelii*. The presence of the small (<5 µm) morphotype of *Prediscosphaera columnata* and the absence of *Hayesites albiensis* and

Corollithion kennedyi indicate a late (but not latest) Albian age for this assemblage. Traces of sediments attached to a piece of chert from Section 159-962C-3R-CC yielded a few, poorly preserved nannofossils, and common nannofossil debris. Identifiable taxa include *Axopodorhabdus albianus*, small *Broinsonia*, *Corollithion signum*, *Cyclagelosphaera margerelii*, *Eiffellithus turriseiffelii*, *Eprolithus floralis*, *Gartnerago nanum*, *Manivitella pemmatoidea*, *Prediscosphaera columnata*, *Stradneria crenulata*, *Stoverius achylosus*, *Watznaueria barnesae*, and *W. ovata*. *Gartnerago obliquum* and *L. alatus* were not found, even though the assemblage came from a level similar to that from which Sample 159-962B-10H-CC was recovered. The assemblage is dominated by common *W. barnesae* and frequent *E. floralis*; other species are rare. It is suggestive of Zone CC9.

Assemblages in Cores 159-962D-2R through 37R (84.7–393.5 mbsf) contain a similar association of key biostratigraphic species, including *Axopodorhabdus albianus* and *Eiffellithus turriseiffelii* (and related species such as *Eiffellithus* sp. 2 of Perch-Nielsen (1985) and *E. collis*). This association in the absence of the key taxa *Corollithion kennedyi*, *Lithraphidites acutus*, or *Microrhabdulus decoratus*, suggests assignment to the late Albian part of Zone CC9. The key species *Prediscosphaera columnata* and the related *P. avitus* are either extremely rare or absent from most of the assemblages from Hole 962D cores. Another species of *Prediscosphaera*, similar to *P. spinosa*, but which could well be *P. sp. cf. P. stoveri* of Perch-Nielsen (1985), is reported from Samples 159-962D-18R-CC (248.8 mbsf) and 31R-CC (354.9 mbsf).

Differences between the late Albian assemblages recovered from Hole 962D cores are minor, but a notable degree of dwarfism was detected in some. The differences include the distribution and abundance of some taxa. For example, small *Broinsonia* spp. are more notable in the younger assemblages (e.g., in Sample 159-962D-2R-CC at 94.4 mbsf) than in the older assemblages where species of *Crucicribrum* occur (e.g., in Sample 159-962D-32-CC at 364.6 mbsf). Similarly, *Parhabdololithus achylostaurion* is more frequent in the assemblages from the upper cores of Hole 962D than in those from the lower cores.

The assemblage from Sample 159-962D-2R-CC, representing the top of the Cretaceous sequence in this hole, contains common *Watznaueria barnesae*, and frequent small *Broinsonia* (probably including *B. beveiri* and *B. dentata*), *E. turriseiffelii*, *Eprolithus floralis*, *Gartnerago* sp. cf. *G. obliquum*, and *Tranolithus exiguus*. Other species identified, including *A. albianus*, *Biscutum constans*, *B. ellipticum*, *Crucicribrum* sp. cf. *C. anglicum*, small *Eiffellithus* sp., *Gartnerago nanum*, *Prediscosphaera columnata*, *Rhagodisus asper*, and *Stradneria crenulata*, are either rare or very rare.

The assemblage from Sample 159-962D-36R-CC, representing the bottom of the Cretaceous sequence in this hole, contains common *Watznaueria barnesae* and frequent *Biscutum constans* and *B. ellipticum*. Other species are rare. These include *A. albianus*, *Discorhabdus ignotus/rotatorius*, *Corollithion signum*, *Cyclagelosphaera margerelii*, *E. turriseiffelii*, small *Eiffellithus* sp., *P. columnata* (small morphotype), and *Tranolithus manifestus*.

Planktonic Foraminifers

Preservation of planktonic foraminifers is generally poor at Site 962, except for a few intervals in the Pliocene (159-962B-3H-1, 53–55 cm; 17.5 mbsf) and late Albian to Cenomanian(?) (159-962B-10X-CC; 93.0 mbsf and 159-962D-8R-CC; 152.4 mbsf) where well-preserved to moderately preserved foraminifers have been found.

Samples taken between the top of Core 159-962B-1H and Sample 159-962B-2H-6, 50–52 cm (0.0–15.5 mbsf), contain a Holocene to late Pliocene assemblage dominated by dissolution-resistant taxa such as *Globorotalia tumida*, *Neoglobobulimina pachyderma* (dextral), and *Neoglobobulimina dutertrei*. *Pulleniatina obliquiloculata* occurs as low as Sample 159-962B-2H-6, 50–52 cm, and suggests

Zone N22 or Zone PL6. *Globorotalia pseudomiocenica* (whose extinction marks the top of Zone PL6) as well as *Globigerinoides fistulosus* and *Globorotalia tosaensis* (whose extinctions mark the subzones of Zone N22) have not been found. Preservation is poor throughout this interval with many samples entirely barren of planktonic and benthic foraminifers or showing nearly complete fragmentation of the planktonic foraminifer assemblage.

Zone PL5 of the late Pliocene is indicated by the presence of moderately preserved *Globorotalia pertenuis* and *Globorotalia miocenica* in the absence of *Dentogloboquadrina altispira* in Sample 195-962B-3H-1, 53–55 cm (17.5 mbsf). This sample contains abundant *G. miocenica*, common *Globigerinoides sacculifer*, *Neogloboquadrina acostaensis*, *Globigerinoides extremus*, and few *Globorotalia inflata*, *G. pertenuis*, and *Globorotalia crassaformis*.

Sample 159-962B-3H-2, 50–52 cm (19.0 mbsf), contains *Sphaeroidinellopsis paendehiscens* and *Sphaeroidinella dehiscentis*, which suggests Zone PL3 or an older zone of the Pliocene. The rest of the assemblage is not age-diagnostic and includes poorly preserved, dissolution-resistant specimens of *Globoquadrina venezuelana*, *Globigerinoides conglobatus*, *N. dutertrei*, and *G. sacculifer*. Sample 159-962B-3H-4, 50–52 cm (22.0 mbsf), has moderately preserved foraminifers, including specimens of *D. altispira*, *G. crassaformis*, *G. tumida*, and *Pulleniatina primalis*. The first appearance of *Globorotalia crassaformis* identifies the base of Subzone PL1c (Berggren, 1977), whereas *P. primalis* does not range younger than 3.4 Ma in the Atlantic and Caribbean (Keigwin, 1982). Therefore, this sample is probably equivalent to lower Pliocene Zone PL2 or Subzone PL1c. Very poorly preserved Pliocene foraminifer assemblages that contain *S. dehiscentis* are present as low as Sample 159-962B-3H-CC (26.5 mbsf).

Cores 159-962B-4H and 5H (26.5–45.5 mbsf) yielded fish teeth, fish bone fragments, and small quantities of angular quartz silt when washed through 45- μ m sieves. Sample 159-962B-4H-CC (36.0 mbsf) contains single specimens of *N. acostaensis* and *S. paendehiscens*, which suggest a late Miocene to early Pliocene age. Below this, Cores 195-962B-6H and 7H (45.5–64.5 mbsf) are barren of planktonic and benthic foraminifers.

Poorly preserved Cretaceous foraminifers are present in and below Sample 159-962B-8H-CC (74.00 mbsf). Sample 159-962B-8H-CC contains mostly fish teeth and fish bone fragments, as well as rare casts of phosphate-filled cephalopods. Planktonic foraminifers are preserved as silica casts without the external shell and appear to represent several species of *Hedbergella* including *H. delrioensis*. The same foraminifer assemblage and preservation are seen in Sample 159-962B-9H-CC (83.50 mbsf). Preservation is markedly better in Sample 159-962B-10H-CC (93.00 mbsf), where foraminifers are well preserved and exhibit no chamber filling. Species in this sample include *H. delrioensis*, *H. costellata*, *H. cf. H. angolae*, *Globigerinelloides caseyi*, *Heterohelix* spp., and *Ticinella*? spp. of probable late Albian age. Samples 159-962B-11H-CC through 13X-CC (93.30–100.00 mbsf) are barren of foraminifers.

Only a few very poorly preserved specimens of *Hedbergella delrioensis* and *Heterohelix* spp. were found in core-catcher samples from Hole 962C (73.0–102.40 mbsf). Likewise, core-catcher samples from the first five cores of Hole 962D (84.70–123.40 mbsf) are barren of both planktonic and benthic foraminifers.

Samples 159-962D-6R-CC through 37R-CC (133.00–393.50 mbsf) contain planktonic foraminifers of late Albian age. Species include *H. delrioensis*, *H. costellata*, *H. angolae*, *H. sp. cf. H. gorbachikae*, *Globigerinelloides bentonensis*, *G. caseyi*, *Ticinella*? spp., rare *H. simplex*, and “*Biglobigerinella*” sp. The presence of *Heterohelix* sp. within and below Sample 159-962D-9R-1, 26–28 cm (152.60–393.5 mbsf), and the presence of *Praeglobotruncana? delrioensis* in Samples 159-962D-9R-1, 26–28 cm, 18R-CC (248.80 mbsf), 19R-CC (256.40 mbsf), 23R-CC (297.00 mbsf), and 31R-CC (354.90 mbsf) suggest that the sequence may be correlated with the “*Rotalipora*” *apenninica* Zone of the late Albian. *Praeglobotruncana*

delrioensis has been identified in Samples 159-962D-25R-CC (306.60 mbsf), 27R-1, 87–90 cm (312.10 mbsf), and 27R-CC (316.30 mbsf). Poorly preserved specimens of *Schackoina* sp. cf. *S. cenomana* found in Samples 159-962D-20R-04, 68–72 cm (261.50 mbsf), and 159-962D-30R-CC (345.30 mbsf) also suggest a latest Albian age. In nearly all cases, preservation in these samples is poor, as the foraminifer chambers are infilled with calcite and many specimens are partly crushed.

Silicoflagellates

Examination of smear slides from Hole 962B indicates that common, well-preserved silicoflagellates occur only in the interval from Sample 159-962B-6H-3, 50–52 cm, through 6H-6, 50–52 cm (49.0–53.5 mbsf). These assemblages include *Naviculopsis ponticula spinosa*, *Naviculopsis ponticula*, *Naviculopsis lata*, *Naviculopsis contraria*, *Bachmannocena elliptica*, *Corbisema triacantha triacantha*, *Distephanus speculum triommata*, and *Distephanus speculum hemisphaericum*. The assemblages in these samples are dominated by *Distephanus hannai*. This association of taxa is definitive for the late early Miocene *N. ponticula* Zone. This age is corroborated by determinations based on radiolarians (see below).

Radiolarians

Radiolarians are present sporadically at Site 962 and are only well preserved in the late Holocene and parts of the lower Miocene sequence. Radiolarians in the Albian sections of Hole 962B and 962D are rare and invariably partly recrystallized to opal-CT or replaced by calcite.

Holocene radiolarians were collected in sediment washed off the top of Cores 159-962A-1H and 159-962B-1H as the cores were being cut into sections. These samples presumably represent the fluff-layer of organic detritus on the seabed. The assemblage is diverse and well preserved. Common to abundant taxa include *Hexacantium enthacanthum*, *Ommatartus tetrathalamus*, *Euchitonina elegans*, *Dityocornyne truncatum*, *Spongaster tetras*, *Anthocrytidium ophirensis*, and *Axoprimum stauraxonium*. Additional taxa present include *Giraffospyris angulata*, *Botryostrobos auritus*, *Stylodictya* spp. (possibly *S. validuspina*), *Strichtopilium bicornis*, *Lamprocyclus maritalis*, *Tetrapyle octacantha*, *Pterocanium trilobium*, and *Eucyrtidium hexagonatum*.

Sediments from below the top of Section 159-962B-1H-1 through Sample 159-962B-6H-1, 50–52 cm, are barren of radiolarians or contain only fragmentary, pyritized specimens. Sample 159-962B-6H-2, 50–52 cm, contains a highly dissolved assemblage consisting largely of *Liriospyris* spp. Preservation is good from Sample 159-962B-6H-3, 50–52 cm, through 6H-CC (49.0 to 55.0 mbsf). Radiolarians of the uppermost lower Miocene *Calocyclus costata* Zone are present throughout this sequence and include *Didymocyrtis prismatica*, *Calocyclus costata*, *Dorcadospyris dentata*, *Cyrtocapsella tetrapera*, *Calocyclus virginis*, *Calocyclus robusta*, and *Tholospyris anthophora*. A dissolved assemblage probably referable to the *C. costata* Zone is also present in Sample 159-962B-7H-CC (64.5 mbsf). Abundant in all samples is a form of *Liriospyris* that has been described by Sanfilippo et al. (1985) as the ancestor to *L. stauropora*.

Sample 159-962B-8H-4, 87–89 cm (71.4 mbsf), includes poorly preserved radiolarians referable either to *Novixitilus* spp. or *Stichomitra* spp. and suggest a Turonian or older age. The sample was taken from a glauconite interval that separates Cenozoic sediments in Sample 159-962B-7H-CC (64.5 mbsf) from upper Albian–Cenomanian? deposits in Sample 159-962B-8H-CC (74.0 mbsf). Sample 159-962B-8H-CC contains rare and poorly preserved specimens referable to *Archaeodictyomitra* spp. (possibly *A. pseudocaris* or *A. simplex*) as well as *Strichomitra communis*? and *Crucella messinae*. The Albian to Turonian species *Archaeospongoprimum cortinaensis* is

present in Sample 159-962B-9H-2, 49–51 cm (76.0 mbsf). Poorly preserved radiolarians also have been observed, but not identified, in Sample 159-962B-9H-5, 52–54 cm (80.5 mbsf).

PALEOMAGNETISM

Magnetic properties at Site 962 were measured from each of the recovered cores in Holes 962B and 962D. The shipboard magnetic investigation of each hole included measurements of bulk susceptibility and natural remanent magnetization (NRM). The APC cores in Hole 962B were oriented using data collected from the Tensor orientation tool. Sections 159-962B-1H-1 through 8H-4 were demagnetized up to 25 mT. No whole-core cryogenic (WCC) demagnetization was applied in the XCB and RCB cores because of the observed drilling disturbance during coring. A systematic magnetic overprint was again observed in the APC cores, including a radial and isothermal magnetization induced by the core barrel that was discussed in the previous site reports (e.g., see "Paleomagnetism" section, "Site 960" chapter, this volume). Based on the correlation of magnetic properties of Hole 962B with those measured at the other sites, we interpret the magnetostratigraphy of Core 159-962B-5H to lie between Biozones PL3 and M9 (3.5 to 12 Ma).

Bulk Susceptibility

Magnetic susceptibility measurements were made on whole cores from Holes 962B and 962D (Fig. 22). Volume susceptibility values are included in Site 962 Appendix A on the enclosed CD-ROM (back pocket). Core recovery with the APC provided a continuous susceptibility record down to ~83 mbsf in this site (Fig. 22A). The RCB cores of Hole 962D provide a discontinuous record below a depth of ~75 mbsf because of the poor recovery (Fig. 22B). Three significant data gaps occurred at the following intervals: 84–152, 194–220, and 224–238 mbsf.

Below the mud line (0 mbsf) in Hole 962B, susceptibility decreases from 20×10^{-5} SI units over 1 m of sediment. Below 1 mbsf, measurements remain constant between values of ~5 and 20×10^{-5} SI units down to 10 mbsf. An apparent cyclicity was observed over this interval. At ~10 mbsf, susceptibility steeply increases from 7 to 21×10^{-5} SI units, over an interval <1 m. Below 11 mbsf, susceptibility gradually decreases from 21 to 4×10^{-5} SI units down to ~15.7 mbsf. Below this depth, susceptibility gradually increases again from low values of $\sim 4 \times 10^{-5}$ SI units to relatively high values of $\sim 32 \times 10^{-5}$ SI units down to ~25 mbsf. Between 26 and 45 mbsf, values remain relatively high (between 20 and 40×10^{-5} SI units, including some measurements $>40 \times 10^{-5}$ SI units). At 45 mbsf, the record sharply decreases from values of ~30 to 10×10^{-5} SI units in <1 m. Below 46 mbsf, susceptibility values remain low (between ~6 and 18×10^{-5} SI units) down to 64 mbsf. Below this depth, measurements decrease to values between 4 and 8×10^{-5} SI units in <0.7 m and remain low with depth ($<20 \times 10^{-5}$ SI units), except in the interval from 68 to 70 mbsf in Hole 962B, and at ~174 mbsf in Hole 962D, where some measurements are $>20 \times 10^{-5}$ SI units. At ~68 mbsf, susceptibility increases abruptly downward over a thickness of about 2 m from ~6 to almost 30×10^{-5} SI units. At ~69.9 mbsf, the trend changes and values sharply decrease to $<12 \times 10^{-5}$ SI units over <0.25 m. Below 70.1 mbsf, the range of values gradually decreases to a low of $\sim 4 \times 10^{-5}$ SI units at ~74.2 mbsf, where the occurrence of maximum values up to 240×10^{-5} SI units was observed over an interval of <0.3 m thickness. Below this zone of high values, susceptibility is generally $<10 \times 10^{-5}$ SI units, with sporadic moderately high values of between 10 and 30×10^{-5} SI units in Core 159-962B-9H. In this core, the rocks were highly disturbed by the recovery process and are composed of drilling breccia with small fragments of chert. We presume that the scatter in the measurements is the result of this disturbance.

Cores recovered in Hole 962D display, on average, low values of susceptibility, $\leq 20 \times 10^{-5}$ SI units below 150 mbsf. At 150–195 mbsf, the susceptibility values are less than 10×10^{-5} SI units. In the interval from 220 to 390 mbsf, values range from 5 to 20×10^{-5} SI units.

Changes of the susceptibility gradient with depth correspond to lithologic and biostratigraphic discontinuities in Hole 962B (Fig. 22A). The boundaries of lithologic Units I and II and the biostratigraphic discontinuities in the upper Cenozoic are also marked by changes in the NRM record. Presumably, shifts in susceptibility values reflect subtle lithologic changes at these biozone boundaries. At a depth of about 15.7 mbsf, the change in susceptibility coincides with the transition between Biozones CN14a and CN12b, which corresponds to a hiatus between the Pleistocene and Pliocene. The change in susceptibility at ~26 mbsf corresponds to the boundary between the silty clay with some biogenic component of lithologic Subunit IA and the claystones with quartz silt, but no biogenic component, of lithologic Subunit IB. Changes in lithology and susceptibility at this depth also coincide with the boundary between the early Pliocene nannofossil clay (Biozone CN11a) and the uppermost zone barren of calcareous microfossils in Hole 962B, corresponding to the transition between Biozones PL2-PL1c and M13-PL3 (late Miocene to Pliocene). The change in susceptibility at ~45 mbsf coincides with the boundary between the clays in lithologic Subunit IB and the radiolarian claystones with diatoms in lithologic Subunit IIA. The interval 26–45 mbsf, which is barren of microfossils, coincides with the highest susceptibility and remanent magnetization seen at this site. The changes in susceptibility and lithology at 45–46 mbsf are close to the upper boundary of the early Miocene radiolarian *C. costata* and silicoflagellate *N. ponticula* biozones (48 mbsf). At a depth of ~64 mbsf, a susceptibility change occurs from radiolarian claystone and porcellanite (lithologic Subunit IIA) to palygorskite claystone with diatoms (lithologic Subunit IIB). Another change in susceptibility occurs at ~70 mbsf, corresponding to a change in lithology from palygorskite claystone with glauconite (lithologic Subunit IIB) to chert and porcellanite (lithologic Subunit IIC).

Remanent Magnetization

Measurements of remanent magnetization were made on core sections and discrete cubes from Holes 962B and 962D. The magnetization of Cores 159-962B-1H through 8H was also measured after carrying out steps of AF demagnetization up to 25 mT. Because of the poor recovery in Hole 962D, NRM measurements were only performed on Cores 159-962B-9R through 37R, which recovered lengths >0.1 m. The magnetization data of the archived core sections are in Site 962 Appendix B on the CD-ROM, and the NRM data are shown in Figure 23. Discrete samples were obtained from each of the core sections in Hole 962B and from intact sections in Hole 962D. Only NRM measurements were performed on the discrete samples because of the lower limit of resolution in the WCC magnetometer. The discrete sample measurements are compiled in Site 962 Appendix C on the CD-ROM.

The magnetization of the sedimentary rocks in cores from Hole 962B is mostly characterized by NRM intensities <100 mA/m. The magnetization of the APC cores shows the characteristic trend of the drilling overprint observed at Sites 959–961 (Fig. 24). Cores 159-962B-1H through 9H possess a vertical remanent component that is steeply inclined upward along the length of the hole, except in Cores 159-962B-1H, 3H, and 6H, in which the component swings from steeply downward at the top to steeply upward at the bottom of each core (Fig. 24A). Furthermore, the horizontal remanent component shows a radial magnetic overprint that was presumably isothermally induced by the drilling, so that the net declination is directed toward 0° (Fig. 24B).

Changes in NRM intensities also reflect zones of lithologic change in Hole 962B. In the upper 0.55 m, the remanent intensity in-

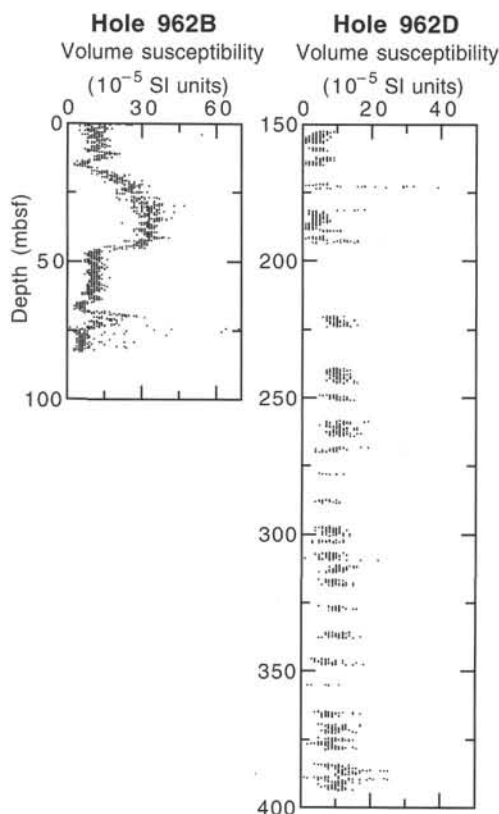


Figure 22. Bulk magnetic susceptibility vs. depth, Holes 962B and 962D.

creases from about 2 to 9 mA/m (Fig. 23A). Remanent intensity drops to values ~ 0.8 mA/m at a depth of 0.85 mbsf. Below this depth, intensity steeply increases to values >10 mA/m at about 1.25 mbsf. Between 1.25 and 4.45 mbsf, intensity remains constant within the range 2–13 mA/m. At about 4.45 mbsf, this change corresponds only to a transition between Biozones CN15 and CN14b (Pleistocene), but not to a visible lithologic change at this depth. Below 4.50 mbsf, values gradually decrease to <0.5 mA/m at about 6.95 mbsf. Below this depth, intensity sharply increases up to 25 mA/m over an interval of about 0.6 m. From 7.5 to 10.7 mbsf, intensity values range from 2 to 50 mA/m. The depth of this change also corresponds to a change in susceptibility, but it does not appear to correspond to any visible lithologic or biostratigraphic boundary. Below 10.7 mbsf, values sharply decrease from ~ 28 to 2 mA/m over an interval of 1.3 m. Below 11.9 mbsf, intensity sharply increases up to values >21 mA/m over a thickness of 0.30 m. Below this point, intensity gradually decreases to values <0.5 mA/m at about 15.3 mbsf, which corresponds to a change in susceptibility and a biostratigraphic hiatus between Biozones CN14a (middle Pleistocene) and CN12b (early late Pliocene). In the interval from 17.1 to 25.5 mbsf, intensity is uniformly constant with higher values (>40 mA/m). Below 25.5 mbsf, there is another sharp increase in intensity (up to 95 mA/m), which represents a change in lithology from clay with a biogenic component in lithologic Subunit IA to clays with quartz silt and no biogenic component in lithologic Subunit IB. Intensity remains relatively high with maximum values >90 mA/m down to ~ 44.5 mbsf, which corresponds to the transition from goethite-bearing claystones in lithologic Subunit IB to radiolarian claystones with diatoms in lithologic Subunit IIA. Below this depth, intensity steeply decreases to values of about 1 mA/m and remains at this value, or lower, down to 63.4 mbsf. At this depth, intensity increases again to values >9 mA/m. This change in intensity corresponds to the transition from porcellanite

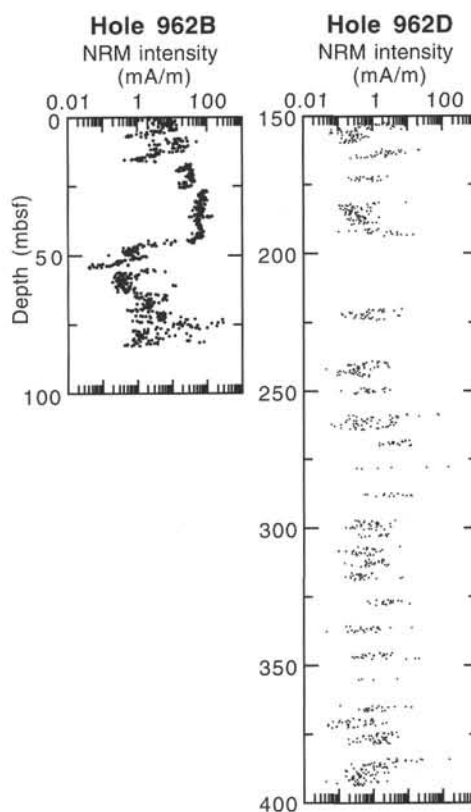


Figure 23. NRM intensity vs. depth, Holes 962B and 962D.

with clay in lithologic Subunit IIA to palygorskite claystone in lithologic Subunit IIB. Below 63.4 mbsf, intensity values remain moderately higher (>1 mA/m) than those for lithologic Unit III and display a wide distribution, with maximum values >120 mA/m.

In summary, the results from Hole 962B indicate that the rocks carry a strong magnetization (values >5 mA/m) in the upper 45 m and are weakly magnetized (<5 mA/m) below 45 mbsf. The interval from 25.5 to 45 mbsf corresponds to layers with very high magnetization, which are predominantly composed of goethite-bearing clay and claystones with quartz silt. At other sites drilled on this leg (Sites 959–961), the upper boundary of the highly magnetized interval is at the boundary of Biozones PL3/PL2 (about 3.5 Ma), and the lower boundary is at, or younger than, Biozone M9 (about 12 Ma). If this high-intensity zone can be chronostratigraphically correlated among the sites, then this suggests that the interval from 25.5 to 45 mbsf in Hole 962B is older than the Biozone PL3/PL2 boundary and younger than Biozone M9.

In Hole 962D, the NRM record indicates that the rocks in the deeper recovered sections (over the interval 150–390 mbsf) are also weakly magnetized with a range of values from 0.1 to 10 mA/m, except over a few intervals where NRM intensity sharply increases to values >10 mA/m. The continuous NRM measurements from Cores 159-962D-9R through 37R do not provide any directional information in the deeper section at this site because of the high degree of fragmentation induced by RCB coring.

Core Orientation

Cores 159-962B-3H through 8H were successfully oriented using the Tensor orientation tool (Table 3). While the tool was in the measuring position in the nonmagnetic drill collar, its magnetometers recorded a field strength of about 30×10^3 nT, similar to the Earth's

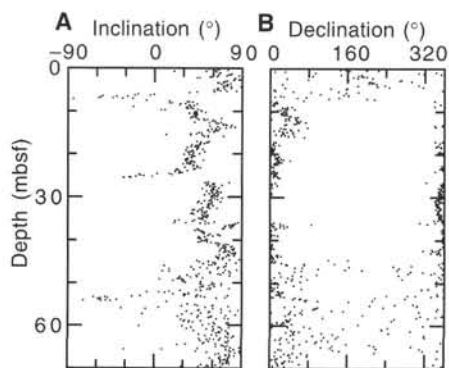


Figure 24. Inclination and declination of NRM directions of Hole 962B.

field at the site. The directions of hole azimuth and inclination, and the position of the core within the barrel typically varied by only a few degrees over the 5-min period before the APC was “fired,” providing a degree of confidence in the reliability of these measurements. Tensor measurements were also made for Core 159-962B-9H, but a data recording problem occurred, and no reliable orientations could be obtained for this core.

Magnetostratigraphy

Within the interval of high NRM intensities in Hole 962B (16–44 mbsf) one core (159-962B-5H) records a magnetic signal from which a plausible magnetostratigraphy can be extracted. For this core, the Tensor tool indicates an angle of 6° between true north and 000° in the core coordinates (Table 3). The NRM directions are steep, downward, and toward the cut face, typical of drilling-induced components seen throughout the leg (Fig. 25A). Alternating field demagnetization to 25 mT partially removed this drilling-induced component, revealing two characteristic sets of directions (Fig. 25B). In the first case, demagnetization isolated a north-directed, subhorizontal component (Fig. 25B, C). In the second case, demagnetization partially removed the drilling-induced component, leaving a south-directed, often steep component (Fig. 25B, D). Inspection of the demagnetization trajectories in stereographic projection suggests that progressive demagnetization moves these directions toward a south-directed, shallow-dipping component. The pattern of the reversal stratigraphy can be seen in the declination at 25 mT cleaning (Fig. 25E). The biostratigraphy at Site 962B only constrains the age of Core 159-962B-5H as being between planktonic foraminifer Biozones PL3-M13 and the uppermost lower Miocene *C. costata* radiolarian zone. However, the distinctive magnetic high zone in Hole 962B may be correlated with a similar pattern observed at Sites 959 and 960, which have better biostratigraphic control. This suggests that Core 159-962B-5H is between planktonic foraminifer Biozones PL3 and M9. More than 30 reversals are present within this interval (Cande and Kent, 1992), so it clearly is not possible to uniquely tie the five reversals observed in this core to the magnetostratigraphic record. However, we consider the best fit to be Chron 3A (Fig. 25E), placing Core 159-962B-5H in the upper Miocene (Messinian–late Tortonian).

SEDIMENTATION RATES

Sediment accumulation rates were calculated from biostratigraphic data only for the Neogene from Hole 962B (Fig. 26). Strata older than the late early Miocene at this site were disrupted by slumping or severe drilling disturbance (Section 159-962B-8H-3 through Core

Table 3. Tensor tool orientations for cores from Site 962.

Leg, hole, core number	MTF (°)
159-962B-	
3H	255
4H	56
5H	354
6H	351
7H	353
8H	354

Note: MTF is the angle between true north and the line marked on the center of the working half section.

159-962B-9H) or by structural deformation (Core 159-962B-10H and below). As a result, sediment accumulation estimates for these strata would be meaningless.

Samples were examined at approximately 1.5 m intervals throughout the upper nine cores from Hole 962B. However, several samples in the Neogene are barren of calcareous microfossils. In addition, planktonic foraminifer preservation is poor in many samples. The combination of poor preservation and barren intervals limits the biostratigraphic resolution and, in some cases, increases the depth errors for some biostratigraphic datums. The datums used for sediment accumulation calculations are given in Table 4.

Sedimentation accumulation rates for the upper lower Miocene strata are only partially constrained by siliceous microfossil biostratigraphy (see “Biostratigraphy” section, this chapter). Silicoflagellates and radiolarians provide minimum and maximum ages for Samples 159-962B-6H-3, 50–52 cm (49.0 mbsf), and 7H-CC (64.4 mbsf), respectively. Assuming that these two biostratigraphic datums are accurately placed in the sequence yields a sediment accumulation rate of 38–42 m/m.y. This sediment accumulation rate is quite reasonable for a biogenic siliceous claystone. However, the sediment above this interval of siliceous microfossil preservation is barren of fossils through the top of lithologic Subunit IB (at Sample 159-962B-4H-1, 0–1 cm). Thus, it is probable that the top of *Naviculopsis* is a preservational artifact. In addition, the base of *Calocycletta costata*, as identified in this sequence, coincides with the boundary of lithologic Units I and II, suggesting that its range has been truncated at a disconformity. As a result, this rate of sediment accumulation must be considered as a minimum estimate.

The entire middle and late Miocene is represented at this site by zeolitic pelagic clay that is barren of calcareous or siliceous microfossils. Assuming continuous and constant sediment accumulation throughout the middle and late Miocene yields a reasonable estimate of 2 m/m.y. for this interval.

Sediment accumulation during the Pliocene and Pleistocene was sporadic and punctuated by numerous hiatuses. In some cases, these disconformities are marked by glauconitic hardgrounds (see “Lithostratigraphy” section, this chapter), whereas others are masked by breaks in the core and are only detectable by biostratigraphic means. The earlier part of the early Pliocene (approximately 5.4–4.4 Ma) may have been a continuation of the zeolitic pelagic clay deposition that characterized the middle and late Miocene, although the absence of calcareous and siliceous microfossils in this clay make it impossible to determine.

The period from approximately 4.0 to 4.4 Ma was characterized by an episode of nannofossil ooze sedimentation with accumulation rates of 16–20 m/m.y. The presence of several glauconitic hardgrounds in the sediments of this age suggests that accumulation was sporadic and that sediment flux was probably higher than reflected in the sediment accumulation rates. This was followed by an interval (from approximately 0.5 to 4 Ma) of very slow, sporadic sediment accumulation of less than 3 m/m.y. Numerous glauconitic hardgrounds

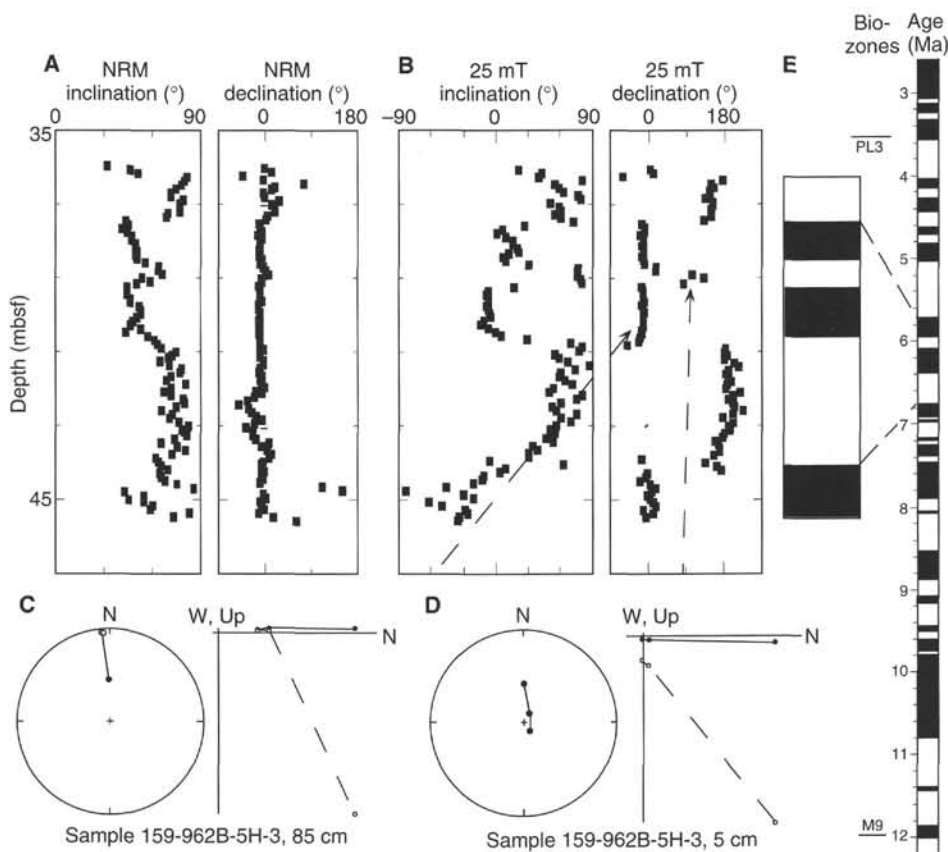


Figure 25. Preliminary magnetostratigraphic interpretation of Core 159-962B-5H. **A.** Declination and inclination of NRM directions vs. depth. **B.** Declination and inclination of 25-mT demagnetization directions vs. depth. **C.** Stereonet and Zijderveld diagrams at 39.85 mbsf. **D.** Stereonet and Zijderveld diagrams at 39.05 mbsf. **E.** Correlation of magnetic reversals with Cande and Kent (1992) geomagnetic time scale in the Miocene.

in the sediments of this age suggest that bottom currents were active during at least part of this interval. It is likely that much of this time period is represented only by disconformity surfaces at this site, although more detailed sampling will be necessary to establish the precise timing of these events.

Sediment accumulation rates for the last 0.5 m.y. of the Quaternary are high (37–49 m/m.y.), despite the fact that part of this sequence was deposited below the local carbonate compensation depth. Sedimentological analysis indicates the presence of a large amount of clay and silt in this sediment, as well as lower content of terrestrial organic debris (see “Lithostratigraphy” section, this chapter). Analyses of the organic carbon in the Pleistocene sediments indicate a high degree of maturity consistent only with the reworking of older sediments (see “Organic Chemistry” section, this chapter). This influx of clastic material is responsible, no doubt, for the high sediment accumulation rates in this part of the sequence.

STRUCTURAL GEOLOGY

In Hole 962B, cores were recovered by the APC and bedding measurements were reoriented to geographic coordinates (i.e., relative to true north) through use of Tensor orientation tool data. Because the RCB was used in Hole 962D, the Tensor tool could not be used for reorientation. For Hole 962D, measurements will be reoriented relative to geographic north when Formation MicroScanner

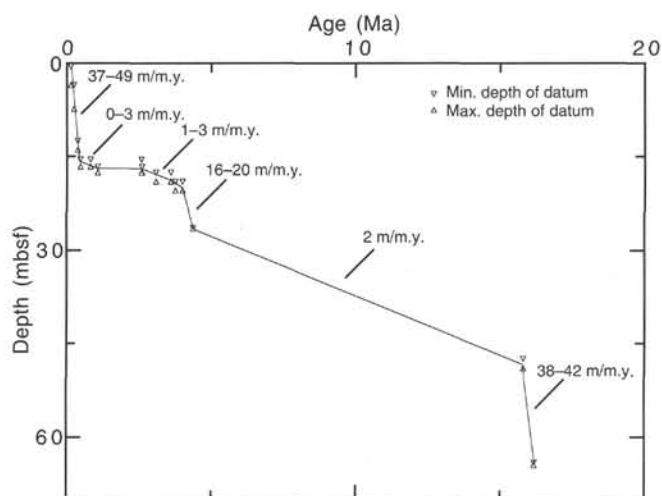


Figure 26. Graphic representation of sediment accumulation rates for the Neogene of Site 962.

Table 4. Biostratigraphic datums, ages, and depths used to calculate sediment accumulation rates for Hole 962B.

Datum	Age (m.y.)	Maximum depth (mbsf)	Minimum depth (mbsf)
t <i>H. inversa</i>	0.15	0.5	3.5
b <i>E. huxleyi</i>	0.26	3.5	7.4
t <i>P. lacunosa</i>	0.39	12.5	14.0
b <i>H. inversa</i>	0.48	15.5	16.6
t <i>R. asanoi</i>	0.83	15.5	16.6
t <i>G. oceanica</i>	1.08	16.6	17.5
t <i>G. pertenuis</i>	2.60	15.5	17.5
t <i>D. surculus</i>	2.61	16.6	17.5
t <i>Sphaeroidinellopsis</i>	3.10	17.5	19.0
t <i>Sphenolithus</i>	3.62	17.5	19.0
t <i>R. pseudoumbilica</i>	3.77	19.0	20.5
b <i>D. tamalis</i>	4.01	19.0	20.5
t <i>Amaurolithus</i>	4.39	26.4	26.5
t <i>Naviculopsis</i>	15.80	47.5	49.0
b <i>C. costata</i>	16.20	55.4	64.2

Note: t = top of occurrence, and b = bottom of occurrence.

(FMS) data (recorded between 191 and 286 mbsf) and paleomagnetic data become available. The RCB drilling of Holes 962B and 962D caused strong core disturbance, resulting in rotation of individual blocks about a vertical axis within the core liner.

Structures were recorded in Holes 962B and 962D only, as the recovery in Holes 962A and 962C was restricted to 3.71 and 0.51 m of soft sediments, respectively. In Hole 962B, apart from the dip variation, structures are represented by normal faults with rare, small reverse faults. Hole 962D provided relatively few structures in the upper part of the hole because of the high degree of drilling disturbance. From Section 159-962D-12R-4 (at 186 mbsf) downward, the core condition and hence the quality of measurements improved. A variety of structures was observed. Extensional features are illustrated by fractures filled by calcite with a variable normal offset. Evidence for compressional deformation includes reverse faulting and microfolding. Calcite veining is common and occurs as infilling of fractures.

Bedding

In Hole 962B, bedding dip values vary between 1° and 18° (Fig. 27A). Deformation of the soft sediments during the coring process produced this variation, and it is clear from observing the cores that bedding is predominantly flat to very shallowly dipping. A rose diagram of bedding dip directions is shown in Figure 28. A wide scatter in all directions is indicated.

The bedding dips in Hole 962D display a wide scatter of values that do not show any clear or systematic trends (Fig. 27B). Bedding is locally highly disturbed (e.g., Cores 159-962D-6R and 7R) by faulting and some bioturbation. Locally the sandstone is slumped on a small scale (interval 159-962D-7R-1, 25–33 cm; 133 mbsf) and may be a cause of some of the variation in dip. High dips (up to 85°) are found in Section 159-962D-12R-4 at 186 mbsf, where an asymmetric microfold may be interpreted as resulting from dragging in the reverse limb of a large-scale fold. In the next core (interval 159-962D-13R-2, 35–40 cm; 192 mbsf), dips vary from 30° to vertical. This abrupt change in dip may be interpreted as a result of faulting. The data gap between 200 and 250 mbsf is due to highly fractured and disrupted cores (Cores 159-962D-14R through 20R; 200–229 mbsf). An overall increase in dip value can be observed between approximately 150 and 200 mbsf. Thereafter, dip values are widely scattered. Some of this scatter undoubtedly reflects core disruption. However, a significant amount of the scatter is due to real variations in the dip and may reflect folding and/or tilting related to faults. High dip values (up to 81°) in Cores 159-962D-23R through 25R (288–303 mbsf) were measured in laminated and cross-bedded silty lime-

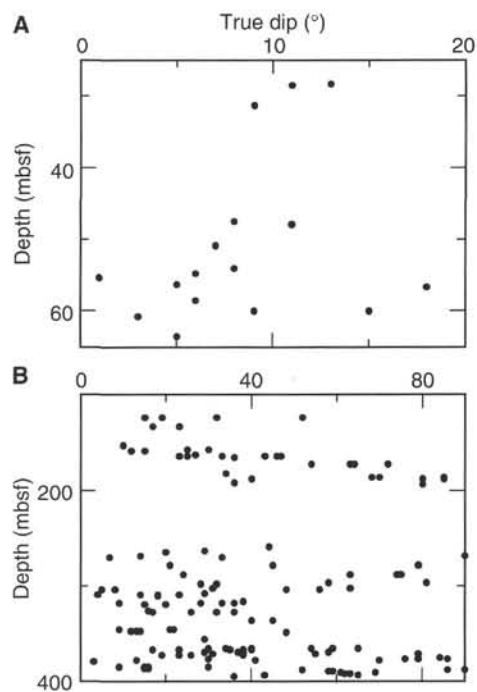


Figure 27. Variation of bedding dip with depth in (A) Hole 962B and (B) Hole 962D. Dip values are calculated from two apparent dips.

stones. Many of the measurements were made in relatively large, undisturbed pieces of core and thus probably reflect true dip values. The highly varied dip directions of these pieces resulted from rotation about a vertical axis within the core liner. Bedding dip values within the interval 307–355 mbsf (Cores 159-962D-26R through 32R) are slightly lower (in the range 4°–48°). The dip values in Cores 159-962D-33R through 37R are highly variable (3°–90°) and may reflect meso- to macroscale folding or fault-related tilting. A slight curvature in some of the beds also suggests folding (e.g., interval 159-962D-35R-2, 6–34 cm; 374 mbsf). Another cause of dip variation is cross- and undulose bedding (e.g., interval 159-962D-6R-1, 20–24 cm; 123 mbsf).

Faults and Shears

Fracturing occurs as several different types, including sharp fault planes, either open or filled by vein material, and more diffuse shear zones. A third type of rock disruption is represented by breccia, where the deformation associated with faulting and veining affects a wide area of the rock.

In Hole 962B, faults were observed in Cores 159-962B-4H, 5H, and 8H. Faults in the nanofossil clay and claystone of Cores 159-962B-4H and 5H are formed by moderately to steeply dipping (43°–77°) sharp planes. The faults appear to be predominantly normal although bedding is difficult to discern in the sediments of Cores 159-962B-4H and 5H. However, a clear example of normal faulting is present in Section 159-962B-5H-6, where a series of normal microfaults with offsets of 0.5 cm cuts a glauconitic layer. Similarly, in Section 159-962B-8H-1, two series of normal faults were observed. Both normal and reverse faults were observed in Section 159-962B-8H-2. Several of the faults display irregular trace.

In Hole 962D, faulting is well represented and tends to occur as sets rather than isolated fault planes. In Section 159-962D-6R-CC, the well-laminated brown calcareous sandstone is highly fractured by a set of minor normal faults filled with calcite (Fig. 29). Two sets of

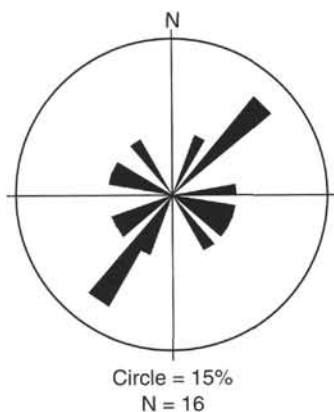


Figure 28. Rose diagram of bedding dip directions in Hole 962B, showing a wide scatter of values. The apparent predominantly northeast-southwest direction is an artifact of the rose diagram intervals (10°) and does not reflect a significant maximum.

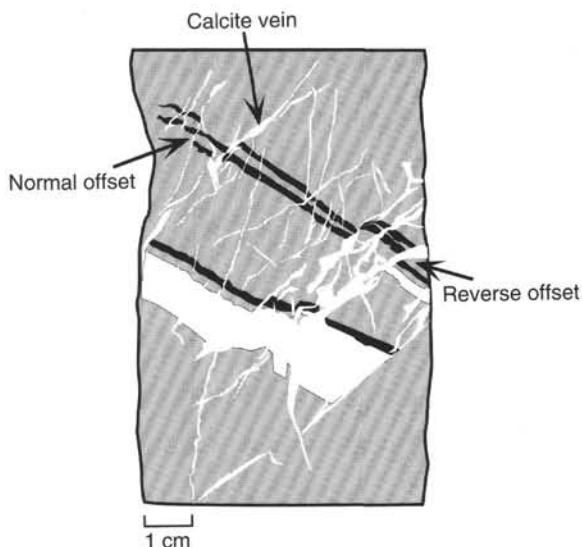


Figure 29. Sketch of a set of conjugate normal faults formed prior to tilting (Section 159-962D-6R-CC, archive-half). Note the occurrence of a reverse fault and calcite infills along the fault planes.

conjugate planes are present, and their orientation relative to the bedding suggests an origin prior to the tilting of bedding. A reverse fault associated with the normal faults is marked by more intense veining.

Other occurrences of normal microfaults were observed in Section 159-962D-7R-1, at 14–20 and 23–25 cm. The deformation seen in interval 159-962D-7R-1, 25–32 cm, may have a syndimentary origin, as no well-marked fault plane could be observed. Realignment of quartz grains, rather than discrete planes, defines the offsets. Section 159-962D-7R-CC is highly fractured, with pieces of gray calcareous sandstone detached and scattered in a disturbed matrix.

Fractures related to horizontal compression are also common and generally consist of reverse faults occurring as sets (intervals 159-962D-12R-4, 35–36 cm, and 159-962D-12R-5, 88–90 cm) or associated with small asymmetric folds. The top of Hole 962D has a poor recovery, but in Section 159-962D-2R-1 deformation was observed in well-layered siliceous rock. This deformation is related mainly to bedding-parallel compression and resulted in an open fold, with two reverse faults forming a pop-up structure in the core (inner hinge)

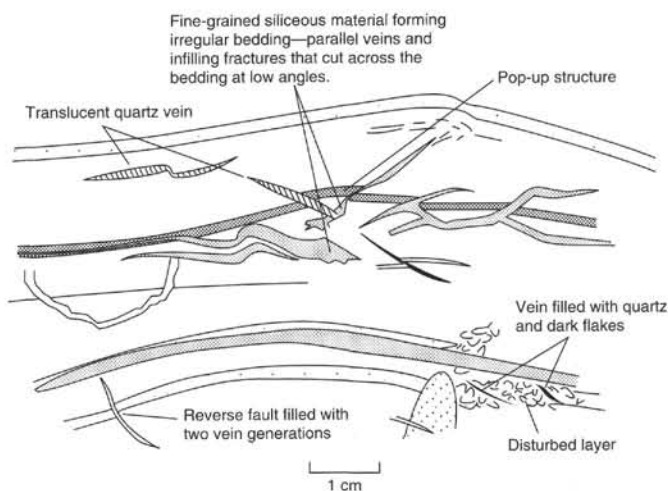


Figure 30. Bedding-parallel compressional structures. A gentle asymmetric fold with reverse faults in the core bounds a pop-up structure. Veining occurs in two habits: an earlier generation comprises quartz as a fracture infill or tension gashes, and the second is formed by a fine-grained siliceous material parallel to bedding or in fractures (interval 159-962D-2R-1, 1–4 cm, working-half).

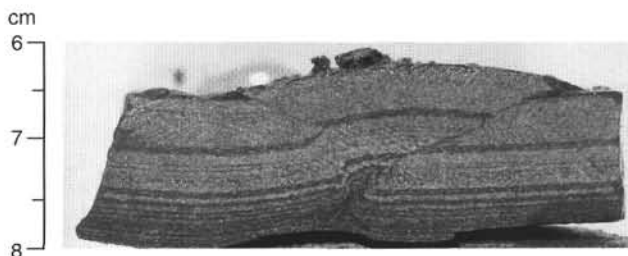


Figure 31. Asymmetric microfolding, resulting in the formation of a pop-up structure, with the right-hand reverse fault more strongly developed than that on the left. The faults are marked by thin seams of dark fine-grained material (interval 159-962D-27R-CC, 6–8 cm).

(Fig. 30). A similar geometry was observed in a more clastic lithology where a pop-up structure has produced buckling in the underlying clayey laminae, resulting in the disappearance of the fold within this less coherent lithology (Fig. 31).

Shallowly dipping shear zones were recorded in Section 159-962D-9R-1, and many others can be inferred as slickensided planes bounding lens-shaped bodies were identified in the disturbed parts of cores.

Evidence for strike-slip faulting is sparse at Site 962. However, a set of steeply dipping microfaults displaying both normal and reverse senses of motion in interval 159-962D-24R-3, 53–57 cm, may be evidence for strike-slip motion. Oblique slickensides on a vertical fault in interval 159-962D-35R-2, 132–140 cm, pitch at an angle of 30° to the strike of the fault plane and may be further evidence for a strike-slip component. Small pop-up structures and the close association of extensional and compressional features in Hole 962D may also reflect larger scale flower structures related to strike-slip motion.

Folds

Folding is a common structural feature in Hole 962D from 85 to 391 mbs, where it is variously expressed (size, morphology, associ-

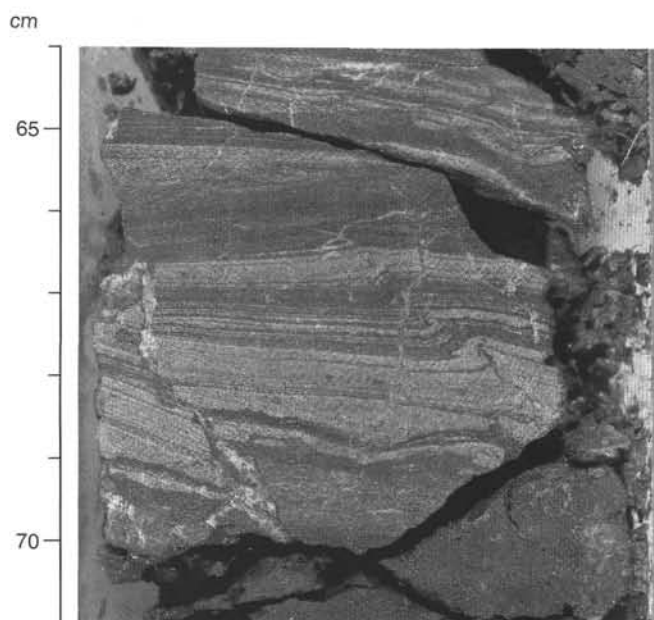


Figure 32. Asymmetric microfold with incipient reverse fault along the short limb. On the left-hand side, a fracture with calcite infilling displays a reverse offset (interval 159-962D-26R-1, 64–71 cm).

ated with other structures). A tectonic origin is clear for most of the folds, although their morphology indicates deformation within the sediments at different stages of lithification. For example, the fold in interval 159-962D-19R-1, 146–148 cm, has a distinctly soft-sediment appearance, whereas the fold in Section 159-962D-34R-1 is clearly a tectonic kink fold.

Several brittle microfolds were observed in Section 159-962D-26R-1, including one with a thin fracture along its shallowly dipping axis (Fig. 32). The fracture is infilled with fine-grained black material and both the fold and fracture are crosscut by a vertical calcite vein. Slight kinking of laminations was observed in Section 159-962D-26R-2 and an incipient kink fold was recorded in Section 159-962-33R-CC at 7 cm (366 mbsf).

The well-layered cherts in Sections 159-962D-2R-1 and 5R-CC display folding. An open fold with associated reverse faults (see above) shows a slight asymmetry (Section 159-962D-2R-1). Section 159-962D-5R-CC shows a tight fold with a rounded hinge and a rapid variation of thickness across the fold, with one limb thinned. Evidence of relative motion along the bedding planes is seen on the thinned limb as a small fault-drag effect. A quartz vein cuts across the fold and shows clear evidence of movement.

The variable dips recorded in Hole 962D may reflect folding on a large scale. For instance, an asymmetric fold (10 cm in length) in Section 159-962D-12R-4 at 93–103 cm may be parasitic on a much larger fold. The steeply dipping laminae in the coherent fragments of Cores 159-962D-34R and 35R display slight curvature and changes in dip direction, suggesting large-scale open folding. However, considerable drilling disturbance throughout Hole 962D makes this difficult to confirm.

Veins

Calcite veins are ubiquitous throughout Hole 962D. They occur as dense networks, and are common along minor faults that show 1 mm to 0.5 cm of predominantly normal offset. Calcite veining in various degrees of intensity was observed in every core from Cores 159-962D-6R to 159-962D-37R (123.4 to 393.5 mbsf). An entire spec-

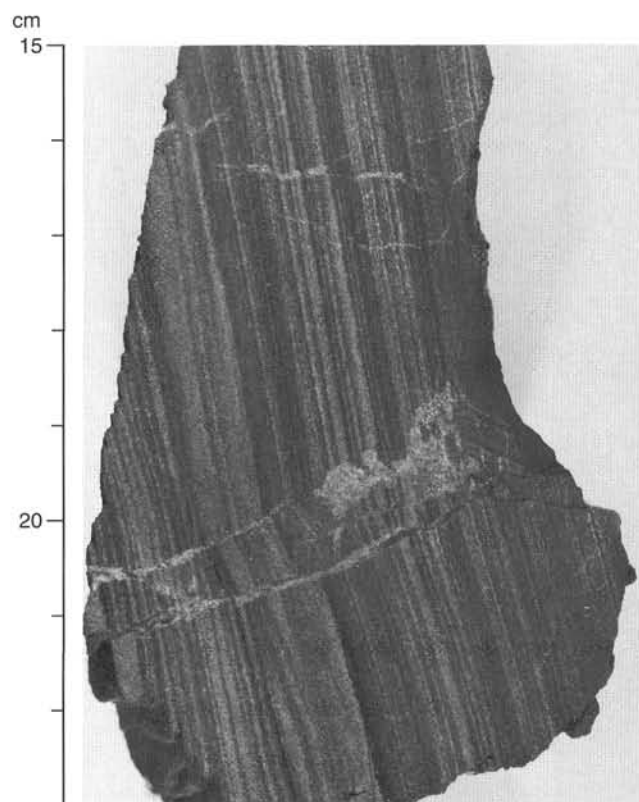


Figure 33. A series of fractures and faults with offsets of 1 mm or less that have been mineralized by calcite (interval 159-962D-23R-CC, 15–23 cm).

trum, from single mineralized fractures to vein networks and ultimately, brecciation, can be observed in Hole 962D. A beautiful example of calcite veining occurs in Section 159-962D-6R-CC, where conjugate sets of normal microfaults are infilled with calcite (Fig. 29). Section 159-962D-10R-3 also displays intense calcite veining in laminated brown sandstone. The veins offset the laminae by 1–2 mm. The veins contain translucent sparry calcite and a pale brown micritic material, reflecting two generations of vein infill. A good example of different vein generations and infills is also present in Section 159-962D-17R-CC (Fig. 18; “Lithostratigraphy” section, this chapter). Here, white calcite veins are cut by a second generation of veins that display pale calcite margins and darker centers. The central parts of these younger veins are brown micrite that contains fine clastic material. Two types of vein were also observed infilling fractures in chert in Section 159-962D-2R-1 (Fig. 30). The first generation is formed by quartz infilling reverse microfaults. Black flakes are associated with the vein quartz. A later generation, represented by a fine-grained siliceous material, occurs as infilling along bedding and fracture planes.

Pyrite is associated with calcite veins in a few cases (e.g., Section 159-962D-12R-5). A common feature of the calcite veins in Hole 962D is their association with brittle fractures, faults, and kinks. For example, in Section 159-962D-23R-CC, a series of faults with offsets of 1 mm or less have been mineralized by calcite (Fig. 33). Similar features were found in Sections 159-962D-25R-CC and 31R-1 and throughout the rest of Hole 962D. The laminations on either side of these minor faults have different angles, as well as being offset. En échelon calcite veins were observed in a few cases (e.g., Section 159-962D-24R-3). Calcite is commonly associated with brecciation, with a good example seen in Section 159-962D-36R-2 (Fig. 34). A zone 1

cm wide comprises angular fragments of laminated calcareous siltstone (the surrounding lithology) in a calcite matrix. This probably represents a mineralized fault zone. Sections 159-962D-37R-2 and 37R-3 also contain zones of intense veining and brecciation. The example in Section 159-962D-37R-3 represents an intermediate stage between fracturing and brecciation. Calcite also occurs in wispy veinlets less than 0.5 mm wide. These are ubiquitous and generally cut the bedding at high angles. Vein generations are difficult to determine at this stage and will become clearer after the detailed study of samples. Conjugate sets of veins are common and typically form crosses (approximately 60° apart) at high angles to the bedding. The high variability in bedding dips and the relatively constant relationship of the veins to the bedding imply that veining predated tilting.

Section 159-962D-6R-1 is formed by calcareous sandstone displaying two generations of calcite veining: the central part of the vein is formed by white calcite crystals oblique to the vein margins, whereas the calcite along the margins is formed by fine-grained gray calcite.

Two types of siliceous veins were observed in chert in Section 159-962D-5R-CC. One is a fine, gray-white siliceous material bearing thin slickensides; a second opaque white generation of siliceous material bears slickensides at a low angle (about 3°–5°) to the first one.

Soft-sediment Deformation

Several structures related to soft-sediment deformation were recorded at Site 962. In Section 159-962D-11R-1, ptygmatic-style, soft-sediment folding was observed. Section 159-962D-11R-CC displays a series of listric normal faults a few centimeters in length that appear to be relatively soft sedimentary in origin. A soft-sediment microfold (1 cm in diameter) was also observed in Section 159-962D-19R-1. The folded laminae display variable thicknesses and have become separated and bulbous in appearance in the fold hinge. A larger scale slump fold (approximately 10 cm across) was observed in Section 159-962D-29R-CC. Convolute bedding occurs within a 2-cm-thick bed in Section 159-962D-37R-3. Synsedimentary reverse microfaults are found in a laminated and cross-laminated succession in Section 159-962D-23R-1. The two faults form a small pop-up structure less than 1 cm in diameter. The rounded appearance of the displaced segment and the undisrupted nature of the surrounding laminae suggest a soft sedimentary origin.

ORGANIC GEOCHEMISTRY

At Site 962 real-time monitoring of volatile hydrocarbons, determination of inorganic and total carbon, total nitrogen and Rock-Eval measurements were performed ("Explanatory Notes" chapter, this volume). Results on volatile hydrocarbons are discussed in the "Source Rock Geochemistry" section (this chapter).

Carbonate and Organic Carbon Records

At Site 962 inorganic and organic carbon and total nitrogen contents were measured on 68 samples. Average sampling frequency for organic geochemical studies was three samples per core in Hole 962B and one to two samples per core in Hole 962D, due to lower core recovery. Table 5 and Figure 35 summarize and present the analytical results.

Minimum carbonate carbon contents (below 0.5 wt%) in clays and oozes in the upper 15 mbsf reflect persistent carbonate dissolution below the calcium carbonate compensation depth (CCD) at Site 962 throughout the Pleistocene (Fig. 35). The corresponding organic carbon record, however, shows consistently high contents ranging from 1.2 to 1.5 wt%. Such elevated values were unexpected, consid-

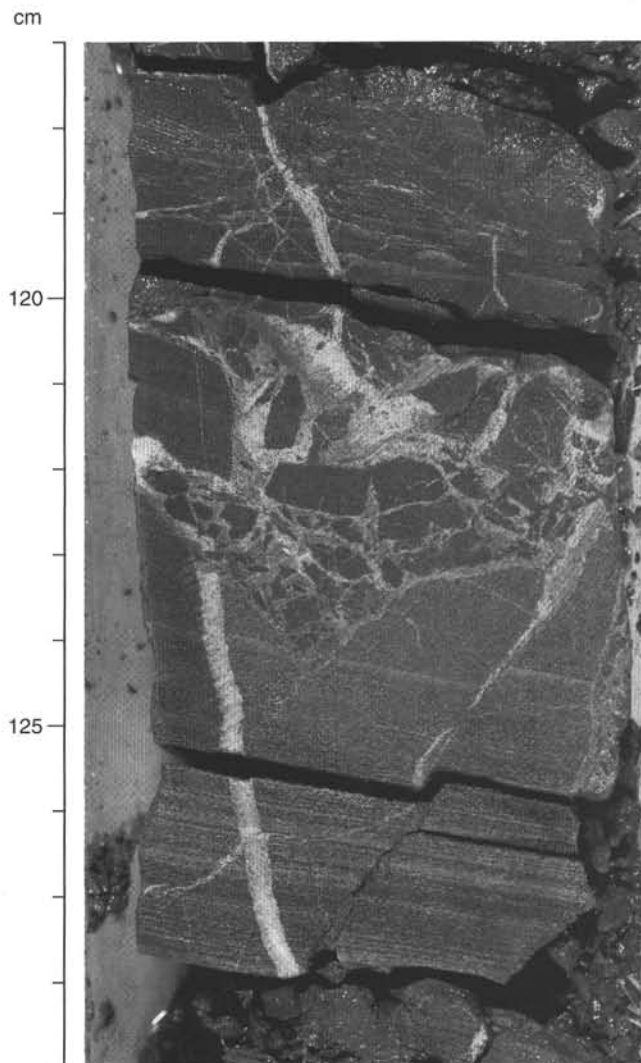


Figure 34. Calcite-cemented breccia in Section 159-962D-36R-2, at 117–129 cm. The breccia comprises angular fragments of laminated calcareous siltstone (the surrounding lithology) in a calcite matrix. This probably represents a mineralized fault zone.

ering the water depth of 4637 m at Site 962. Typically, very low organic carbon contents (about 0.2 wt%) are reported from surface sediments from equivalent pelagic settings in the center of main ocean basins (Emerson and Hedges, 1988). Large amplitude fluctuations in organic carbon deposition, as observed in sediments at Sites 959 and 960 (see "Organic Geochemistry" sections, "Site 959" and "Site 960" chapters, this volume), were not recorded in deposits at Site 962. Instead, a more continuous supply of probably unreactive, reworked organic matter delivered to the Deep Ivorian Basin is suggested during Pleistocene times (see "Composition of Organic Matter," below). This assumption is supported by pore-water profiles obtained from this sedimentary section, which do not show evidence of intense downcore degradation of labile organic matter (see "Inorganic Geochemistry" section, this chapter).

Between 16 and 70 mbsf, Paleocene–Eocene to Pliocene claystones (lithologic Subunits IB, IIA, and IIB, see "Lithostratigraphy" section, this chapter) are almost barren of both carbonate carbon and organic carbon (Fig. 35). This pattern is interpreted as a record of typical pelagic deposition below the CCD throughout the upper Cenozo-

Table 5. Summary of elemental analysis of sediments at Site 962.

Core, section, interval (cm)	Depth (mbsf)	Inorg-C (wt%)	CaCO ₃ (wt%)	Tot-C (wt%)	Org-C (wt%)	TN (wt%)	C/N
159-962B-							
1H-1, 98-99	0.98	0.06	0.5	1.39	1.33	0.16	8.3
1H-3, 98-99	3.98	0.05	0.4	1.47	1.42	0.16	8.9
1H-5, 38-40	6.38	0.04	0.3	1.53	1.49	0.15	9.8
2H-1, 77-78	8.27	0.05	0.4	1.23	1.18	0.09	13.4
2H-3, 98-99	11.48	0.04	0.3	1.55	1.51	0.14	10.5
2H-5, 74-75	14.24	0.03	0.2	1.47	1.44	0.14	10.0
3H-1, 55-56	17.55	2.73	22.7	3.26	0.53	0.09	6.0
3H-3, 112-113	21.12	1.87	15.6	2.14	0.27	0.04	6.8
3H-5, 112-113	24.12	0.14	1.2	0.49	0.35	0.05	7.3
4H-1, 92-93	27.42	0.05	0.4	0.38	0.33	0.05	6.9
4H-3, 92-93	30.42	0.04	0.3	0.32	0.28	0.04	7.0
4H-5, 92-93	33.42	0.03	0.2	0.20	0.17	0.04	4.3
5H-1, 92-93	36.92	0.04	0.3	0.12	0.08	0.03	2.5
5H-3, 92-93	39.92	0.03	0.2	0.12	0.09	0.03	2.8
5H-5, 93-94	42.93	0.03	0.2	0.12	0.09	0.03	2.8
6H-1, 90-91	46.40	0.01	0.1	0.15	0.14	0.03	4.4
6H-3, 91-92	49.41	0.04	0.3				
6H-5, 91-92	52.41	0.04	0.3	0.13	0.09	0.03	2.8
7H-1, 93-94	55.93	0.04	0.3	0.20	0.16	0.04	4.0
7H-3, 94-95	58.94	0.05	0.4	0.13	0.08	0.03	2.5
7H-5, 115-116	65.15	0.03	0.2	0.23	0.20	0.04	5.0
8H-1, 97-98	65.47	0.05	0.4	0.09	0.04	0.02	1.7
8H-3, 67-68	68.17	0.06	0.5	0.08	0.02	0.00	
9H-1, 87-88	74.87	0.05	0.4	0.89	0.84	0.04	21.0
9H-3, 99-100	77.99	0.05	0.4	1.53	1.48	0.07	20.6
9H-5, 84-85	80.84	0.05	0.4	1.45	1.40	0.06	25.0
13X-CC, 2-3	94.32	3.10	25.8	4.53	1.43	0.10	13.8
159-962D-							
7R-CC, 5-7	133.52	8.81	73.4	9.35	0.54	0.04	13.9
9R-2, 115-117	155.05	0.91	7.6	2.02	1.11	0.12	9.5
9R-5, 54-55	158.94	1.83	15.2	3.63	1.80	0.15	12.4
10R-1, 103-104	163.03	2.12	17.7	4.05	1.93	0.16	12.4
10R-2, 98-99	164.48	1.49	12.4	3.46	1.97	0.16	11.9
11R-1, 23-24	171.93	1.38	11.5	2.87	1.49	0.16	9.6
11R-1, 89-90	172.59	11.07	92.2	11.89	0.82	0.05	16.9
11R-2, 17-18	173.15	11.45	95.4	12.09	0.64	0.05	13.2
11R-CC, 3-4	173.66	2.03	16.9	3.99	1.96	0.16	12.6
12R-4, 41-42	186.21	2.35	19.6	5.59	3.24	0.22	14.5
12R-5, 81-82	188.11	1.15	9.6	2.47	1.32	0.13	10.5
13R-1, 143-144	192.43	6.05	50.4	7.52	1.47	0.12	12.6
13R-2, 11-13	192.61	7.14	59.5	8.45	1.31	0.10	13.5
15R-CC, 15-16	200.85	1.93	16.1	3.12	1.19	0.14	8.8
16R-1, 140-141	221.40	1.32	11.0	2.62	1.30	0.17	7.4
17R-CC, 1-2	229.61	10.56	88.0	11.10	0.54	0.12	4.6
18R-1, 50-51	239.60	2.09	17.4	3.23	1.14	0.18	6.2
18R-4, 88-89	244.48	6.88	57.3	7.87	0.99	0.12	8.5
19R-1, 31-32	249.11	2.46	20.5	4.08	1.62	0.19	8.4
20R-1, 142-143	259.82	1.03	8.6	2.14	1.11	0.17	6.4
20R-4, 17-18	263.07	2.09	17.4	3.10	1.01	0.14	7.4
21R-1, 119-120	269.19	0.98	8.2	2.08	1.10	0.16	7.1
21R-cc, 2-3	270.06	9.41	78.4	10.30	0.89	0.08	11.5
22R-1, 18-19	277.88	4.55	37.9	5.60	1.05	0.14	7.7
23R-1, 108-109	288.38	10.00	83.3	10.41	0.41	0.04	10.6
24R-1, 114-115	298.14	9.03	75.2	9.85	0.82	0.09	9.4
25R-1, 5-6	302.05	10.79	89.9	11.16	0.37	0.05	7.8
26R-2, 139-141	309.49	7.33	61.1	8.47	1.14	0.15	7.5
27R-2, 90-91	313.70	10.39	86.5	10.57	0.18	0.03	6.3
28R-1, 21-23	316.51	10.35	86.2	10.46	0.11	2.54	0.0
29R-1, 99-100	326.99	8.70	72.5	9.54	0.84	0.15	5.5
29R-CC, 10-12	328.10	0.51	4.2	1.72	1.21	0.20	6.1
30R-1, 108-109	336.68	8.28	69.0	9.16	0.88	0.15	5.8
30R-CC, 13-14	338.15	6.49	54.1	7.56	1.07	0.15	7.0
31R-1, 38-40	345.68	10.23	85.2	10.67	0.44	0.05	9.3
32R-1, 25-26	355.15	2.21	18.4	2.70	0.49	0.15	3.2
33R-CC, 9-10	366.92	9.72	81.0	9.83	0.11	0.03	3.9
34R-2, 115-116	371.95	8.73	72.7	9.18	0.45	0.12	3.6
35R-1, 87-89	375.17	3.12	26.0	5.18	2.06	0.25	8.3
36R-1, 23-24	384.13	5.54	46.1	6.70	1.16	0.14	8.1
37R-1, 103-105	389.53	8.06	67.1	8.93	0.87	0.11	7.6

Note: Inorg-C = inorganic carbon, CaCO₃ = carbonate, Tot-C = total carbon, Org-C = total organic carbon, TN = total nitrogen, and C/N = organic carbon/total nitrogen ratios.

ic, without strong supply of allochthonous organic matter. A temporary deepening of the CCD below the water depth of Site 962, however, could explain the moderate increase in carbonate carbon (up to 23 wt%) observed in the lower Pliocene (17-22 mbsf).

A distinct increase in organic carbon content at 75 mbsf marks a change in lithology from Tertiary clay to Cenomanian(?) or late Albian porcellanite (lithologic Subunit IIC, see "Lithostratigraphy" sec-

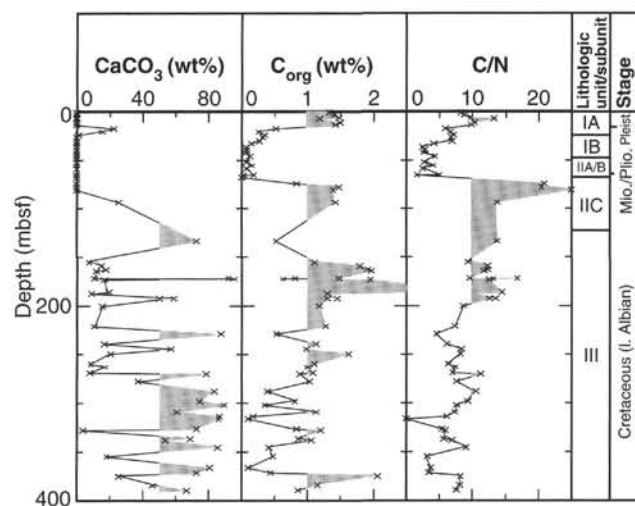


Figure 35. Carbonate content, total organic carbon content, and C/N ratios in sediments at Site 962. Lithologic units (see "Lithostratigraphy" section, this chapter) and preliminary stratigraphic stages are indicated.

tion, this chapter; Fig. 35). Organic carbon contents plateau at about 1.5 wt% while calcium carbonate relative abundance is near zero, reflecting a clear dominance of siliceous biogenic material according to smear slide results (see "Lithostratigraphy" section, this chapter). Similar porcellanite units, although of younger age (Oligocene to Miocene), were encountered at the shallower Site 959 (see "Lithostratigraphy" and "Organic Geochemistry" sections of "Site 959" chapter, this volume).

Total organic carbon contents of Site 959 deposits, in general, exceed those at Site 962, suggesting either less efficient remineralization of marine organic matter due to shallower water depths and/or higher paleoproductivity close to the African continent, or less dilution of organic carbon by other sedimentary components.

Underlying upper Albian sediments (lithologic Unit III; see "Lithostratigraphy" section, this chapter) in Hole 962D display highly variable carbonate carbon and organic carbon contents (Fig. 35), reflecting two major lithologies. The first, with high carbonate contents, ranging from 50 to almost 100 wt% and variable organic carbon contents (0.1-1.5 wt%) represent turbiditic micritic-nannofossil claystones and siltstones. Although organic carbon contents in general reach only intermediate levels (1.0 wt%) in carbonate-rich units, it needs to be stressed that sections with high organic carbon contents of 1.5 wt% are frequently correlated to elevated carbonate contents (i.e., at 192 mbsf, Sections 159-962D-13R-1 and 13R-2, or at 309 mbsf, Section 159-962D-26R-2; Table 5). The elevated organic carbon content of turbidites suggests rapid deposition and efficient preservation of sedimentary organic matter. The second lithologic type in the late Albian deposits at Site 962 are carbonate-poor, but organic carbon-rich, dark colored claystones (Fig. 35). Organic carbon contents, generally exceed 1.0 wt% and reach maximum values of 3.25 wt% at 186 mbsf (Section 159-962D-12R-4; Table 5). Highest organic carbon levels occur between 173-200 and 375-385 mbsf and at 249 mbsf (Fig. 35). During equivalent time periods in the late Albian, phases of increased paleoproductivity are suggested. Associated carbonate contents in claystones are below 20 wt%.

Composition of Organic Matter

Characterization of sedimentary organic matter, with regard to marine vs. terrigenous sources and the level of thermal maturity, was performed using C/N ratios and results from Rock-Eval pyrolysis (for

Table 6. Summary of total organic carbon (Org-C), obtained from elemental analysis, and of T_{max} , S_1 , S_2 , S_3 , hydrogen index (HI) values, and oxygen index (OI) values derived from Rock-Eval pyrolysis in sediments at Site 962.

Core, section, interval (cm)	Org-C (wt%)	T_{max} ($^{\circ}$ C)	S_1 (mgHC/gRock)	S_2 (mgHC/gRock)	S_3 (mgHC/gRock)	HI (mgHC/gTOC)	OI (mgHC/gTOC)
159-962B-							
1H-1, 98-99	1.33	468	0.02	0.61	0.31	46	23
1H-3, 98-99	1.42	475	0.23	6.42	1.83	452	129
1H-5, 38-40	1.49	474	0.21	9.16	1.57	615	105
2H-1, 77-78	1.18	474	0.25	10.93	1.60	926	135
2H-3, 98-99	1.51	473	0.37	10.08	1.55	667	103
2H-5, 74-75	1.44	478	0.39	10.72	1.60	744	111
9H-3, 99-100	1.48	391	0.23	3.19	0.61	216	41
9H-5, 84-85	1.40	388	0.24	3.21	0.46	229	33
13X-CC, 2-3	1.43	392	0.29	5.26	0.65	368	46
159-962D-							
9R-2, 115-117	1.11	422	0.05	3.14	0.54	282	48
9R-5, 54-55	1.80	415	0.14	8.28	0.72	460	40
10R-1, 103-104	1.93	419	0.16	7.65	0.81	396	42
11R-1, 23-24	1.49	420	0.07	5.17	1.00	347	67
11R-CC, 3-4	1.96	420	0.10	8.29	0.96	423	49
12R-4, 41-42	3.24	419	0.12	17.06	1.22	527	38
13R-1, 143-144	1.47	422	0.04	5.21	1.34	354	91
13R-2, 11-13	1.31	421	0.05	4.76	1.05	363	80
15R-CC, 15-16	1.19	430	0.05	2.04	0.94	172	79
16R-1, 140-141	1.30	430	0.05	2.77	0.79	213	60
18R-4, 88-89	0.99	433	0.06	2.02	0.89	204	90
19R-1, 31-32	1.62	432	0.05	2.21	0.85	136	53
20R-1, 142-143	1.11	428	0.04	1.97	0.60	178	54
21R-cc, 2-3	0.89	430	0.02	2.07	0.59	233	66
22R-1, 18-19	1.05	422	0.09	4.31	1.30	410	124
24R-1, 114-115	0.82	431	0.02	1.52	0.62	186	75
25R-1, 5-6	0.37	429	0.01	0.84	0.63	226	169
26R-2, 139-141	1.14	429	0.05	3.28	0.86	288	75
27R-2, 90-91	0.18	422	0.02	0.15	0.37	81	207
28R-1, 21-23	0.11	422	0.01	0.10	0.36	91	329
29R-1, 99-100	0.84	429	0.04	1.89	0.43	225	52
29R-CC, 10-12	1.21	433	0.02	1.65	0.39	136	32
30R-1, 108-109	0.88	434	0.06	4.85	0.83	551	94
30R-CC, 13-14	1.07	432	0.03	2.05	1.24	191	116
31R-1, 38-40	0.44	433	0.02	0.83	0.36	188	82
32R-1, 25-26	0.49	425	0.03	0.52	0.39	106	79
33R-CC, 9-10	0.11	426	0.01	0.05	0.30	41	274
34R-2, 115-116	0.45	431	0.03	0.66	0.52	148	115
35R-1, 87-89	2.06	429	0.04	2.86	0.72	139	35
36R-1, 23-24	1.16	429	0.02	1.56	0.64	135	55

analytical procedure and interpretation see "Organic Geochemistry" sections, "Site 959" and "Explanatory Notes" chapters, this volume). Results for Site 962 are summarized in Tables 5 and 6, and in Figures 35 and 36.

An abundance of reworked, thermally overmature organic matter in Pleistocene deposits, probably derived from Cretaceous outcrops along the Côte d'Ivoire-Ghana continental margin, or the nearby uplifted Côte d'Ivoire-Ghana Marginal Ridge, is suggested by organic geochemical results. High T_{max} values (468°–478°C) and high hydrogen indices (450–925 mgHC/gTOC) indicate overmature kerogen type I/II material (Tissot and Welte, 1984; Fig. 36). The occurrence of amorphous organic matter (see smear slide results in "Lithostratigraphy" section, this chapter) documents the dominance of highly degraded, lipid-rich organic matter. In addition, terrestrial influence has to be considered as plant fragments also are reported in smear slides (see "Lithostratigraphy" section, this chapter). Supply of marine immature organic matter, reflecting fluctuations in paleoproductivity during the Pleistocene, cannot be excluded at Site 962, but identification and quantification of autochthonous organic material based on shipboard organic geochemical results is difficult due to the pronounced overprint of the fossil organic signal. However, pore-water results suggest reduced amounts of reactive organic matter within these sediments (see "Inorganic Geochemistry" section, this chapter).

Miocene to Pliocene clays between 15 and 70 mbsf are characterized by very low organic carbon contents. Therefore, C/N ratios derived from Site 962 deposits do not provide useful information on the source of organic matter (Fig. 35; see "Organic Geochemistry" section, "Site 959" chapter, this volume). However, assuming that the

organic matter composition in modern deep-sea depositional settings represents an analogue for the Cenozoic environment at Site 962, a dominance of refractory oxidized organic matter of both marine and terrestrial origin can be proposed (Emerson and Hedges, 1988).

Underlying porcellanites and cherts of Late Cretaceous age (70–100 mbsf in Hole 962B and 75–123 mbsf in Hole 962D; see "Lithostratigraphy" section, this chapter) show the highest C/N ratios observed in sediments at Site 962. They reach peak values of 25 at 80 mbsf (Section 159-962B-9H-5; Fig. 35; Table 5) and co-occur with elevated hydrogen indices (200–380 mgHC/gTOC; Fig. 36). This pattern suggests a mixed marine-terrestrial origin of the organic matter. However, compared with porcellanites at Site 959, lower proportions of autochthonous organic matter seem to be preserved at Site 962. T_{max} values below 400°C are indicative of a thermally immature level (Fig. 36).

Cretaceous claystones and turbiditic limestones of lithologic Unit III (see "Lithostratigraphy" section, this chapter) can be subdivided into two subintervals based on Rock-Eval and elemental results:

(I) The upper subunit, ranging from about 150 to 195 mbsf, is characterized by a pulse-like increase in organic carbon contents (up to 3.3 wt%) and corresponding low carbonate contents (below 20 wt%), elevated C/N ratios (10–17), high hydrogen indices (220–530 mgHC/gTOC), and T_{max} values at 420°C, indicating a low stage of thermal maturity (Figs. 35, 36). This type of sediment probably was deposited in a high-productive shallow-water depositional environment in the Late Cretaceous equatorial Atlantic Ocean. Some contribution from terrestrial sources, however, is demonstrated by the frequent occurrence of plant fragments in these deposits (see "Smear Slides" section, this volume).

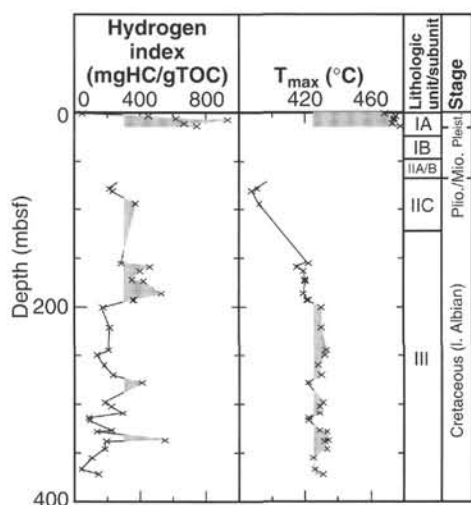


Figure 36. Hydrogen index and T_{\max} values vs. depth at Site 962. Dominant lithologic units (see "Lithostratigraphy" section, this chapter) and preliminary stratigraphic stages are indicated. Hydrogen index values of 0–50 mgHC/gTOC suggest elevated proportions of inert organic matter, values between 50–150 mgHC/gTOC suggest dominant terrestrial with minor contents of marine organic matter, and values above 200 mgHC/gTOC suggest dominant marine organic matter. T_{\max} values below 410°–420°C are characteristic of thermally immature organic matter, values 420°–460°C are characteristic of mature organic matter, and values above 460°C are characteristic of overmature organic matter.

(II) The subunit below 195 mbsf in Hole 962D, in contrast, shows lower organic carbon contents rarely exceeding 1.25 wt%, C/N ratios below 10, and remarkably constant hydrogen indices (about 200 mgHC/gTOC) and T_{\max} values about 430°C (Figs. 35, 36). Interestingly, the pyrolytic character in this part of the section does not reflect changes in lithology; carbonate-rich turbiditic limestones show organic geochemical patterns similar to TOC-rich claystones. The distinct shifts in geochemical parameters at 195 mbsf might be explained by changes in the environment from pelagic to more terrestrially influenced depositional conditions. The step-like offset in T_{\max} of about 10°C toward higher temperature values at 195 mbsf probably cannot be explained by a gradual increase in thermal maturity with depth, but rather it suggests the sudden onset of deposition of more mature and less hydrogen-rich organic matter of probable terrestrial origin in late Albian times. The observed drop in hydrogen indices between the two subunits supports this interpretation. A more conclusive interpretation of Late Cretaceous organic geochemical records, however, requires shore-based study.

SOURCE ROCK GEOCHEMISTRY

Concentrations of headspace gases were measured in all four holes at Site 962. In Hole 962D, the deepest penetration, significant quantities of hydrocarbon gases were observed. The maximum recorded methane content in this hole was 102,214 ppm in Core 159-962D-28R at approximately 316 mbsf.

Heavier hydrocarbons (C_2 – C_6) were also present throughout Hole 962D, although in relatively low concentrations. Ethane (C_2) concentrations up to a maximum of 1401 ppm were seen in Core 159-962D-30R at approximately 318 mbsf. Heavier hydrocarbons, propane through hexane, were also present in trace amounts. From the standpoint of potential safety or pollution concerns, hydrocarbon quantities encountered in Hole 962D were not problematic.

INORGANIC GEOCHEMISTRY

Five interstitial water samples cut from APC cores recovered from Hole 962B were analyzed. The data set spans the uppermost 80 mbsf at Site 962. The three uppermost samples (159-962B-1H-3, 145–150 cm, 159-962B-2H-3, 145–150 cm, and 159-962B-3H-3, 145–150 cm) were taken from the silty clay of lithologic Unit I of late Miocene to late Pleistocene age at 4.45, 11.95, and 21.45 mbsf. The next two samples (159-962B-6H-3, 145–150 cm; and 159-962B-9H-3, 145–150 cm) were from early Miocene radiolarian claystones and palygorskite claystones, both within lithologic Unit II at 49.95 and 78.45 mbsf, respectively. At approximately 90 mbsf a chert layer was encountered in Hole 962B, forcing the abandonment of Hole 962B. One 10-cm whole-round sample was cut from Section 159-962D-9R from upper Albian claystones at 155.45 mbsf. However, after trimming disturbed portions of the sample, less than 0.2 mL of pore fluid could be extracted from the remaining sediment. As this volume was inadequate for the suite of routine analyses, interstitial water sampling at Site 962 was terminated. The interstitial water chemical data for this site are tabulated in Table 7.

The low abundance of biogenic carbonate (<2%) and reactive organic matter throughout the upper 100 mbsf of the sediment pile at Site 962 (see "Organic Chemistry" section, this chapter) are reflected in the chemistry of pore waters. Limited delivery and accumulation of these sediment components at the seafloor, relative to the other Leg 159 sites, are most likely a consequence of the greater water depth of the site (4649 m) and its location near the calcium carbonate compensation depth (CCD). These factors profoundly affect the sediment diagenesis at Site 962 in comparison to the other Leg 159 sites, as discussed below.

Chloride concentrations are slightly elevated relative to those of the shallower sites drilled during Leg 159, but remain similar to concentrations of ambient seawater. As at Sites 959 to 961, in situ diagenetic reactions, rather than fluid mixing or advection, appear to control variations in the chemistry of interstitial waters at Site 962.

Microbially Mediated Organic Degradation

The relatively long water column at Site 962 allows more extensive oxic degradation of sinking organic matter. As a result, the pool of organic carbon that has accumulated at this site is likely to be more refractory than at Sites 959 to 961. Thus, in spite of the relatively high organic carbon content of Cores 159-962B-1H and 2H, up to 1.5% organic carbon (see "Organic Geochemistry" section, this chapter), the impact of microbial organic matter degradation on pore-water chemistry at Site 962 is minimal compared to Sites 959–961. The profiles of sulfate, alkalinity, and ammonium (Fig. 37A–C) all support this interpretation. The rate of decrease of sulfate concentrations is less rapid than at previous sites, with sulfate concentrations of 19 mM at approximately 80 mbsf. Pore-water alkalinity remains low and similar to values typical of seawater over the first 80 mbsf. Ammonium concentrations remain low, reaching a maximum of about 200 μ M, at 80 mbsf, compared to concentrations exceeding 900 μ M in the same depth range at Sites 959–961. Headspace methane concentrations are not plotted, but remain at background levels throughout this section of the sediment pile, consistent with the persistence of sulfate in pore-water samples. Below the chert horizon at approximately 120 mbsf, headspace methane concentrations increase abruptly, suggesting that the chert may act as an impermeable cap rock and that this methane may be thermogenic rather than bacterial in origin.

Iron and Manganese Profiles

The presence of abundant pyrite in sediments from Core 159-962B-2H (see "Lithostratigraphy" section, this chapter) suggests that

Table 7. Interstitial water analyses from Hole 962B.

Core, section, interval (cm)	Depth (mbsf)	IW		Alkalinity (mM)	Salinity (g/kg)	Ca (mM)	Mg (mM)	Sr (μM)	Cl (mM)	SO ₄ (mM)	NH ₄ (μM)	SiO ₂ (μM)	K (mM)	Fe (μM)	Mn (μM)
		vol (mL)	pH												
159-962B-															
1H-3, 145-150	4.45	55	7.73	3.73	35.0	10.6	51.14	97	562	25.0	27	354	12.45	0.7	6.2
2H-3, 145-150	11.95	32	8.01	4.37	35.0	10.67	51.31	96	563	28.1	98	306	13.52	0.2	5.6
3H-3, 145-150	21.45	42	7.34	4.01	35.0	10.59	50.59	108	560	24.2	135	201	12.77	6.7	6.4
6H-3, 145-150	49.95	41	7.78	4.55	35.0	11.73	49.51	137	562	21.2	144	727	11.63	1.6	5.9
9H-3, 145-150	78.45	32	7.37	4.7	34.5	12.5	47.96	168	556	20	208	686	10.49	0.6	5.7

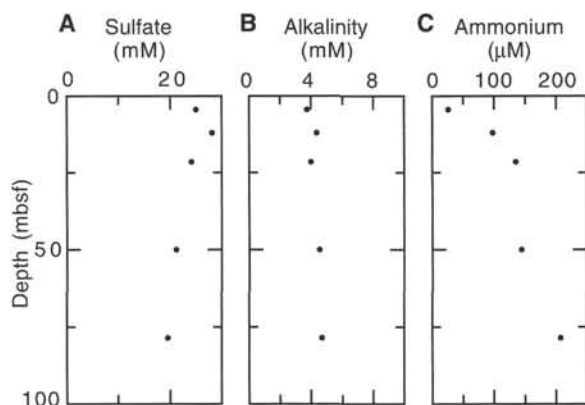


Figure 37. Interstitial water concentrations for (A) sulfate, (B) alkalinity, and (C) ammonium plotted vs. depth at Site 962.

dissolved oxygen in the pore water is likely to be completely consumed above 15 mbsf. Reduction of iron and manganese oxides to their soluble divalent states should be associated with oxygen depletion. Dissolved manganese concentrations remain nearly constant at approximately 6 μM in all Site 962 interstitial water samples. In contrast to Sites 959 and 960, manganese appears to be unrelated to carbonate diagenesis. The relative constancy of manganese concentrations at Site 962 (Table 7) may reflect a solubility control by an authigenic manganese phase, possibly manganese sulfide. The maximum dissolved iron concentration at Site 962, 6 μM (Table 7), is lower than the maximum iron concentrations at Sites 959 through 961. This may well reflect the widely spaced sampling intervals. Sediments from Cores 159-962B-1H through 5H contain oxidized iron minerals (goethite), reduced iron sulfides, and glauconite (see "Lithostratigraphy" section, this chapter). Within the zone of sulfate reduction, goethite should be unstable and subject to reduction, and precipitation of sulfide minerals should be favored. Redistribution of iron among these different phases should exert a strong influence on the distribution of dissolved iron in the sediment column at Site 962 and is likely related to the apparent maximum in dissolved iron concentrations at 21 mbsf.

Calcium, Magnesium, and Strontium Profiles

Concentrations of dissolved calcium and magnesium change little with depth from seawater values in the uppermost samples at Site 962, reflecting the low abundance of calcium carbonate in these sediments. These profiles contrast with those from the other sites drilled during Leg 159, which show greater downhole changes in these concentrations. Calcium concentrations are similar to seawater values in the upper 22 mbsf of Site 962; calcium increases by ~20% by ~79 mbsf (Fig. 38A). At Sites 960 and 961, dissolved calcium increased by 50% over the same depth interval. Likewise, dissolved magne-

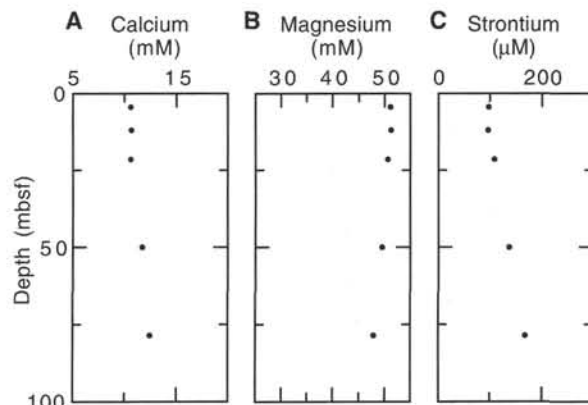


Figure 38. Interstitial water concentrations for (A) calcium, (B) magnesium, and (C) strontium plotted vs. depth at Site 962.

sium concentrations are only slightly lower than seawater, averaging 51 ± 0.4 mM in the upper 22 mbsf, and decreasing to 47 mM in the lowermost sample of Site 962 (Fig. 38B). In contrast, over the same depth interval at Site 961, dissolved magnesium decreases to 39 mM.

The small increase in dissolved calcium with depth at Site 962 may be due to dissolution of calcite. Nannofossil and foraminifer fragments are rare in the upper 30 mbsf, but are not apparent in smear slides between this level and about 90 mbsf. Yet, the dissolution of extremely few coccoliths within these sediments may be a source for dissolved calcium. Moreover, these microfossils are relatively abundant in the Albian claystone in Core 159-962B-10H. Sinks for dissolved magnesium are probably related to the formation of porcellanite, and smectite and chlorite within these clay-rich sediments.

Dissolved strontium increases from 97 μM at ~4.5 mbsf to 168 μM at ~78.5 mbsf (Fig. 38C). The downhole increase in dissolved strontium at Site 962 is smaller than at Sites 960 and 961, but comparable to that at Site 959. This is surprising because sediments within the same depth interval at Site 959 are nannofossil ooze and chalk, with relatively abundant calcium carbonate (~40%). Because the source of dissolved strontium is most likely either dissolution and/or recrystallization of calcium carbonate, it implies that these reactions may be more intensive within the smaller solid phase pool of Site 962.

Potassium and Silica Profiles

Depth variations in the concentrations of potassium (Fig. 39A) and silica (Fig. 39B) are analogous to Sites 959-961. As before, dissolved silica concentrations appear to be governed mainly by dissolution and recrystallization of biogenic silica. Dissolved silica concentrations decrease from approximately 400 μM in the shallowest interstitial water sample to approximately 200 μM in Core 159-962B-3H. This pattern mimics the distribution of opal in the sediment (see

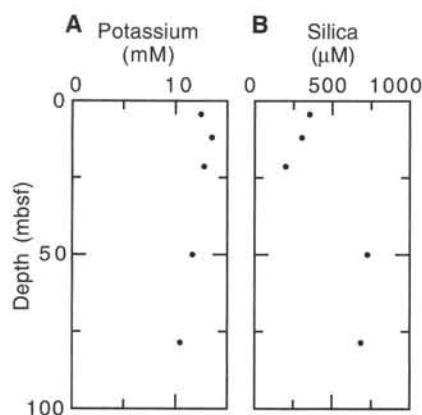


Figure 39. Interstitial water concentrations for (A) potassium and (B) silica plotted vs. depth at Site 962.

“Lithostratigraphy” section, this chapter). Samples from lithologic Subunits IIA and IIC contain markedly higher dissolved silica concentrations, nearly 800 μM . This increase in dissolved silica concentrations is almost certainly related to the more siliceous character of lithologic Subunits IIA and IIC, which are described as a radiolarian claystone, and chert and porcellanite unit, respectively. Potassium concentrations at Site 962 decrease with increasing depth in the sediment, as was observed at all other Leg 159 sites. In spite of the very different sedimentary regime at Site 962, the gradient associated with decreasing potassium concentrations is remarkably similar to all other sites drilled during Leg 159. As before, we interpret this decrease as evidence of potassium uptake in association with authigenic clay mineral formation. See the “Inorganic Geochemistry” section in the “Site 959 chapter” (this volume) for additional discussion of this topic.

PHYSICAL PROPERTIES

Measurements on whole cores taken at Site 962 were made with the magnetic susceptibility meter, gamma-ray attenuation porosity evaluator (GRAPE), *P*-wave Logger (PWL), and Natural Gamma Radiation (NGR) tool. Full-space thermal conductivity measurements were made. Index properties, compressional (*P*) wave velocity, shear strength, and electrical resistivity were measured on split cores. Descriptions of the experimental methods are provided in the “Physical Properties” section of the “Explanatory Notes” chapter (this volume). All tables and all MST data are available on CD (this volume).

Multisensor Track

Magnetic susceptibility was measured in all cores recovered at Site 962. The results are discussed in the “Paleomagnetism” section (this chapter).

GRAPE density was measured on all cores from Holes 962A and 962B. Because of drilling disturbances at Hole 962D, GRAPE density was measured only between 150 and 162 mbsf. GRAPE density values were edited and Boyce-corrected, and only maximum bulk density values were taken into consideration. At Hole 962B, Boyce-corrected bulk density values gradually increase with depth down to about 40 mbsf from about 1.2 to 1.4 g/cm^3 (Fig. 40A). A slight decrease to 1.2 g/cm^3 occurs down to 47 mbsf, corresponding to the change in lithology from claystones with quartz silt to radiolarian claystones. Values below this level gradually increase to 1.3 g/cm^3 at about 60 mbsf. From 60 to 69 mbsf Boyce-corrected bulk density values are slightly lower, reflecting less dense sediments (palygorskite

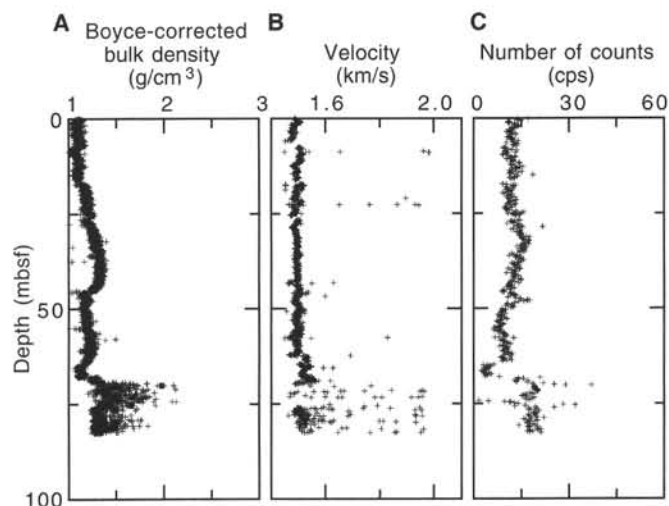


Figure 40. Results from MST measurements at Hole 962B. A. Boyce-corrected density; results from the GRAPE. B. Horizontal *P*-wave velocity; results from the PWL. C. Total number of counts; results from the NGR.

claystone). At 70 mbsf density values increase and become more scattered and range from 1.4 to about 1.8 g/cm^3 .

Horizontal *P*-wave velocity was measured on full sections from 0 to 83 mbsf at Hole 962B and edited in two steps. The velocity data from the seafloor to 64 mbsf are generally constant at about 1.50 km/s (Fig. 40B). A slight increase to about 1.55 km/s was observed at 64 mbsf. Below 70 mbsf, the data become more scattered with some higher values, which coincides with a transition to denser, more consolidated sediments. The scattering could be partially the effect of degradation of the measurement quality, caused by bad contact between the sediments and the liner but also by inhomogeneities in the core (i.e., lithified pieces such as chert, interbedded in softer matrix).

NGR data were collected with 30-s-long counting periods in cores from Holes 962A, 962B, and 962D. Data (i.e., total number of counts) are reported in counts per second (cps) with the total background radiation (8.74 cps) subtracted. The NGR variation with depth corresponds well to small lithologic changes. At Hole 962B, NGR ranges from 7 to 18 cps between the seafloor and 55 mbsf (Fig. 40C). Local maxima occur at 32 and 47 mbsf. At 47 mbsf, there is a decrease in NGR that correlates well with the transition to radiolarian claystone. The interval from 55 to 64 mbsf has slightly higher values because of its high porcellanite content. Lithologic Subunit IIB (64.5–69.5 mbsf), which is composed mainly of palygorskite claystone, is characterized by distinctly lower NGR values (<6 cps). Below 69 mbsf, the NGR data oscillate at about 20 cps and become more scattered as more lithified, and more disturbed, sediments (clay and porcellanite breccia with chert clasts and pyrite) were recovered. Several high values exceeding 25 cps are induced by the high glauconite content (e.g., Section 159-962B-8H-4). NGR was measured between 152 and 373 mbsf at Hole 962D. The values do not show any downhole trend; they are scattered and range between 10 and 30 cps.

Thermal Conductivity Measurements

Thermal conductivity data were collected in full-space configuration from every other section of each core from Hole 962B down to 81 mbsf. At Hole 962D, where recovery was poor and the sediments are more lithified, only a few measurements could be conducted.

Thermal conductivity at Hole 962B increases slightly with depth from 0.86 to 1.26 $\text{Wm}^{-1}\text{C}^{-1}$ from the seafloor to about 43 mbsf (Table 8; Fig. 41). The highest values correspond to sediments from litho-

Table 8. Thermal conductivity data from Site 962.

Core, section, interval (cm)	Depth (mbsf)	Lithologic unit	Thermal conductivity ($\text{Wm}^{-1}\text{C}^{-1}$)
159-962B-			
1H-1, 75	0.75	IA	1.09
1H-3, 75	3.75	IA	0.86
1H-5, 50	6.50	IA	1.00
2H-1, 75	8.25	IA	0.87
2H-3, 75	11.25	IA	0.92
2H-5, 75	14.25	IA	0.84
3H-1, 75	17.75	IA	0.89
3H-3, 75	20.75	IA	0.92
3H-5, 75	23.75	IA	0.97
4H-1, 75	27.25	IB	0.93
4H-3, 75	30.25	IB	1.08
4H-5, 75	33.25	IB	0.96
5H-1, 110	37.10	IB	1.05
5H-3, 110	40.10	IB	1.14
5H-5, 110	43.10	IB	1.26

Only a part of this table is reproduced here. The entire table appears on the CD-ROM (back pocket).

logic Subunit IB that contain more quartz (i.e., quartz silt component). This is followed by a shift to lower values at 46 mbsf and a general increase downhole; this trend continues in the sediments recovered from Hole 962D.

Index Properties

Index properties were determined from measurement of wet and dry masses and from wet and dry volumes. Index properties were measured either on cube samples cut from lithified sediments or on sediments in beakers taken from softer lithologies. The same oriented cubes were used later for discrete three-dimensional velocity measurements.

The index properties show two major downhole trends at Holes 962B and 962D with a large discontinuity at about 70 mbsf (Table 9; Fig. 42). At Hole 962B, there is a continuous increase in bulk density from 1.28 to 1.56 g/cm^3 between the seafloor and 43 mbsf. There is a drop to lower bulk-density values (about 1.40 g/cm^3) near the boundary between lithologic Units I and II (47.0 mbsf). The bulk density then increases to 1.50 g/cm^3 at 68 mbsf (near the boundary between lithologic Subunits IIB and IIC). A distinct shift to higher bulk density values (generally $>2.0 \text{ g/cm}^3$) occurs between 74 and 78 mbsf, and this trend continues to the bottom of Hole 962D (393.5 mbsf). The higher values of bulk density for sediments recovered below 68 mbsf are probably related to compaction, advanced diagenesis, and tectonic deformation that they have been exposed to since their deposition. Porosity values below 75 mbsf at Hole 962D are lower than at Hole 962B—the lowest values (about 1%) of porosity were measured on chert samples at 75 and 113 mbsf.

Velocimetry

Discrete measurements of P -wave velocity at Hole 962B were collected close to the location of samples for index properties in softer sediments and, in more lithified sediments, on the same cube samples. At Hole 962D, as sediments were well lithified, only cubes were cut for measurements.

Discrete velocity values collected in the sediments of Hole 962B (0–70 mbsf) are rather low and uniform, and range from 1.50 to 1.65 km/s, with a gradual increase downhole (Table 10; Fig. 43). At Hole 962D (113–390 mbsf), sediments are more consolidated, and there is an increase in velocities with more scattered values that range from 1.87 to 5.94 km/s. Below 200 mbsf, the values become less scattered and the velocity varies from 2.62 to 5.77 km/s. The highest velocities

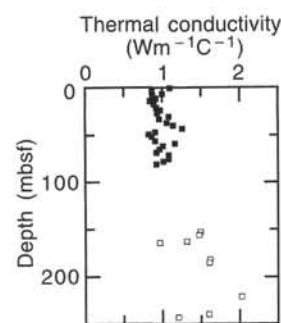


Figure 41. Thermal conductivity variation with depth at Site 962. Solid squares = Hole 962B, open squares = Hole 962D.

were measured for chert, cemented limestones, and well-lithified siltstones.

At Hole 962D, the anisotropy of velocity calculated from discrete velocity measurements in the vertical and horizontal directions ranges from -0.38 to 0.35 (Table 10; Fig. 43C). Three measurements, performed on lithified laminated cubes, show that velocity in the direction parallel to lamination is higher than that in the direction perpendicular to lamination, regardless of the orientation of the lamination with respect to the core axis.

Table 10 further shows P -wave velocities corrected to in situ conditions. The corrected velocity is calculated from in situ seawater velocity, sediment porosity, seawater velocity in the laboratory, and sediment velocity (cf. "Physical Properties" section, "Explanatory Notes" chapter, this volume). The downhole variation of in situ seawater velocity and porosity was determined from regression analysis. The linear and the power regression models in KaleidaGraph 3.0.4 were used to generate curve-fit equations for in situ seawater velocity and porosity. The curve fit between the equations and data is good for in situ seawater velocity and porosity at Site 962 (>0.99 and 0.92 , respectively).

Undrained Shear Strength

Undrained shear strength was measured down to 70 mbsf at Hole 962B. Sediments from Hole 962D were too consolidated for vane shear or penetrometer measurements.

Generally, the strength of the sediments gradually increases with depth, although three intervals could be distinguished (Table 11; Fig. 44). Overlapping vane shear and penetrometer measurements were made between 36 and 49 mbsf. Both techniques show similar trends of undrained shear strength variation with depth, but the results from penetrometer measurements are consistently lower than those from the vane shear device. From the seafloor to about 26 mbsf (boundary between lithologic Subunits IA and IB), there is an increase in strength, followed by constant values of 17 kPa from 27 to 33 mbsf. Below that, there is again an interval with increasing shear strength, reaching a peak of 93 kPa at 68 mbsf.

Electrical Resistivity

Electrical resistivity was measured only in Hole 962B (0–68 mbsf), as the sediments recovered from Hole 962D were too consolidated to allow insertion of the resistance probe. Maximum values of resistance were obtained directly from the display of the Wayne Precision Components Analyzer. Resistivity was calculated by multiplying resistance by the cell constant.

At Hole 962B, the resistivity values from the seafloor to 15 mbsf range from 0.11 to 0.17 Ωm (Table 12; Fig. 45). From 15 mbsf, there

Table 9. Index properties data from Site 962.

Core, section, interval (cm)	Depth (mbsf)	Lithologic unit	Water content		Density			Porosity (%)	Void ratio (1)
			Total wet mass (%)	Mass of solids (%)	Wet bulk (g/cm ³)	Solids-grain (g/cm ³)	Dry (g/cm ³)		
159-962B-1H-1, 96	0.96	IA	68.66	219.11	1.28	2.55	0.40	85.72	5.46
1H-3, 96	3.96	IA	67.90	211.55	1.30	2.52	0.42	86.07	5.21
1H-5, 44	6.44	IA	70.39	237.76	1.27	2.21	0.38	87.05	5.12
2H-1, 77	8.27	IA	68.28	215.21	1.28	2.53	0.41	85.43	5.31
2H-3, 95	11.45	IA	68.52	217.65	1.28	2.16	0.40	85.60	4.59
2H-5, 72	14.22	IA	66.94	202.46	1.31	2.58	0.43	85.73	5.10
3H-1, 50	17.50	IA	59.15	144.79	1.40	2.70	0.57	80.69	3.81
3H-3, 110	21.10	IA	54.92	121.83	1.45	2.62	0.66	77.94	3.12
3H-5, 110	24.10	IA	56.47	129.73	1.44	2.68	0.63	79.55	3.39
4H-1, 90	27.40	IB	51.58	106.51	1.50	2.65	0.73	75.49	2.75
4H-3, 90	30.40	IB	51.11	104.52	1.51	2.62	0.74	75.34	2.68
4H-5, 90	33.40	IB	48.77	95.21	1.54	2.68	0.79	73.09	2.49
5H-1, 90	36.90	IB	46.74	87.75	1.58	2.70	0.84	71.83	2.31
5H-3, 90	39.90	IB	46.47	86.81	1.58	2.62	0.84	71.51	2.22
5H-5, 90	42.90	IB	48.58	94.46	1.56	2.66	0.80	73.72	2.46

Only a part of this table is reproduced here. The entire table appears on the CD-ROM (back pocket).

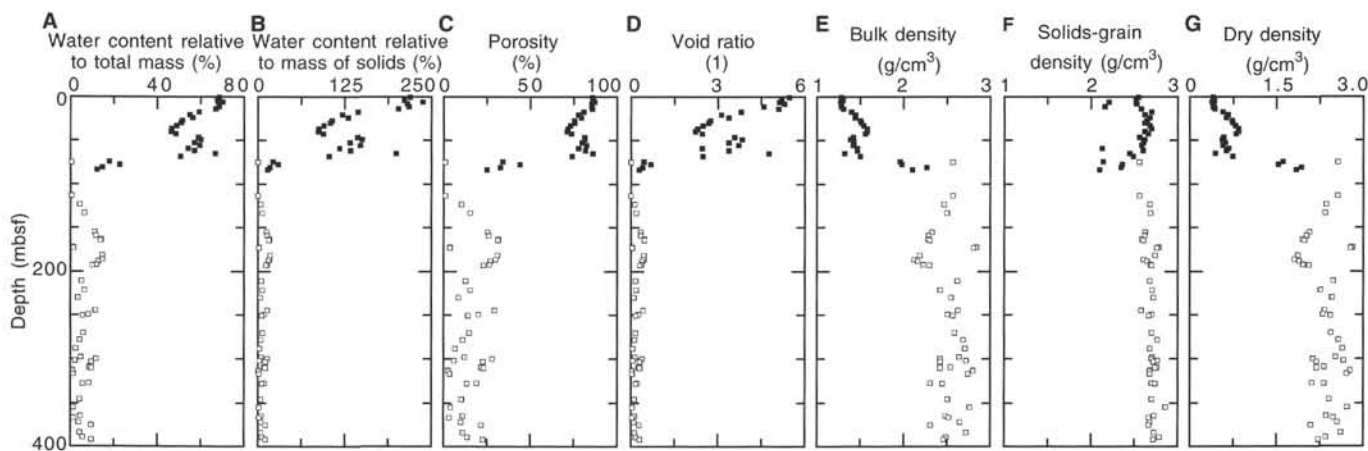


Figure 42. Index properties variations with depth at Site 962. Solid squares = Hole 962B, open squares = Hole 962D.

Table 10. P-wave velocity and anisotropy data from Site 962.

Core, section, interval (cm)	Depth (mbsf)	Lithologic unit	Uncorrected velocity			Anisotropy		Corrected velocity			DSV
			Vert (km/s)	Hor 1 (km/s)	Hor 2 (km/s)	Hor 1 (1)	Hor 2 (1)	Vert (km/s)	Hor 1 (km/s)	Hor 2 (km/s)	
159-962B-1H-1, 95	0.95	IA	1.546	—	—	—	—	1.552	—	—	1
1H-1, 95	0.96	IA	—	1.523	—	—	—	—	1.529	—	3
1H-2, 97	2.47	IA	1.505	—	—	—	—	1.512	—	—	1
1H-2, 97	2.48	IA	—	1.513	—	—	—	—	1.520	—	3
1H-3, 47	3.48	IA	1.504	—	—	—	—	1.511	—	—	1
1H-3, 49	3.5	IA	—	1.520	—	—	—	—	1.527	—	3
2H-1, 75	8.26	IA	1.503	—	—	—	—	1.511	—	—	1
2H-1, 77	8.27	IA	—	1.512	—	—	—	—	1.520	—	3
2H-3, 93	11.44	IA	1.510	—	—	—	—	1.519	—	—	1
2H-3, 94	11.45	IA	—	1.517	—	—	—	—	1.526	—	3
2H-5, 70	14.2	IA	1.504	—	—	—	—	1.513	—	—	1
2H-5, 71	14.22	IA	—	1.512	—	—	—	—	1.521	—	3
3H-1, 48	17.49	IA	1.505	—	—	—	—	1.515	—	—	1
3H-1, 50	17.5	IA	—	1.511	—	—	—	—	1.521	—	3
3H-3, 108	21.08	IA	—	1.510	—	—	—	—	1.520	—	3

Note: Vert = vertical direction (along core); Hor 1 = horizontal direction (perpendicular to cut core face); Hor 2 = horizontal direction perpendicular to Hor 1; DSV 1 = Digital Sound Velocimeter; DSV 3 = Hamilton Frame Velocimeter.

Only a part of this table is reproduced here. The entire table appears on the CD-ROM (back pocket).

Table 12. Electrical resistivity and formation factor data, Hole 962B.

Core, section, interval (cm)	Depth (mbsf)	Lithologic unit	Resistivity		Formation factor	
			Vert (ohm-m)	Hor (ohm-m)	Vert (1)	Hor (1)
159-962B-						
1H-1, 92	0.92	IA	0.14	0.12	0.60	0.53
1H-3, 95	3.95	IA	0.15	0.14	0.65	0.59
1H-5, 41	6.41	IA	0.12	0.16	0.54	0.68
2H-1, 77	8.27	IA	0.10	0.11	0.43	0.50
2H-3, 93	11.43	IA	0.12	0.17	0.53	0.73
2H-5, 69	14.19	IA	0.14	0.11	0.60	0.47
3H-1, 46	17.46	IA	0.20	0.23	0.86	1.01
3H-3, 107	21.07	IA	0.29	0.26	1.30	1.16
3H-5, 107	24.07	IA	0.36	0.29	1.59	1.29
4H-1, 87	27.37	IB	0.26	0.16	1.13	0.72
4H-3, 88	30.38	IB	0.21	0.22	0.92	1.00
4H-5, 94	33.44	IB	0.29	0.13	1.30	0.58
5H-1, 95	36.95	IB	0.24	0.22	1.05	0.96
5H-3, 88	39.88	IB	0.24	0.23	1.06	1.03
5H-5, 95	42.95	IB	0.27	0.25	1.22	1.09

Note: Vert = vertical direction (parallel to core axis) Hor = horizontal direction (perpendicular to cut core axis).

Only a part of this table is reproduced here. The entire table appears on the CD-ROM (back pocket).

Table 11. Undrained shear strength data from Hole 962B.

Core, section, interval (cm)	Depth (mbsf)	Lithologic unit	Shear strength	
			Vane shear (kPa)	Penetrometer (kPa)
159-962B-				
1H-1, 100	1.01	IA	2.5	—
1H-3, 104	4.04	IA	2.4	—
1H-5, 48	6.48	IA	3.0	—
2H-1, 68	8.19	IA	3.7	—
2H-3, 100	11.50	IA	6.6	—
2H-5, 75	14.26	IA	5.7	—
3H-1, 54	17.55	IA	10.7	—
3H-3, 114	21.14	IA	12.4	—
3H-5, 115	24.15	IA	18.7	—
4H-1, 95	27.46	IB	17.0	—
4H-3, 98	30.48	IB	17.4	—
4H-5, 95	33.45	IB	17.2	—
5H-1, 96	36.97	IB	24.2	—
5H-1, 97	36.97	IB	—	14.7
5H-3, 100	40.00	IB	30.2	—

Only a part of this table is reproduced here. The entire table appears on the CD-ROM (back pocket).

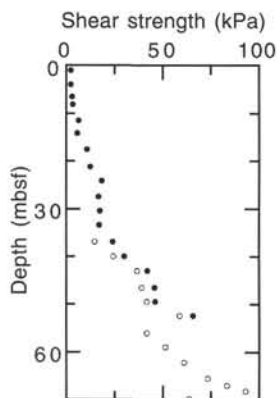


Figure 44. Undrained shear strength variation with depth at Hole 962B. Solid circles = vane shear data, open circles = penetrometer data.

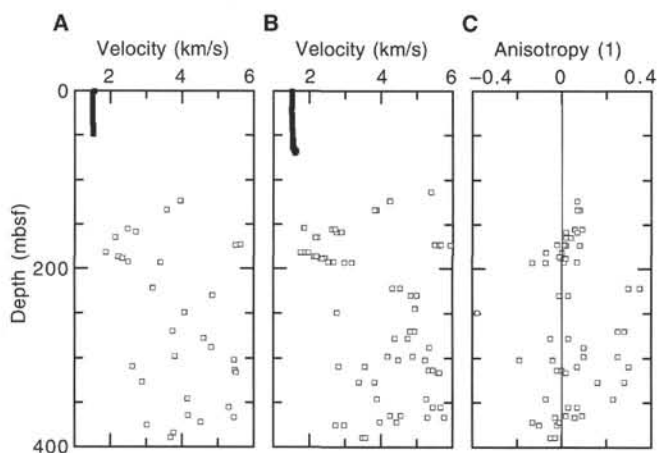


Figure 43. Results of discrete velocity measurements vs. depth at Site 962. A. P-wave velocity in vertical direction. B. P-wave velocity in horizontal direction. C. Anisotropy. Solid squares = Hole 962B, open squares = Hole 962D.

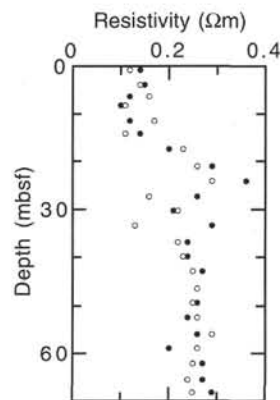


Figure 45. Electrical resistivity variation with depth at Hole 962B. Solid circles = vertical resistivity, open circles = horizontal resistivity.

is an increase to higher resistivity values (about 0.36 Ωm at 24 mbsf), followed by a general decrease to 0.13 at 33 mbsf. There is a slightly increasing trend downhole, from 0.22 to 0.29 Ωm between 37 and 68 mbsf.

The formation factor was calculated using a pore-water resistivity of 0.226 Ωm and is presented in Table 12. No correlation between porosity and formation factor was made owing to time constraints.

Summary

Physical properties data at Site 962 reflect variations in the lithology, consolidation, and composition of sediments. GRAPE and NGR measurements at Hole 962B correlate well with the lithology; also, the index properties and discrete velocity measurements show some distinctive downhole trends.

The most important discontinuities in the physical properties data of Site 962 at Hole 962B are at about 47 and 70 mbsf. The discontinuity at 47 mbsf corresponds to the boundary between lithologic Units I and II (Figs. 40–42, 44). At the second discontinuity (70 mbsf), bulk density increases abruptly and porosity drops sharply (Fig. 42). Moreover, the NGR and GRAPE densities increase to high-

Table 13. Summary of logging operations at Hole 962D.

Hole	Tool string	Tool string components	Depth (mbsf)
962D	Seismic stratigraphic	DITE/HLDT*/SDT/NGTC/TLT	Main: 328–162 Repeat: 306.5–173
962D	FMS	FMS/GPIT/NGTC	Main: 293–192 Repeat: 293–192

Notes: * = used for caliper only (source removed). DITE = Dual Induction Resistivity Tool; HLDT = High Temperature Lithodensity Tool; SDT = Sonic Digital Tool (Array); NGTC = Natural Gamma Ray Tool; TLT = Lamont-Doherty Temperature Tool; FMS = Formation MicroScanner; GPIT = General Purpose Inclinerometer Tool.

er and more scattered values (Fig. 40). This discontinuity corresponds to the boundary between lithologic Subunits IIB and IIC at 69.9 mbsf. Sediments in these units are significantly different; lithologic Subunit IIB is composed of mainly palygorskite claystone and glauconitic silty sand of unknown age, whereas lithologic Subunit IIC consists of chert and porcellanite of late Albian age.

DOWNHOLE MEASUREMENTS

Logging Operations

Poor borehole conditions at Site 962 hindered logging at this site, but to a lesser degree than at Site 960. A modified seismic stratigraphic tool string was deployed in Hole 962D, including the High Temperature Lithodensity Tool (with nuclear source removed) to provide caliper measurements. The Formation MicroScanner (FMS) tool string was also run in Hole 962D, despite the less than ideal conditions, because of the importance of obtaining structural data at this site. Sea-state conditions were mild and the wireline heave compensator was employed during most of the logging.

Bridges once again prevented both tool strings from reaching the total depth of the hole (393.5 mbsf). The seismic stratigraphic tool string, run at about 900 ft/hr, collected a main log (328–162 mbsf) and a repeat log (306.5–173 mbsf). The FMS tool string reached a depth of only 293 mbsf, collecting main and repeat logs over the interval 293–192 mbsf at a speed of about 1800 ft/hr. A summary of logging operations is presented in Table 13.

Log Quality and Data Processing

As at Site 960, the data suffered from the effects of extreme borehole washout, which severely degraded the quality of the sonic and FMS logs. Although the caliper arms were able to maintain contact with the borehole walls for most of the logged interval, washout was still a problem and the hole diameter exceeded 14 in. throughout most of the measured interval. Borehole size variations induce “cycle skipping” in the sonic velocity log as a result of the receivers picking incorrect first arrival times used in velocity calculation. This log, however, can be improved with post-cruise processing of the full-waveform sonic data. The resistivity and gamma-ray data (see processed logs at the end of chapter) are affected to a much lesser degree by borehole washout.

Selected logs collected with the seismic stratigraphic tool string are shown in Figure 46. All these logs were linearly depth-shifted relative to the seafloor (–4657 mbsf) and will undergo further depth-shifting during post-cruise processing. Preliminary shipboard processing of the FMS data from Hole 962D was not performed owing to time restrictions. Complete processing and interpretation of the FMS data will be performed post-cruise.

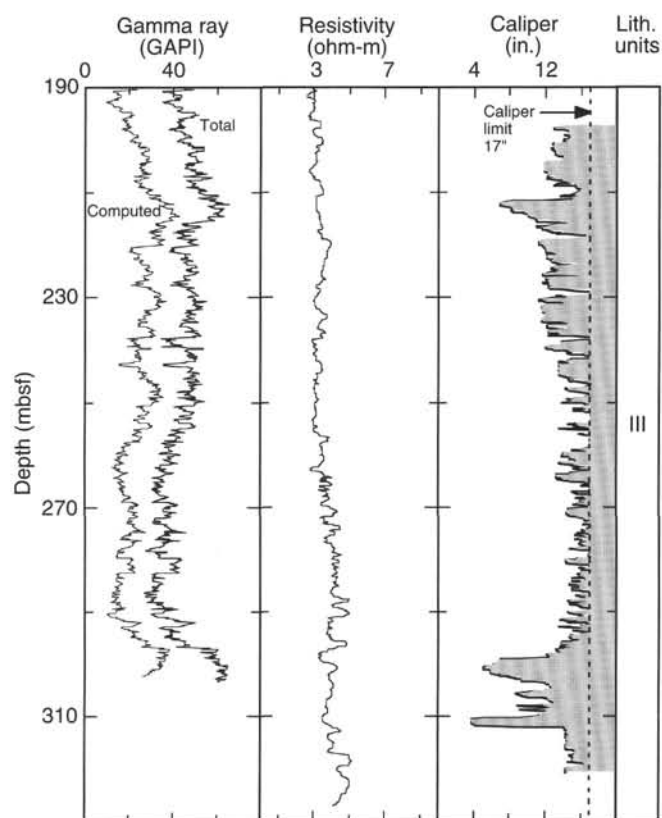


Figure 46. Summary of selected log data from Hole 962D. Lithologic units are shown at right (see “Lithostratigraphy” section, this chapter).

Comparison of Core and Log Physical Property Measurements

Although the natural gamma-ray values were measured both in the core and by logs at Site 962, there are insufficient data to compare the core and log measurements effectively because of the low core recovery in Hole 962D.

Log Interpretation and Lithology

The logs collected at this site do not cross any lithologic boundaries and fall entirely within lithologic Unit III (see “Lithostratigraphy” section, this chapter), which includes claystone, siltstone, sandstone, and limestone. The natural gamma-ray and resistivity logs show little variation throughout the logged interval. Overall, the natural gamma-ray values are in the same range (10–60 API units) as those seen in the lower sections of Holes 960A and 960C (Fig. 47), but at 210–215 and 295 mbsf there are slight increases that result from higher levels of thorium (see processed logs at the end of chapter). The most notable feature in the logs is the change in borehole diameter evident in the caliper log (Fig. 46), where two bridges (at 210–215 and 295 mbsf) coincide with the small, short-lived increases in natural gamma-ray values. This suggests the presence of slightly more shaley beds that are more resistant to borehole washout. The resistivity log shows even less character than the natural gamma-ray log, and is slightly lower than the log resistivities seen in the previous holes (Fig. 47).

Measurements with FMS Images

Hole deviation is limited in Hole 962D. The deviation increases from 0.6° at 191 mbsf to 1.5° at 280 mbsf, but is almost 0° at 195 mbsf (Fig. 48). The azimuth of the hole varies slightly between N15° and N40°.

The diameter of the hole shows high-frequency variations that may reflect claystone beds alternating with more resistive siltstones. The thickness of the resistive layers varies from 20 cm to 1 m in the lower part of the logged interval, whereas they can reach 5 m between 190 and 247 mbsf (Fig. 46). The elongation of the hole (maximum width/minimum width) varies between 1 and 1.2 with no preferential direction, as it is probably related to washout.

The FMS data from Hole 962D was not processed on board because of time constraints.

Borehole Temperature

The Lamont-Doherty Temperature Logging Tool (TLT) was run at the bottom of the seismic stratigraphic tool string in Hole 962D. The formation cools during drilling operations because of drilling fluid circulation, and temperatures begin to rebound only after drilling has ceased. Because logging started only 11.5 hr after drilling ceased, the temperatures measured (Fig. 49) predominantly reflect the seawater temperature in the borehole, rather than the true formation temperature. The depths for the TLT tool were calculated from the pressures recorded by the tool.

An equilibrium thermal profile for the run was difficult to obtain because of fluid circulation during hole conditioning immediately prior to logging. Temperatures range from 5°C at seafloor to 10°C at 328 mbsf. The temperatures increase approximately linearly for the interval surveyed and only one break of approximately 1°C was observed at the bottom of the pipe. This variation gives a geothermal gradient of about 15°C/1000 m. Thermal lags due to mud clogging can be observed between the downhole and uphole logs, with the latter more affected.

Synthetic Seismogram

A log-derived synthetic seismogram is not presented for this site because of the lack of density data and the poor quality of the velocity data associated with borehole washouts throughout the logged interval. Post-cruise processing of the velocity (full waveform) data is required to produce a reliable velocity log.

REFERENCES

- Basile, C., 1990. Analyse structurale et modélisation analogique d'une marge transformante: l'exemple de la marge profonde de Côte d'Ivoire-Ghana. *Mem. Doc. CAESS Rennes*, 39.
- Basile, C., Mascle, J., Popoff, M., Bouillin, J.P., and Mascle, G., 1993. The Côte d'Ivoire-Ghana transform margin: a marginal ridge structure deduced from seismic data. *Tectonophysics*, 222:1–19.
- Berggren, W.A., 1977. Late Neogene planktonic foraminiferal biostratigraphy of the Rio Grande Rise (South Atlantic). *Mar. Micropaleontol.*, 2:265–313.
- Byers, C.W., 1977. Biofacies patterns in euxinic basins: a general model. In Cook, H.E., and Enos, P. (Eds.), *Deep-water Carbonate Environments*. Spec. Publ.—Soc. Econ. Paleontol. Mineral., 25:5–17.

- Cande, S.C., and Kent, D.V., 1992. A new geomagnetic polarity time scale for the Late Cretaceous and Cenozoic. *J. Geophys. Res.*, 97:13917–13951.
- Chamley, H., 1989. *Clay Sedimentology*: Berlin (Springer-Verlag).
- Emerson, S., and Hedges, J.I., 1988. Processes controlling the organic carbon content of open ocean sediments. *Paleoceanography*, 3:621–634.
- Giresse, P., and Barusseau, J.-P., 1989. Quaternary accumulation rates by hemipelagic and gravity current sedimentation on the Atlantic margin of Africa: control factors of advective and vertical flows. *Mar. Geol.*, 89:279–297.
- Heath, G.R., 1981. Ferromanganese nodules of the deep sea. *Econ. Geol.*, 75:736–765.
- Honnorez, J., Villeneuve, M., and Mascle, J. 1994. Old continent-derived metasedimentary rocks in the Equatorial Atlantic: an acoustic basement outcrop along the fossil trace of the Romanche transform fault at 6°30'W. *Mar. Geol.*, 117:237–251.
- Keigwin, L.D., Jr., 1982. Neogene planktonic foraminifers from Deep Sea Drilling Project Sites 502 and 503. In Prell, W.L., Gardner, J.V., et al., *Init. Repts. DSDP*, 68: Washington (U.S. Govt. Printing Office), 269–288.
- Klingebiel, A., Boltzenhagen, C., Caratini, C., Debyser, Y., Delteil, J.R., Duran, B., Etienne, J., Huc, A., Latouche, C., Millepieds, P., Parra, M., Pujol, C., Sauvan, P., and Sommer, F., 1975. Etude stratigraphique, sédimentologique et géochimique des sédiments carottés dans le golfe de Guinée au cours de la campagne Bénin 1971. *Bull. Inst. Geol. Bassin Aquitaine*, 17:101–232.
- Konta, J., 1985. Mineralogy and chemical maturity of suspended matter in major river samples under the SCOPE/UNEP project. *Mitt. Geol.-Palaeontol. Inst. Univ. Hamburg*, 58:569–592.
- Mascle, J., and the Scientific Party, 1994. Les marges continentales transformantes ouest-africaines—Côte d'Ivoire, Ghana, Guinée. *Série Repères Océan*, 5: Brest (IFREMER).
- Molfini, B., and McIntyre, A., 1990. Nutricline variations in the equatorial Atlantic coincident with the Younger Dryas. *Paleoceanography*, 5:997–1008.
- Moore, D.M., and Reynolds, R.C., Jr., 1989. *X-ray Diffraction and the Identification and Analysis of Clay Minerals*: Oxford (Oxford Univ. Press).
- Perch-Nielsen, K., 1985. Mesozoic calcareous nannofossils. In Bolli, H.M., Saunders, J.B., and Perch-Nielsen, K. (Eds.), *Plankton Stratigraphy*: Cambridge (Cambridge Univ. Press), 329–426.
- Pickering, K.T., Hiscott, R., and Hein, F.J., 1989. *Deep-marine Environments: Clastic Sedimentation and Tectonics*: London (Unwin Hyman).
- Pickering, K.T., Stow, D., Watson, M., and Hiscott, R., 1986. Deep-water facies, processes and models: a review and classification scheme for modern and ancient sediments. *Earth-Sci. Rev.*, 22:75–174.
- Sage, F., 1994. Structure crustale d'une marge transformante et du domaine océanique adjacent: exemple de la marge de Côte d'Ivoire-Ghana [Ph.D. thesis]. Univ. Pierre et Marie Curie, Paris.
- Sanfilippo, A., Westberg-Smith, M.J., and Riedel, W.R., 1985. Cenozoic radiolaria. In Bolli, H.M., Saunders, J.B., and Perch-Nielsen, K. (Eds.), *Plankton Stratigraphy*: Cambridge (Cambridge Univ. Press), 631–712.
- Sato, T., and Takayama, T., 1992. A stratigraphically significant new species of the calcareous nannofossil *Reticulofenestra asanoi*. In Ishizaki, K., and Saito, T. (Eds.), *Centenary of Japanese Micropaleontology*: Tokyo (Terra Sci. Publ.), 457–460.
- Scholle, P.A., Arthur, M.A., and Ekdale, A.A., 1983. Pelagic environments. In Scholle, P.A., Bebout, D.G., and Moore, C.H. (Eds.), *Carbonate Depositional Environments*. AAPG Mem., 33:620–691.
- Tissot, B.P., and Welte, D.H., 1984. *Petroleum Formation and Occurrence* (2nd ed.): Heidelberg (Springer-Verlag).

Ms 159IR-108

NOTE: For all sites drilled, core-description forms (“barrel sheets”) and core photographs can be found in Section 4, beginning on page 317. Smear-slide data can be found in Section 5, beginning on page 587. Scanned structural VCDs, structural data spreadsheets, and selected scanned microstructures are included on the CD-ROM in the back of this volume. Also presented on the CD-ROM are all processed logs (including FMS, dipmeter, BRG temperature, high-resolution density, and neutron data), sonic waveforms, and explanatory text.

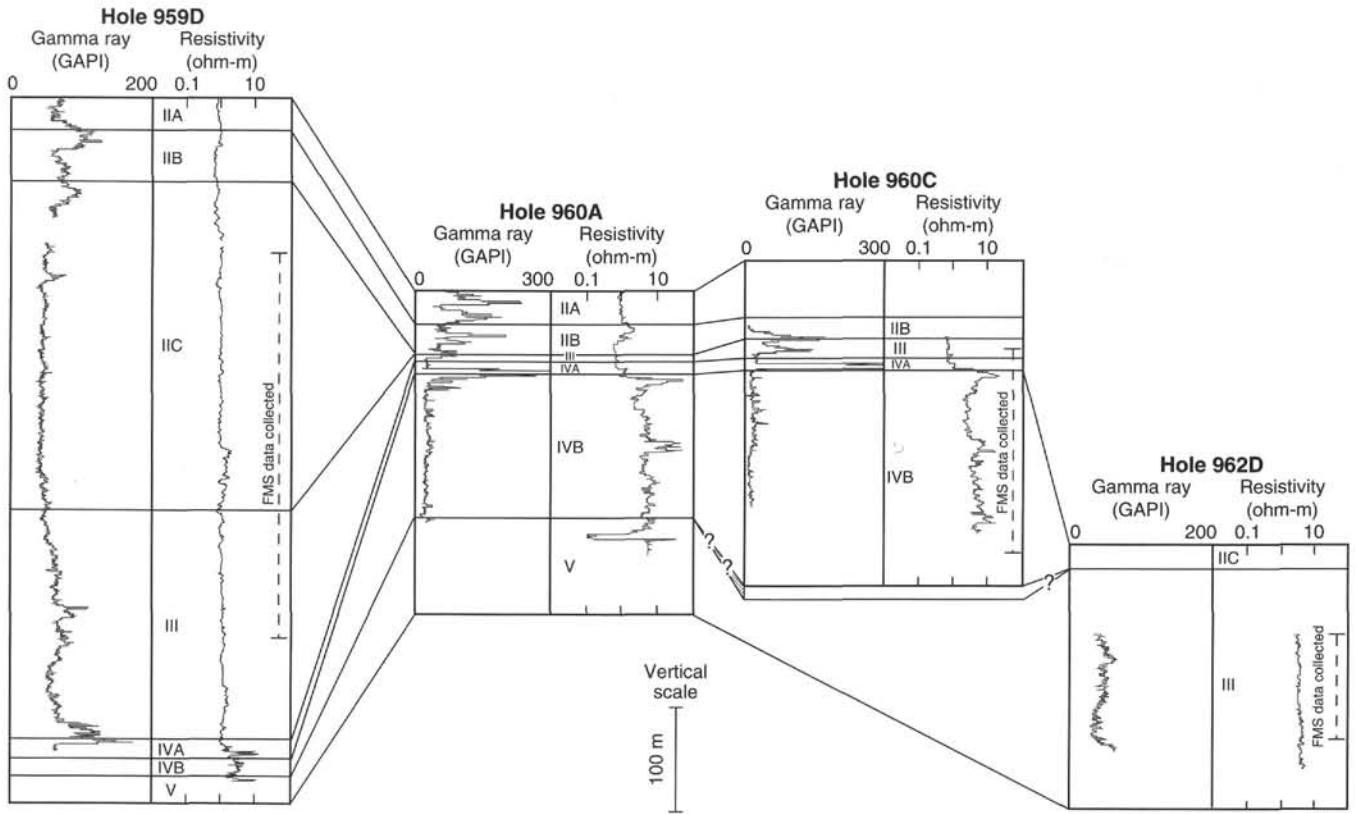


Figure 47. Comparison of natural gamma-ray and shallow focused resistivity logs for Holes 959D, 960A, 960C, and 962D. Correlation of the lithologic units (see “Lithostratigraphy” section, this chapter) shows that logs were obtained only in lithologic Unit III. The resistivity log is plotted on a logarithmic scale.

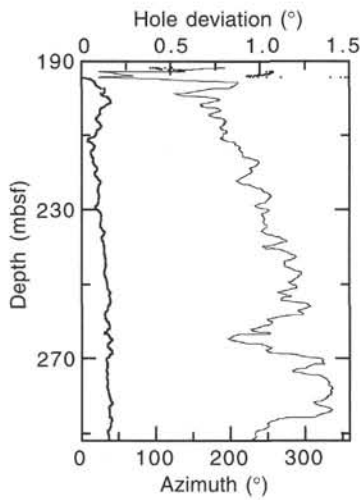


Figure 48. Deviation (thin line) and azimuth (thick line and dots) of Hole 962D in the interval logged by the FMS tool. Deviation and azimuth are by reference to the vertical and north, respectively.

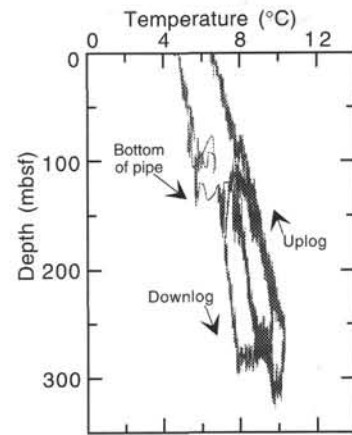


Figure 49. Borehole fluid temperature in Hole 962D from the Lamont-Doherty Temperature Logging Tool, which was run on the seismic stratigraphic tool string. Maximum temperature was 10°C at 328 mbsf.

SHORE-BASED LOG PROCESSING

HOLE 962D

Bottom felt: 4657 mbrf (used for depth shift to seafloor)

Total penetration: 393.5 mbsf

Total core recovered: 92.76 m (29.3%)

Logging Runs

Logging string 1: DIT/SDT/NGT with hydraulic caliper and no HLDT source.

Logging string 2: FMS/GPIT/NGT (two passes)

Wireline heave compensator was used to counter the mild ship heave.

Bottom-hole Assembly

The following drill pipe depths are as they appear on the logs after differential depth shift (see "Depth shift" section) and depth shift to the seafloor. As such, there might be a discrepancy with the original depths given by the drillers on board. Possible reasons for depth discrepancies are ship heave, use of wireline heave compensator, and drill string or wireline stretch.

DIT/SDT/NGT: Bottom-hole assembly at ~189 mbsf.

FMS/GPIT/NGT: Bottom-hole assembly at ~189 mbsf.

Processing

Depth shift: Reference run for depth shift: DIT/SDT/NGT main pass. All original logs have been interactively depth shifted with ref-

erence to NGT from DIT/SDT/NGT main pass, and to the seafloor (-4657 m).

Gamma-ray processing: NGT data have been processed to correct for borehole size and type of drilling fluid.

Acoustic data processing: The quality of the data is impaired by the bad hole conditions. The borehole size variations induced frequent cycle skipping in the log, the result of the receivers picking incorrect first arrival times. Because of the extremely noisy character of the sonic logs, no processing has been performed at this stage.

Quality Control

Data recorded through bottom-hole assembly, such as the NGT data above 189 mbsf, should be used only qualitatively because of the attenuation on the incoming signal.

Hole diameter was recorded by the hydraulic caliper on the HLDT tool (CAL) and the caliper on the FMS string (C1 and C2).

Details of standard shore-based processing procedures are found in the "Explanatory Notes" chapter, this volume. For further information about the logs, please contact:

Cristina Broglia
Phone: 914-365-8343
Fax: 914-365-3182
E-mail: chris@ldeo.columbia.edu

Elizabeth Pratson
Phone: 914-365-8313
Fax: 914-365-3182
E-mail: beth@ldeo.columbia.edu

Hole 962D: Natural Gamma Ray-Resistivity Logging Data

